New Physics of the Standard Model and Beyond

by

Chen Zhang

A thesis submitted in conformity with the requirements
for the degree of Doctor of Philosophy
Graduate Department of Physics
University of Toronto

Abstract

New Physics of the Standard Model and Beyond

Chen Zhang
Doctor of Philosophy
Graduate Department of Physics
University of Toronto
2020

In this thesis, I present the research works carried during my Ph.D. period from 2014 to 2019, on topics of the high energy completion and the low energy exploration of the Standard Model (SM). The focus will be put on four finished papers.

Firstly, we introduce the extensions of the Standard Model that are not only completely asymptotically free, but are such that the UV fixed point is completely UV attractive. Semi-simple gauge groups with elementary scalars in various representations are explored. We also present a Pati-Salam model for illustration.

We then attempt to build the asymptotically safe extensions of the Standard Model using the large number-of-flavour technique.

Next, we build a phenomenological model that describes the mass and decay width spectra of the lightest pseudo-scalar and scalar meson nonets at low energy. We then apply this model to the study of quark matter, and find that udQM (quark matter consists of up and down quarks only) generally has a lower energy per baryon than the strange quark matter and normal nuclei for baryon number $A > A_{\rm min}$ with $A_{\rm min} \gtrsim 300$.

After that, we present the work on the ud quark stars (udQSs) that are composed of udQM. Distinct signatures are discussed compared to the conventional study regarding strange quark stars. The tidal deformabilities in binary star mergers, including the udQS-udQS and udQS-HS cases, are calculated. This study points to a new possible interpretation of the GW170817 binary merger event, where udQS may be at least one component of the binary system detected.

Dedication

To my beloved grandfather

Acknowledgements

I sincerely thank my supervisor Bob Holdom for guiding me with his insight and advising me with his patience throughout my degree. I also thank Jing Ren, from whom I learned a lot in our several collaborations during her postdoc period here. Thanks also to Prof. Michael Luke and Prof. William Trischuk for their helpful suggestions in my committee meetings.

I dedicate this thesis to the memory of my grandfather Jing-Quan Zhang (张景泉), who passed away on August 13, 2015. Owing to him, my childhood was filled with laughter and joy, and my early adulthood was as sweet as my childhood. He was a mechanical engineer and an entrepreneur, starting his career by himself from the old days when illiteracy and hunger were common in China. He led the whole family to surviving and thriving with his diligence, devotion, kindness, and sense of responsibility. The memories and the inspirations will never fade away.

I thank my grandmother Feng-Jiao Gao (高凤娇) for her love and care. I also thank my parents, Rui-Sheng Zhang (张瑞胜) and Wen-Xia Wang (王文霞). Giving me the chance of coming to this planet and the fortune of being loved as their son, they also give me total freedom on choosing what I pursue in my life. Last but not least, I thank my brother Qi Zhang (张琦) for the fun and warm brotherhood.

The research in this thesis is supported in part by the Natural Sciences and Engineering Research Council of Canada.

Contents

Chapter 1

Introduction

The Standard Model (SM) founded 50 years ago has achieved a huge success with the experimental validation reaching TeV energies. It describes three fundamental forces: the strong, weak, electromagnetic interactions with the gauge group $SU(3)_C \times SU(2)_L \times U(1)_Y$ respectively. The electroweak sector $SU(2)_L \times U(1)_Y$ was introduced by Weinberg to model leptons [1], and later was extended to the quark sector, which additionally is gauged under colour $SU(3)_C$ group.

The Standard Model is built in the paradigm of the Quantum Field Theory (QFT). In QFT, particles are treated as the excitations of the quantized fields. When calculating physical observables like the scattering amplitudes, the quantum physics enters as the loops in the Feynman diagrams, which may result in divergences in the calculation. The Renormalization Group (RG) method [2, 3] is the basic approach to cure these notorious divergences, where the counterterms are introduced for the cancellation of infinities. RG introduces scale dependence for the strength of the couplings. The function describing the changing rate of any coupling g over energy scale μ is called "beta function": $\beta = dg/d\ln\mu$. The renormalization of any pure non-abelian gauge group leads to the asymptotic freedom ($\beta \leq 0$) [4, 5], in which the coupling goes asymptotically small to zero. Oppositely, the abelian gauge coupling and scalar quartic coupling grow asymptotically larger and ultimately reach infinity at some high energy scale (the Landau pole problem), as shown in Figure. 1.1.

Towards the ultraviolet (UV) scale, it was found that the gauge couplings of the Standard Model gauge group $SU(3) \times SU(2) \times U(1)$ tend to merge at the scale of 10^{15} GeV [7], assuming no new physics enters in the intermediate region. The unification of couplings provides a first hint of the Grand Unified Theories (**GUT**) as the possible UV completion of the Standard Model, where the SM can be embedded into a non-abelian gauge group with higher rank beyond the GUT scale. This picture automatically cures

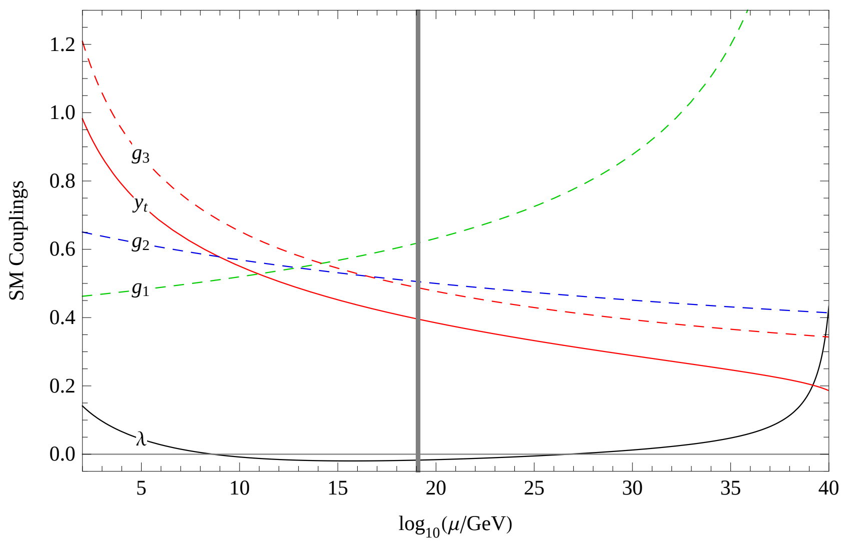

Figure 1.1: Running of the SM couplings [6]. The Higgs quartic coupling is evaluated at 1-loop, the top Yukawa and the gauge couplings are evaluated at 2-loop order. The abelian gauge coupling (green dashed) and the quartic (black) diverge at large scales beyond Planck scale.

the U(1) Landau pole problem, but generally induces proton decay faster than what the experiments suggest. Another serious problem is the so-called the naturalness problem or the hierarchy problem, in which the Higgs mass acquires a quadratic correction sensitive to the new physics scale at UV, causing tension with the light mass experimentally observed. We will try to address these problems via constructing UV fixed points in Chapter 4 and Chapter 5.

Reversing the renormalization flow of asymptotic freedom back towards the infrared (IR) scale implies that the $SU(3)$ gauge coupling α_s becomes very strong at low energy around 200 MeV, the scale of which is conventionally denoted as Λ_{QCD}. Therefore, strong dynamics has to be involved at long-distance scale $\sim 1/\Lambda_{\mathrm{QCD}}$, which gives rise to the colour confinement that only colour singlet states can be observed experimentally. In the picture of effective field theory (EFT), we can integrate out the heavy mass freedoms of the UV physics so that the effective description of low energy physics can be obtained, with high mass dimension terms suppressed by the heavy mass scale integrated out. In this way, one can tell which term plays a more important role than the others in the determination of low energy physics. However, the lack of knowledge on IR strong dynamics makes it extremely hard to derive the effective description from first principles. Therefore, some intuitive guesses have to be made, with the correctness examined by the theoretical consistency or from the experimental tests. For example, we know that u, d, s quarks have relatively small quark masses, so QCD should have an approximate chiral flavour symmetry $SU(3)_L \times SU(3)_R$. The chiral condensate formed in QCD vacuum can break this symmetry dynamically down to the diagonal $SU(3)_{\mathrm{V}}$ group, from which eight Goldstone bosons are generated, with their masses given by the explicit chiral symmetry breaking due to the finite current quark masses. The eight Goldstone bosons can be naturally interpreted as the eight components of a pseudo-scalar octet. Models incorporating this simple physics picture, including the Nambu-Jona-Lasinio model (NJL) [8, 9], the linear and non-linear sigma models [10, 11, 12, 13] have achieved huge successes on explaining the QCD phenomenology.

Colour confinement leads to the common state of quarks in forms of hadrons, either $q\bar{q}$ meson or qqq baryon. But the collective many-body interactions at the high density regime may lead to a phase transition from the hadronic matter to the quark matter, a state composed entirely of quarks instead of neutrons and protons. It is a natural and fundamental question to ask what the most stable form of QCD matter is. We will explore this question in Chapter 6.

1.1 Organization of the Thesis

In Chapter 2, we give an overview of the UV completion of SM. We introduce some background knowledge for the QCD dense matter in Chapter 3. In Chapter 4 and Chapter 5, we present our work on the UV completion of the Standard Model through some asymptotically free [17] and asymptotically safe [18] extensions, respectively. After that, we explore the physics at IR, proposing a new form of quark matter, udQM [19], in Chapter 6. The related gravitational-wave probe [20] is presented in Chapter 7. In the appendix, we present the details of the generalized meson potential and the study of finite-size effects used in Chapter 6.

Chapter 2

Overview of the UV completions

In this chapter, we give an overview of the current status of UV completion, introducing the background knowledge of the asymptotically free extension for Chapter 4, and the asymptotically safe extension for Chapter 5. We first give a recap on the grand unified theory (GUT) that embeds the SM to gauge groups with a higher rank. Then we introduce the program on the asymptotic free extensions of the SM, in which all couplings are made asymptotically free at high energy scale. After that, we present the other possible UV completions of the SM via asymptotic safety, where the couplings may achieve a set of non-zero UV fixed points. Finally, we briefly introduce the UV completion of the gravity sector.

2.1 The Grand Unification Theory

What is the ultimate fate of particle physics at high energy? A straightforward speculation is that the SM gauge group may be embedded into a simple group with an equal or larger rank. To see this, note that the one loop beta function of gauge theories has the following general form

$$\beta = \frac{dg}{dt} = \frac{bg^3}{(4\pi)^2}, \tag{2.1}$$

where $t = \ln \mu$ and

$$b = -\left(\frac{11}{3}C_2(G) - \frac{4}{3}\omega C(r_f)\, n_F - \frac{1}{3}C(r_s)\, n_S\right). \tag{2.2}$$

Here n_F is the number of fermion flavour. ω is $\frac{1}{2}$ for Weyl fermions and 1 for Dirac fermions. The Lie group factors $C_2(r) \cdot \mathrm{I} = T^a T^a$ so that $C_2(G)\delta^{ab} = f^{acd} f^{bcd}$ for the adjoint representation. And $C(r)\delta^{ab} = \mathrm{Tr}(T^a T^b)$. For the fundamental representation of $SU(N)$ group, $C_2(G) = N$, $C(r_f) = C(r_s) = 1/2$. Implementing Eq. (2.1) for the Standard Model gauge group with corresponding matter content, it turns out all Standard Model couplings tend to meet at the high energy scale ($\sim 10^{15}$ GeV) [7], where a unification into a larger Lie group can be achieved. This is the picture of "Grand Unified Theory".

The minimal GUT group is $SU(5)$, which has rank four as the SM does. The Standard Model fermions can perfectly fit into **5** and **10** representation of $SU(5)$. To break $SU(5)$ to the SM, we need a scalar in adjoint representation **24** of $SU(5)$, with the Higgs doublet in **5** for the subsequent electroweak symmetry breaking. However, $SU(5)$ GUT suffers some severe problems. On the theoretical side, one needs to introduce an additional $SU(5)$ singlet to incorporate right-hand neutrino, which is needed for the generation of the neutrino mass observed. Besides, it has the "doublet-triplet splitting" problem: the colour triplet component of **5** must have its mass at the GUT scale, while the remaining Higgs doublet resides at the electroweak scale. On the experimental side, the current proton decay bound has already ruled out the minimal $SU(5)$ model, since the leptoquarks (gauge bosons of $SU(5)$ that carry both lepton number and quark number) cause the proton to decay too fast.

A more plausible GUT group is $SO(10)$. The spinor representation **16** of $SO(10)$ naturally incorporates the SM matter freedoms in its component **15**, with the remaining **1** for the right-hand neutrino. It can give a better fit to the proton lifetime compared to SU(5) GUT. The supersymmetric extensions can improve the fit further, but there is no LHC signature of supersymmetry so far.

One can also seek to unify the SM into a higher-rank semi-simple gauge group, like the Pati-Salam $SU(4)_C \times SU(2)_L \times SU(2)_R$ [21] and the Tri-unification $SU(3)^3$ [22]. In the $SU(4)$ of Pati-Salam unification, the fourth colour is the lepton number. The fundamental representation of Pati-Salam **(4,1,2)** and **(4,2,1)** can be naturally embedded into the **16** of $SO(10)$, so that it can also be seen as an intermediate unification between SM and $SO(10)$, which can help saturate the proton lifetime constraint.

2.2 UV Completion with Asymptotic Freedom

In this section, we introduce the Complete Asymptotic Freedom (CAF) program [19, 14, 15, 16], in which all couplings are made asymptotically free at high energy scale. In 1973, Cheng et al. [14] initiated this program and studied related aspects in $SU(N)$ and $O(N)$ gauge groups with fermions in vector, adjoint, and tensor representation. Later in 2014, Giudice [16] et al. and our group [19] generalized this to the semi-simple gauge group almost at the same time.

The main struggle is to realize the asymptotic freedom for the quartic coupling, since the couplings of non-abelian gauge group are intrinsically asymptotically free, and the abelian gauge group can be embedded into a non-abelian gauge group at UV. As we will see, the gauge group with a larger rank and matter content with fewer scalar freedoms helps to reach this goal.

We review the basic idea to realize CAF in [14]. The one-loop β-functions are sufficient for the study of asymptotic freedom. For each of the gauge couplings, the β-function only depends on itself, as introduced in Eq. (2.1). Therefore, when the β-function coefficient $b > 0$, the gauge coupling g increases as the energy scale μ increases. Oppositely, $b \leq 0$ gives the asymptotic freedom. For the Yukawa coupling y, its β function has the generic form

$$\beta_y = \frac{1}{(4\pi)^2}(c\, y^3 - d\, g^2 y), \tag{2.3}$$

where the coefficients $c, d > 0$. The dependence on g can be eliminated with a change of variable $\bar{y} \equiv y^2/g^2$, which gives

$$(4\pi)^2 g^{-2} \beta_{\bar{y}} = 2c\, \bar{y}^2 - (d+b)\bar{y}, \tag{2.4}$$

where the dependence on b has appeared due to the insertion of Eq. (2.1). To have asymptotically free y amounts to find a UVFP for $\bar{y}$. Eq. (2.4) shows a stable UVFP requires that $d + b > 0$, in which case $\bar{y} = 0$ is the stable UVFP. The result is that $\bar{y}$ decreases asymptotically as

$$\bar{y}(t) \propto t^{\frac{d+b}{b}}. \tag{2.5}$$

So the contribution of Yukawa couplings is negligible in the β-functions of quartic couplings in the deep UV. For a scalar Φ_i with potential

$$V_\lambda = \lambda\, \Phi_i^* \Phi_i \Phi_j^* \Phi_j, \tag{2.6}$$

the one loop β-function for λ is

$$(4\pi)^2 \beta_\lambda = e\, \lambda^2 - f\, \lambda g^2 + k\, g^4. \tag{2.7}$$

The coefficients e, f, k can be calculated from the Feynman diagram shown as Fig. 2.1.

If Φ is in the fundamental representation of a $SU(N_A)$ gauge group, then $e = 4(N+4)$, $f = 6(N - \frac{1}{N})$, $k = 3(N-1)(N^2+2N-2)/4N^2$. We may again eliminate the dependence

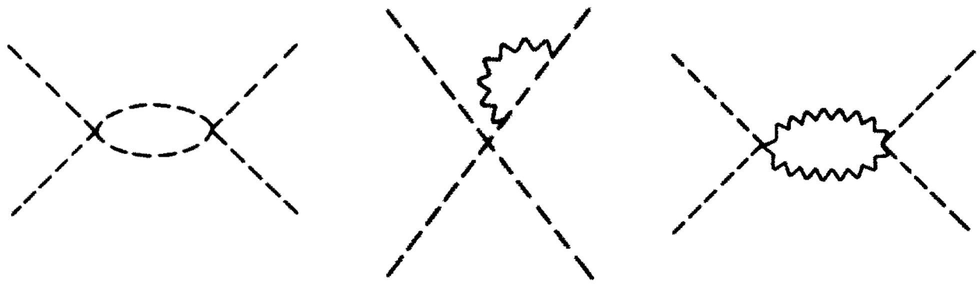

(a) (b) (c)

Figure 2.1: Diagrammatic representations of the e, f, k terms in Eq. (4.6), respectively [14]. The dashed line and the wavy line denote the scalar and the gauge boson, respectively.

on g by a change of variable $\bar{\lambda} \equiv \lambda/g^2$, which gives

$$(4\pi)^2 g^{-2} \beta_{\bar{\lambda}} = e\,\bar{\lambda}^2 - \bar{\lambda}(2b+f) + k. \tag{2.8}$$

The fixed points should satisfy $\beta_{\bar{\lambda}} = 0$, which is simply a quadratic equation for $\bar{\lambda}$ and there are two real roots $\bar{\lambda}^*_{1,2}$ when

$$(2b+f)^2 - 4ek > 0. \tag{2.9}$$

Stability requires $\lambda > 0$. This constraint translates to $2b + f < 0$, since e is always positive. Together with Eq. (4.8), these imply that complete asymptotic freedom favours the absolute value of b as small as possible, which can be achieved by adding more fermion degrees of freedom without changing the sign of b.

We will present our related work in Chapter 4.

2.3 UV Completion with Asymptotic Safety

A theory featuring an interacting UV fixed point corresponds to the scenario of asymptotic safety (AS). AS was first introduced by Weinberg [23] to address the issue of the non-renormalizability of Einstein gravity. Later, people applied this idea to gauge theories, particularly in the context of the Veneziano limit where both colour number N_C and flavour number N_F are sent to infinity while their ratio is kept fixed [24, 25]. In 2017, we attempted to realize asymptotic safety in the finite N_C regime [18] with the large N_F

technique [26], where N_F is taken to infinity while keeping N_C finite [26]. Here we give a brief review on the large N_F technique [26]. The abelian β-function is defined as

$$\beta(\alpha) = \frac{\partial \ln \alpha}{\partial \ln \mu}. \tag{2.10}$$

The one loop result is $\beta(\alpha) = 2A/3$ where $A \equiv N_F\alpha/\pi$. The beta function can be re-arranged as an expansion of $1/N_F$:

$$\frac{3}{2}\frac{\beta(\alpha)}{A} = 1 + \sum_{i=1}^{\infty} \frac{F_i(A)}{N_F^i}. \tag{2.11}$$

We can re-sum the fermion bubble chain diagrams (Fig. 2.2) to obtain the leading $1/N_F$ contribution F_1 [27, 28]:

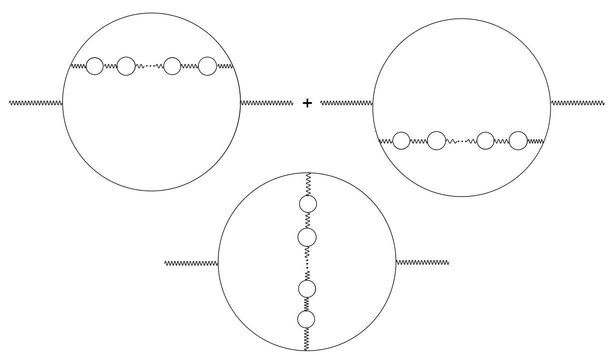

Figure 2.2: Diagrams of the fermion bubble chain [27].

$$F_1(A) = \int_0^{\frac{A}{3}} I_1(x)dx, \tag{2.12}$$

with

$$I_1(x) = \frac{(1+x)\,(2\,x-1)^2\,(2\,x-3)^2 \sin(\pi\,x)^3\,\Gamma\,(x-1)^2\,\Gamma\,(-2\,x)}{(x-2)\,\pi^3}. \tag{2.13}$$

One can handle the integration with the Cauchy principal value prescription. The result is shown in Figure 2.3. The poles are at $A = 15/2 + 3n$ for integer $n \geq 0$. The first singularity at $A = 15/2$ gives rise to an interacting UV fixed point for a large enough N_F.

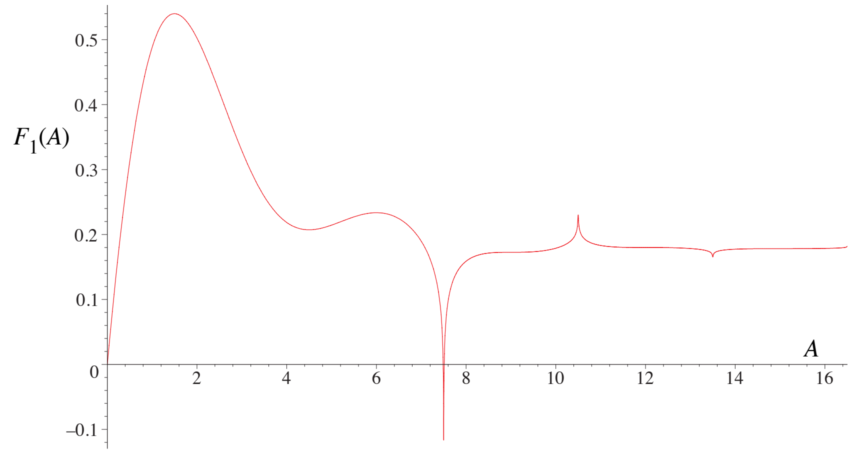

Figure 2.3: $F_1(A)$ as defined in (2.12).

For non-abelian gauge theory $SU(N_C)$, the beta function in $1/N_F$ expansion is:

$$\frac{3}{2}\frac{\beta(\alpha)}{A} = 1 + \sum_{i=1}^{\infty} \frac{H_i(A)}{N_F^i}. \tag{2.14}$$

where $A = N_F T_R \alpha/\pi$ with $T_R = 1/2$. Holdom [26] derived from [28] that

$$H_1(A) = -\frac{11}{4}\frac{C_G}{T_R} + \int_0^{A/3} I_1(x) I_2(x) dx, \tag{2.15}$$

$$I_2(x) = \frac{C_R}{T_R} + \frac{(20 - 43\,x + 32\,x^2 - 14\,x^3 + 4\,x^4)}{4\,(2\,x-1)\,(2\,x-3)\,(1-x^2)}\frac{C_G}{T_R}, \tag{2.16}$$

where the Lie factors are $C_G = N_C$, $C_R = (N_c^2 - 1)/2N_c$. The result is illustrated in Figure 2.4. The poles are at $A = 3, 15/2, \cdots, 3n + 9/2$. The first singularity at $A = 3$

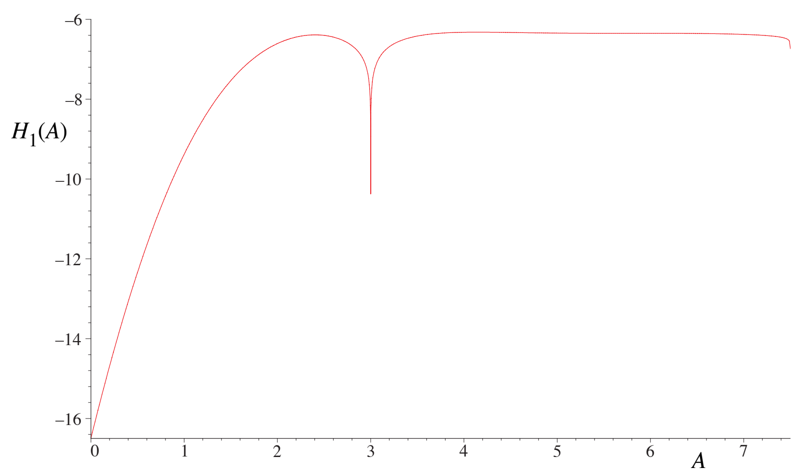

Figure 2.4: $H_1(A)$ as defined in (2.15).

gives rise to an interacting UV fixed point as long as N_F is large enough so that the leading $1/N_F$ order contribution dominates. Note that the pole structures are independent of the renormalization scheme [29]. We will use the resulted UV fixed points to construct asymptotically safe extensions of the SM in Chapter 5.

Another kind of study on the large-N_F bubble chain shown in Fig 2.2 is in the context of the QCD perturbative expansion resummation related to the infrared Landau pole in the running coupling, assuming N_F is large enough for the dominance of bubble chain contribution. In the bubble chain approximation, the running of coupling induces a factorial divergence in the perturbative expansion coefficients, generating a set of singularities referred to as renormalons in the Borel transform. The difference between the contour choices in the Borel integration, the so-called renormalon ambiguity, gives a power-like correction, which hints some non-perturbative effects possibly missed from the perturbative expansion. In contrast, there is no no ambiguities in the results of the large N_F program we are studying here, since there is no infrared Landau pole for the coupling running and and the bubble chain dominance is not ad hoc.

2.4 UV completion with Gravity

Serious problems emerge when Einstein's gravity meets quantum physics. Firstly, Einstein's gravity suffers from the non-renormalizability problem, in which the graviton scattering amplitudes tend to diverge in the deep UV. A way to get around this problem is to treat Einstein's gravity as merely an effective field theory at the low energy scale. Eventually, some unknown UV completion should cure the non-renormalizability problem. Secondly, S. Hawking found the black hole information paradox that the evolution of quantum entanglement is not unitary in the black hole background. Any candidate theory of UV completion should address these two problems at least.

It turns out both problems can be resolved by the theory of quadratic gravity [32, 33], in which the second-order of Ricci scalar and Ricci curvature terms are included, in addition to the Einstein-Hilbert action. It turns out that the gravitational couplings of quadratic gravity are weakly coupled with the matter sector at UV, and thus will not help removing the Landau pole of the SM. Therefore, the Landau pole problem in the SM has to be resolved by the SM sector its own. This can be achieved by constructing UV fixed points for the SM sector, as introduced in previous sections. In this way, a complete and well-defined quantum field theory of the SM and the gravity can be extrapolated to infinite energy scales. However, the spectrum of quadratic gravity has a notorious ghost, for which the sign of propagator is negative, potentially ruining the unitarity and stability of the theory. Although the issue of ghost has not been settled in a widely-accepted way, some recent studies argued that the problems of unitarity and stability are avoided by showing that the ghost does not appear in the asymptotic spectrum [34], with only some acausal behaviour left that can not be observed due to its extremely short timescale [35].

Chapter 3

Overview of QCD dense Matter

In this chapter, we introduce some background knowledge on QCD dense matter related to our study of quark matter later in chapter 6.

The fundamental building blocks of QCD are quarks and gluons. At low density, quarks and gluons are in the form of hadrons like protons and neutrons. When the density gets higher, some exotic phases of matter may appear. In order to study the baryonic matter in the high density regime, we first recall some related basic knowledge of thermodynamics. Then we recap the role of chiral symmetry in the low energy QCD dynamics, with the linear sigma model presented as an effective description. After that, we introduce the current understanding and modelling of hadronic matter and quark matter. Finally, we review the related study on compact stars that are composed of either hadronic matter or quark matter.

3.1 Thermodynamics Basics

In thermodynamics, the grand potential (free energy) of a system is

$$\Omega = E - TS - \mu N, \tag{3.1}$$

where E is the (internal) energy. T, S, μ, N are the temperature, entropy, chemical potential, and the particle number, respectively. The differential form of Eq. (3.1) reduces to

$$d\Omega = -SdT - PdV - Nd\mu \tag{3.2}$$

using the fundamental thermodynamics equation

$$dE = TdS - PdV + \mu dN, \tag{3.3}$$

with P as the pressure and V as the volume. Therefore, the number density n has the relation

$$n = \frac{N}{V} = -\frac{1}{V}\frac{\partial\Omega}{\partial\mu}. \tag{3.4}$$

Besides, with Eq. (3.1) and the Euler's equation

$$E = TS - PV + \mu N, \tag{3.5}$$

one obtains the simple relation

$$P = -\frac{\Omega}{V} = n\mu - \rho \tag{3.6}$$

at $T = 0$. An alternative derivation is from Eq. (3.3)

$$\begin{aligned} P &= -\frac{\partial E}{\partial V} = -\frac{\partial E}{\partial(N/n)} = n^2\frac{\partial(\rho/n)}{\partial n} & (3.7)\\ &= n\mu - \rho & (3.8) \end{aligned}$$

with relation $\mu = d\rho/dn$ substituted. Thus,

$$\mu = \rho/n = E/N \text{ at } P = 0. \tag{3.9}$$

In the following study, we absorb the volume factor into the grand potential and set temperature $T = 0$.

3.2 Chiral Symmetry and the Linear Sigma model

Gellmann and Levy [10] proposed the linear sigma model for the nucleon interactions. This model can be recast as a more fundamental picture in terms of quarks. It encompasses an $SU(N_f)_L \times SU(N_f)_R$ global chiral symmetry, which is the basic ingredient of QCD with N_f massless quark flavours. This chiral symmetry is spontaneously broken into the diagonal $SU(N_f)_V$ group by the non-zero vacuum expectation values of the σ field at the potential minimum.

The Lagrangian for the linear sigma model [10, 36, 38] is:

$$\mathcal{L} = \mathrm{Tr}\left(\partial_\mu\Phi^\dagger\partial^\mu\Phi\right) - V(\Phi), \tag{3.10}$$

with the scalar potential

$$V(\Phi) = V_{\rm inv}(\Phi) + V_b(\Phi), \tag{3.11}$$

where $V_{\rm inv}$ is the chiral invariant part:

$$V_{\rm inv} = \lambda_1 \left(\mathrm{Tr}\ \Phi^\dagger\Phi\right)^2 + \lambda_2\, \mathrm{Tr}\left(\Phi^\dagger\Phi\Phi^\dagger\Phi\right) + m^2\, \mathrm{Tr}\left(\Phi^\dagger\Phi\right) + c\left(\det\Phi + \det\Phi^\dagger\right).$$

The c term is the t'Hooft term that signals $U(1)_A$ breaking. V_b includes the terms that explicitly break the chiral symmetry. We denotes

$$\Phi = T_a\Phi_a = T_a\left(\sigma_a + i\pi_a\right), \tag{3.12}$$

where $T_a = \lambda_a/2$ with $a = 0, \ldots, 8$ are the nine generators of the $U(3)$, with $\lambda_a = 1 \sim 8$ the Gell-Mann matrices and $\lambda_0 = \sqrt{\frac{2}{3}}\,\mathbf{1}$. The generators T_a are normalized to $\mathrm{Tr}(T_aT_b) = \delta_{ab}/2$ and obey the $U(3)$ algebra $[T_a, T_b] = if_{abc}T_c$ and $\{T_a, T_b\} = d_{abc}T_c$. d_{abc} and f_{abc} are the symmetric and antisymmetric structure constants respectively, with $f_{ab0} = 0$, $d_{ab0} = \sqrt{\frac{2}{3}}\delta_{ab}$. σ_a and π_a form the scalar and pseudoscalar meson nonets:

$$\begin{aligned} T_a\sigma_a &= \frac{1}{\sqrt{2}}\begin{pmatrix} \frac{1}{\sqrt{2}}\,a_0^0 + \frac{1}{\sqrt{6}}\,\sigma_8 + \frac{1}{\sqrt{3}}\,\sigma_0 & a_0^- & \kappa^- \\ a_0^+ & -\frac{1}{\sqrt{2}}\,a_0^0 + \frac{1}{\sqrt{6}}\,\sigma_8 + \frac{1}{\sqrt{3}}\,\sigma_0 & \bar{\kappa}^0 \\ \kappa^+ & \kappa^0 & -\frac{2}{\sqrt{3}}\,\sigma_8 + \frac{1}{\sqrt{3}}\,\sigma_0 \end{pmatrix}, \\ T_a\pi_a &= \frac{1}{\sqrt{2}}\begin{pmatrix} \frac{1}{\sqrt{2}}\,\pi^0 + \frac{1}{\sqrt{6}}\,\pi_8 + \frac{1}{\sqrt{3}}\,\pi_0 & \pi^- & K^- \\ \pi^+ & -\frac{1}{\sqrt{2}}\,\pi^0 + \frac{1}{\sqrt{6}}\,\pi_8 + \frac{1}{\sqrt{3}}\,\pi_0 & \bar{K}^0 \\ K^+ & K^0 & -\frac{2}{\sqrt{3}}\,\pi_8 + \frac{1}{\sqrt{3}}\,\pi_0 \end{pmatrix}. \end{aligned}$$

Here the charged and neutral pions are $\pi^\pm \equiv (\pi_1 \pm i\,\pi_2)/\sqrt{2}$ and $\pi^0 \equiv \pi_3$, respectively. For kaons, $K^\pm \equiv (\pi_4 \pm i\,\pi_5)/\sqrt{2}$, $K^0 \equiv (\pi_6 + i\,\pi_7)/\sqrt{2}$, and the conjugate $\bar{K}^0 \equiv (\pi_6 - i\,\pi_7)/\sqrt{2}$. The remaining pseudoscalar components π_0 and π_8 mix into the η and η' meson. For scalar mesons, a_0 and κ are the parity partners of pion and kaon, respectively. The remaining scalar components σ_0 and σ_8 mix into the σ and the f_0.

The minimal model includes the following linear term [36, 38]

$$V_b = \mathrm{Tr}\left[H(\Phi + \Phi^\dagger)\right], \tag{3.13}$$

where $H = T_ah_a$. Here h_a are external fields that explicitly break the chiral symmetry. More explicitly, h_8 is responsible for breaking the degeneracy between strange and non-strange sectors, while h_3 is responsible for the isospin breaking of the non-strange sector.

In the following discussion, we focus on the isospin-symmetric case where $h_3 = 0$.

The potential can induce spontaneous symmetry breaking so that Φ field obtains an expectation value

$$\langle\Phi\rangle \equiv T_a\,\bar{\sigma}_a \equiv T_0\,\bar{\sigma}_0 + T_8\,\bar{\sigma}_8, \tag{3.14}$$

with

$$\frac{\partial V}{\partial\bar{\sigma}_0} = 0, \qquad \frac{\partial V}{\partial\bar{\sigma}_8} = 0. \tag{3.15}$$

at the vacuum. The non-strange (σ_n) and strange (σ_s) flavour basis has the relation:

$$\begin{pmatrix}\sigma_n\\ \sigma_s\end{pmatrix} = \frac{1}{\sqrt{3}}\begin{pmatrix}\sqrt{2} & 1\\ 1 & -\sqrt{2}\end{pmatrix}\begin{pmatrix}\sigma_0\\ \sigma_8\end{pmatrix}, \tag{3.16}$$

so that Eq. (3.14) converts to

$$\langle\Phi\rangle \equiv \frac{1}{2}\mathrm{diag}(\bar{\sigma}_n, \bar{\sigma}_n, \sqrt{2}\bar{\sigma}_s). \tag{3.17}$$

The PCAC relation gives

$$\bar{\sigma}_0 = (f_\pi + 2\,f_K)/\sqrt{6}, \quad \bar{\sigma}_8 = \frac{2}{\sqrt{3}}\,(f_\pi - f_K)\,. \tag{3.18}$$

With Eq. (3.16), these lead to

$$\bar{\sigma}_n = f_\pi, \qquad \bar{\sigma}_s = \sqrt{2}f_K - \frac{f_\pi}{\sqrt{2}}. \tag{3.19}$$

The mass spectra of scalar and pseudo-scalar mesons are:

$$(m_S^2)_{ab} = \frac{\partial^2 V}{\partial\sigma_a\partial\sigma_b},\ (m_P^2)_{ab} = \frac{\partial^2 V}{\partial\pi_a\partial\pi_b}, \tag{3.20}$$

with $m_{a_0} = (m_S)_{11} = (m_S)_{22} = (m_S)_{33}$, $m_\kappa = (m_S)_{44}$; $m_\pi = (m_P)_{11} = (m_P)_{22} = (m_P)_{33}$, $m_K = (m_P)_{44}$. By the diagonalization of the (0, 8) elements, we obtain the masses of (σ, f_0) for the scalar sector and those of (η', η) for the pseudo-scalar sector:

$$\begin{aligned} m_{\phi_1}^2 &= (m_i^2)_{00}\cos^2\theta_i + (m_i^2)_{88}\sin^2\theta_i + (m_i^2)_{08}\sin 2\theta_i, \\ m_{\phi_2}^2 &= (m_i^2)_{00}\sin^2\theta_i + (m_i^2)_{88}\cos^2\theta_i - (m_i^2)_{08}\sin 2\theta_i \end{aligned}$$

with a defining relation for θ_i:

$$\tan 2\theta_i = \frac{2\,(m_i^2)_{08}}{(m_i^2)_{00} - (m_i^2)_{88}}, \tag{3.21}$$

where $i = S, (\phi_1, \phi_2) = (\sigma, f_0)$ for the scalar sector, and $i = P, (\phi_1, \phi_2) = (\eta', \eta)$ for the pseudo-scalar sector. The results of couplings $(\lambda_1, \lambda_2, m^2, c, h_0, h_8)$ are obtained by solving Eq. (3.15), Eq. (3.20), and Eq. (3.21) as the functions of two decay constants $(f_\pi,\ f_K)$ and four of the eight meson masses $(m_\pi,\ m_K,\ m_\eta,\ m_{\eta'},\ m_\sigma,\ m_{f0},\ m_\kappa,\ m_{a0})$. We present a benchmark with $(f_\pi, f_K, m_\pi, m_K, \sqrt{m_\eta^2 + m_{\eta'}^2}, m_\sigma) = (92.4, 113, 138, 496, 1103.6, 600)$ MeV [37, 38]. The solution for the coupling values is shown in Table 3.1.

λ_1	λ_2	$m^2\,(\text{MeV}^2)$	$c\,(\text{MeV})$	$h_0\,(\text{MeV}^3)$	$h_8\,(\text{MeV}^3)$
1.400	46.484	$(342.523)^2$	4807.835	$(286.094)^3$	$-(310.960)^3$

Table 3.1

This minimal model gives the right mass predictions for η and η', but yields the values of m_{a0}, m_{f0}, m_κ larger than 1 GeV. The difficulty on fitting all scalar meson masses below 1 GeV is a common problem for any known variation of the linear sigma model when only the linear term is included in the explicit breaking sector, no matter taking variations with a large departure on inputs data [39], including vector mesons, or replacing the t'Hooft term by the Veneziano-Witten term [40]. This deficiency motivates us to extend the explicit breaking sector. We will present our related work in Appendix A.

3.3 Nuclear Matter

In this section, we introduce the basic properties of nuclear matter that constrain the nuclear model building. Then we introduce some basic models of nuclear matter, capturing the fundamental physics and satisfying the introduced properties.

3.3.1 Properties

The total mass of an atomic nucleus composed of protons and neutrons can be described by the relation

$$m = Zm_p + Nm_n - E_B, \tag{3.22}$$

where m_p and m_n are the rest mass of a proton and a neutron, with Z and N denoting their numbers respectively. E_B is the binding energy of the nucleus. The semi-empirical mass formula (the Bethe-Weizsäcker mass formula) approximates E_B as

$$E_B(A, Z) = a_V A - a_S A^{2/3} - a_C \frac{Z(Z-1)}{A^{1/3}} + a_{\rm sym} I^2 A, \tag{3.23}$$

where $A = Z + N$ is the baryon number, and $I = (N - Z)/A$ is the isospin asymmetry parameter. The coefficients $(a_V, a_S, a_C, a_{\rm sym})$ denote the volume, surface, Coulomb, isospin contributions, respectively. The values of these coefficients are determined by fitting experimental data of nuclei masses [41, 42, 43], giving

$$(a_V, a_S, a_C, a_{\rm sym}) = (15.76, 17.81, 0.711, 23.7) \tag{3.24}$$

within a few percent uncertainty, depending on how they are fitted to the nuclear data. Note that $a_V \sim 16\,\mathrm{MeV}$ indicates the largest binding energy for isospin-symmetric case with the Coulomb contribution turned off. The analysis of electron-nucleus scattering determines the number density at saturation limit to be $n_0 \approx 0.16\,\mathrm{fm}^{-3}$. Any theory of nuclear matter should meet this minimal set of constraints on binding energy and number density at the saturation limit.

The compression modulus K is defined as:

$$K = 9[n^2 \frac{d^2}{n^2}(\frac{\rho}{n})]_{n=n_o} \tag{3.25}$$

characterizing the stiffness of the equation of state, which directly influences the maximum mass of the compact star that the nuclear matter compose. A direct measurement of K is from the giant monopole excitation in nuclei, which constrains K to the range $K = 200 - 300$ MeV. Recent nuclear data suggests $K \approx 234\,\mathrm{MeV}$.

The nucleon effective mass m^* at the saturation density is expected to lie within the range $0.7 m_N \sim 0.8 m_N$ from the analysis of neutron scattering with Pb nuclei.

Varying Eq. (3.23) with respect to charge Z, one obtains the $Z(A)$ function for the most stable configuration:

$$Z_{\rm min} = \frac{2 a_{\rm sym} A}{a_C A^{2/3} + 4 a_{\rm sym}}. \tag{3.26}$$

3.3.2 The Walecka Model and the GM model

The original version of the Walecka model [44] has the form:

$$\begin{aligned}\mathcal{L} = &\bar{\psi}\left(i\not{\partial} - (m - g_\sigma\sigma)\right)\psi + \frac{1}{2}\left(\partial^\mu\sigma\partial_\mu\sigma - m_\sigma^2\sigma^2\right) - \frac{1}{3}mb\left(g_\sigma\sigma\right)^3 - \frac{1}{4}c\left(g_\sigma\sigma\right)^4 \\ &- \frac{1}{4}\omega^{\mu\nu}\omega_{\mu\nu} + \frac{1}{2}m_\omega^2\omega^\nu\omega_\nu,\end{aligned} \tag{3.27}$$

where σ and ω_ν are the scalar meson and vector meson coupled to baryon ψ, respectively. From the Lagrangian above, one can write down the equations of motion (EOM) and solve the system with the charge neutrality and chemical equilibrium conditions. In the bulk (large particle number) limit, one can take the relativistic mean-field approximation where the scalar and vector fields are replaced by their mean values. The EOM thus become:

$$\begin{aligned} g_\sigma\sigma &= -(\frac{g_\sigma}{m_\sigma})^2\langle\bar{\psi}\psi\rangle - mbg_\sigma^2\left(g_\sigma\sigma\right)^2 - c\,g_\sigma^2\left(g_\sigma\sigma\right)^3, \\ g_\omega\omega_0 &= (\frac{g_\omega}{m_\omega})^2\langle\bar{\psi}\gamma_0\psi\rangle, \\ g_\omega\omega_k &= 0,\end{aligned} \tag{3.28}$$

where

$$\langle\bar{\psi}\psi\rangle = \frac{\partial E}{\partial m} = \frac{4}{(2\pi)^3}\int_0^{p_F} d^3p\frac{m}{\sqrt{p^2+m^2}} \tag{3.29}$$

is the scalar density, and

$$\langle\bar{\psi}\gamma_0\psi\rangle = \langle\psi^\dagger\psi\rangle = n = 2\int_0^{p_F}\frac{d^3p}{(2\pi)^3} = \frac{p_F^3}{3\pi^2} \tag{3.30}$$

is the vector density in the Thomas-Fermi approximation where the mass varies very slowly compared to the scale of the fermion Compton wavelength.

From Eq. (3.28), one can observe that for the Yukawa couplings and the meson masses, only their ratios $x_\sigma = g_\sigma/m_\sigma$, $x_\omega = g_\omega/m_\omega$ are relevant to the EOM. They can be used to fit the parameters of bulk nuclear property, such as the binding per nucleon a_V and the saturation density n_0, as discussed in section 3.3.1. The two scalar self-interaction b and c terms are needed to fit (K, m^*). And $x_\rho = g_\rho/m_\rho$ is needed to fit $a_{\rm sym}$ further.

The generalized model is the GM model [45]:

$$\mathcal{L} = \sum_B \bar{\psi}_B \left(i\partial\!\!\!/ - m_B\right)\psi_B + \frac{1}{2}\left(\partial^\mu\sigma\partial_\mu\sigma - m_\sigma^2\sigma^2\right) - \frac{1}{4}\omega^{\mu\nu}\omega_{\mu\nu} + \frac{1}{2}m_\omega^2\omega^\nu\omega_\nu$$
$$+ \frac{1}{2}m_\rho^2\boldsymbol{\rho}^\mu\boldsymbol{\cdot}\boldsymbol{\rho}_\mu - \sum_B\Big(g_{\sigma B}\bar{\psi}_B\sigma\psi_B + g_{\omega B}\bar{\psi}_B\omega\!\!\!/\psi_B + g_{\rho B}\bar{\psi}_B\gamma^\mu\boldsymbol{\tau}\boldsymbol{\cdot}\boldsymbol{\rho}_\mu\psi_B\Big)$$
$$- \frac{1}{3}m_N b\left(g_\sigma\sigma\right)^3 - \frac{1}{4}c\left(g_\sigma\sigma\right)^4 + \sum_{L=e^-,\,\mu^-}\bar{\psi}_L\left(i\partial\!\!\!/ - m_L\right)\psi_L.$$

The sum over B spans all the lowest baryon octet ($p, n, \Lambda, \Sigma^+, \Sigma^-, \Xi^-, \Xi^0$) and Δ quartet. Fitting $(n_0, a_V, K, m^*/m_N, a_{\rm sym}) = (0.153, 16.3, 300, 0.7, 32.5)$ gives $x_\sigma = g_\sigma/m_\sigma = 3.434$, $x_\omega = 2.674$, $x_\rho = 2.100$, $b = 0.00295$, and $c = -0.00107$ for the non-hyperonic matter. For the hyperonic matter, the hyperon-meson coupling to mass ratios determined from the empirical Λ binding energy ($\approx 28\,\mathrm{MeV}$) are $x_{\sigma H} = 0.6, x_{\omega H} = 0.6, x_{\rho H} = 0.653$. These solutions are the widely-used parameter sets of non-hyperonic and hyperonic GM1 model, respectively.

Hadronic stars with the non-hyperonic GM1 EOS have maximum mass $2.36\,M_\odot$, while those with hyperonic GM1 EOS have the maximum mass $\sim 1.65\,M_\odot$. The reduction of maximum mass by the hyperonic composition is a general feature in compact star physics, which we will elaborate more in Section 3.5.

3.4 Quark Matter

Unlike hadrons where quarks are confined, it is also possible for quarks to have the deconfined form, i.e. the so-called quark matter (QM). To study this state, we need to incorporate the essential ingredients of QCD, which result in two categories of approaches: (1) Dynamical approaches like the NJL model and the Dyson-Schwinger formalism, where non-perturbative effects need to be solved self-consistently. (2) Phenomenological Models like the MIT bag model, where a crude bag constant is introduced to account for the non-perturbative contribution of the QCD vacuum, and the quark-meson model, where an effective meson potential replaces the bag constant. Though being rather phenomenological, the quark-meson model captures more realistic dynamics of the QCD vacuum, like the flavour dependence and density dependence, compared to the conventional bag model.

3.4.1 The MIT bag model

The MIT bag model [46, 47] is the most-used model for the study of quark matter. It was originally proposed to model hadrons, in which all quarks are confined in a bag-like configuration. A bag constant B is introduced to account for all the non-perturbative effects of QCD vacuum. Later people applied this model to the study of quark matter [48, 55]. The total energy density of the quarks confined in the bag is given by [49]

$$\epsilon = \sum_f \epsilon^f + B. \tag{3.31}$$

where ϵ^f denotes the kinetic energy contribution of individual quark or lepton flavour f. The pressure from the bag constant together with the external pressure P counterbalance the internal pressure of P^i of the individual quarks and leptons contained in the bag:

$$P + B = \sum_f P^f, \tag{3.32}$$

We know that the relativistic gas has an EOS $P_f = \epsilon^f/3$, so that one obtains for this massless case the equation of state (EOS).

$$P = (\epsilon - 4B)/3, \tag{3.33}$$

so that $\epsilon = 4B$ at zero pressure.

For the non-interacting Fermi gas, we can take the integral form of Eq. (3.1) for each fermion flavour f:

$$\begin{aligned} \Omega_f &= \frac{2}{(2\pi)^3} \sum_f \int_0^{\sqrt{\mu_f^2 - m_f^2}} d^3p \, (\sqrt{p^2 + m_f^2} - \mu_f) \\ &= -\frac{1}{4\pi^2} \left[\mu_f (\mu_f^2 - m_f^2)^{1/2} \left(\mu_f^2 - \frac{5}{2} m_f^2 \right) + \frac{3}{2} m_f^4 \ln \frac{\mu_f + (\mu_f^2 - m_f^2)^{1/2}}{m_f} \right]. \end{aligned} \tag{3.34}$$

And correspondingly

$$P^f = \frac{c_f}{6\pi^2} \int_0^{p_{Ff}} dp \, \frac{p^4}{\sqrt{p^2 + m_f^2}}, \quad \rho^f = \frac{c_f}{2\pi^2} \int_0^{p_{Ff}} dp \, p^2 \sqrt{p^2 + m_f^2}, \quad n^f = \frac{c_f}{6\pi^2} p_{Ff}^3, \tag{3.35}$$

where $c_f = 2$ (spin) $\times$ 3(colour) for quarks, and $c_f = 2$ (spin) for the colour-singlets like leptons, and $p_{Ff} = \sqrt{\mu_f^2 - m_f^2}$ is the Fermi momentum. Note that these integrals can be completed into closed forms, and they obey the thermodynamics relation Eq. (3.8). The relativistic limit of Eq. (3.35) takes the simple form

$$P^f = \frac{\mu_f^4}{4\pi^2}, \quad \rho^f = 3\frac{\mu_f^4}{4\pi^2}, \quad n^f = \frac{\mu_f^3}{\pi^2}. \tag{3.36}$$

Despite the simplicity of the original MIT bag model, it suffers from several problems [50]. The successful fit of the ordinary hadron masses results in a universal bag constant value of $B_{\rm MIT} \approx 56\,{\rm MeV/fm^3}$. However, both the QCD sum rules and the QCD phase transition at high temperatures indicate a much larger bag constant value. Besides, the bag model has the "dihyperon **H**" problem, where an **H** particle with $(uds)^2$ composition is predicted by the bag model to have a mass smaller than two times $\Lambda\,(uds)$ mass. And with some parameter space, it can be smaller than two times the neutron mass. However, no experimental evidence has been found for the existence of **H**. All these sicknesses question the universality of the bag constant. It is thus very possible that B does depend on the density, colour, flavour, temperature, etc. In the next section, we present the quark-meson model, which can account for the density-dependent and flavour-dependent feedback of the quark gas on the QCD vacuum.

3.4.2 The Quark-Meson Model

In the quark-meson model, the effective bag constant of the bag model is replaced by the meson potential, which can account for the physical properties of QCD vacuum like the flavour dependence and the density dependence where the conventional bag model fails. The starting Lagrangian takes the form [51]

$$\mathcal{L}_Q = \bar{\Psi}\left(i\partial\!\!\!/ - g_\Phi \Phi\right)\Psi + {\rm Tr}\left(\partial_\mu \Phi^\dagger \partial^\mu \Phi\right) - V(\Phi), \tag{3.37}$$

where $V(\Phi)$ is the meson potential Eq. (A.2) with the meson multiplet Φ, Eq. (A.3). A general framework to apply this quark-meson model to the study of quark matter at bulk limit (infinite baryon number) is as follows: one can transform the meson potential from original octet-singlet basis (σ_0, σ_8) to the non-strange (σ_n) and strange (σ_s) flavour basis:

$$\begin{pmatrix}\sigma_n \\ \sigma_s\end{pmatrix} = \frac{1}{\sqrt{3}}\begin{pmatrix}\sqrt{2} & 1 \\ 1 & -\sqrt{2}\end{pmatrix}\begin{pmatrix}\sigma_0 \\ \sigma_8\end{pmatrix}, \tag{3.38}$$

In the mean field approach, the equations of motion ares obtained from $\partial\Omega/\partial\sigma_i = 0$, where $\Omega = \Omega_f + V(\Phi)$ with Ω_f defined in Eq. (3.34). Thus,

$$\frac{\partial V}{\partial \sigma_n} = -\sum_{i=u,d} g < \bar{\psi}_i \psi_i >, \tag{3.39}$$

$$\frac{\partial V}{\partial \sigma_s} = -g_s < \bar{\psi}_s \psi_s >, \tag{3.40}$$

where the right hand sides represent the quark condensates:

$$< \bar{\psi}_i \psi_i > \;=\; \frac{\partial \Omega_f}{\partial \sigma_i} = \frac{6}{(2\pi)^3} \int_0^{p_{F_i}} d^3p \frac{m_i}{\sqrt{p^2 + m_i^2}}, \tag{3.41}$$

with $m_{u,d} = g_n \sigma_n$ assuming isospin symmetry. The Fermi momentum for each flavour is $p_{Fi} = p_F {f_i}^{1/3}$, where the quark fractions are $f_i = n_i/(N_C n_A)$, $p_F = (3\pi^2 n_A)^{1/3}$ and n_A is the baryon number density. The quark scalar energy densities are [52, 53]

$$\rho_\psi \;=\; \sum_{i=u,d,s} \frac{2N_C}{(2\pi)^3} \int_0^{p_{Fi}} d^3p \sqrt{p^2 + m_i^2}, \tag{3.42}$$

$$\rho_\phi \;=\; \Delta V + \frac{1}{2} \sum_{i=n,s} (\nabla \sigma_i)^2, \tag{3.43}$$

where ΔV is the potential energy with respect to the vacuum. The flavour composition of the quark gas and the radius R can be determined by minimizing the total energy

$$E = \int_0^R d^3r (\rho_\psi + \rho_\phi). \tag{3.44}$$

The system is in chemical equilibrium with respect to the weak processes:

$$s \to u + e^- + \bar{\nu}_e, \qquad d \to u + e^- + \bar{\nu}_e. \tag{3.45}$$

Neglecting the chemical potential of the neutrino, the chemical equilibrium gives the relation

$$\mu_d = \mu_s = \mu_u + \mu_e, \tag{3.46}$$

where $\mu_i = \sqrt{p_{Fi}^2 + m_i^2}$. For the free-interacting fermion gas, it can be shown that the chemical equilibrium condition is equivalent to the energy minimization over flavour composition in charge neutral configuration. With the input parameters in Table. 3.1 for a benchmark study, the corresponding numerical solutions as the functions of the effective baryon Fermi momentum $p_F = (3\pi^2 n_A)^{1/3}$ are shown in Fig. 3.1, from which we

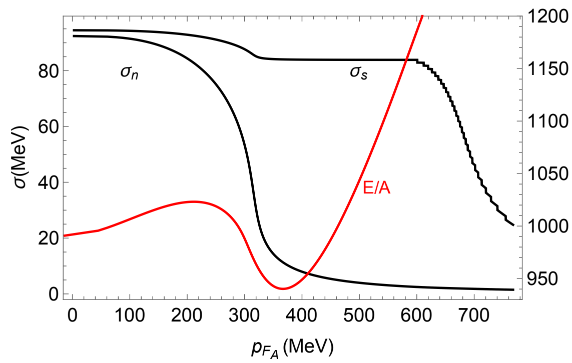

(a) The field values σ_n, σ_s (blue dashed, left axis) and the energy per baryon number ε (red solid, right axis) in the bulk limit.

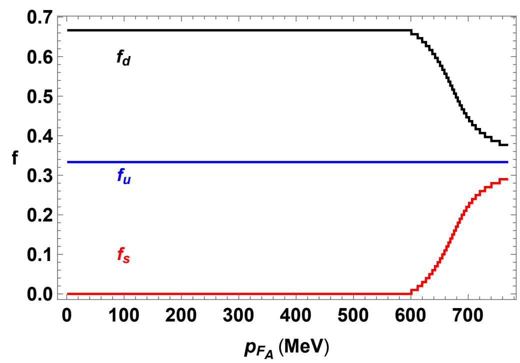

(b) The fractions of u, d, s quarks in the bulk limit

Figure 3.1

see that the minimum of E/A is at $p_F = \bar{p}_F \approx 383\,\mathrm{MeV}$ with $E/A \approx 940.2\,\mathrm{MeV}$. Besides, we see that no strange fraction appears at $\bar{p}_F$, which means the two-flavour quark matter is more stable than the three-flavour one, but neither is more stable than the ordinary nuclei. In Chapter 6, using this quark-meson model but with a more realistic meson potential, we obtain an E/A for the non-strange quark matter even smaller than 930 MeV for the most stable nuclei ^{56}Fe. The general feature that two-flavour is more stable than the three-flavour case is mainly due to the fact that the scalar potential is far more steep in the σ_s direction than it is in the σ_n direction, as shown in Figure 3.2.

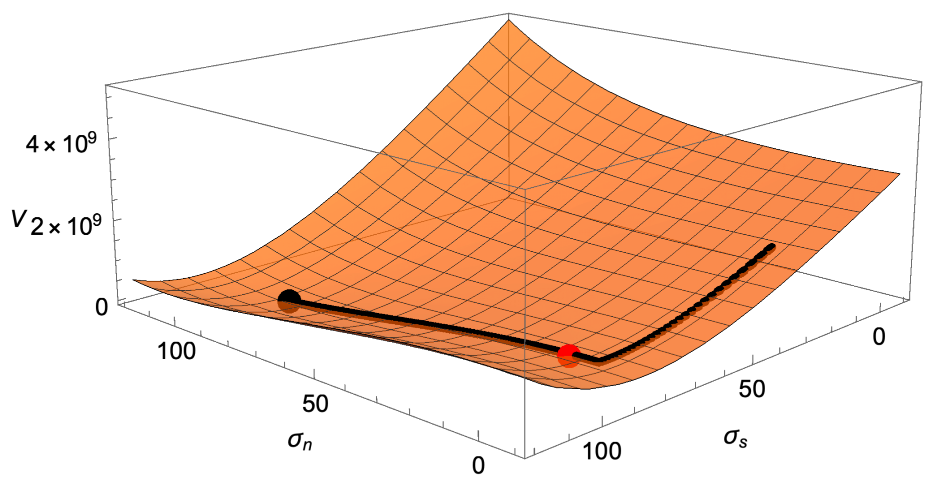

Figure 3.2: 3D plot of the scalar potential $V(\sigma_n, \sigma_s)$ (orange surface). The black line denotes the scalar field trajectory from the EOM solution. The black dot denotes the potential minimum, while the red dot maps to the E/A minimum. All axes are in units of MeV.

As we can see from Fig. 3.1a, at the limit of zero baryon number density, the scalar fields approach to their physical vacuum expectation values (VEVs). As the number density increases, the σ_n field tends to decrease rapidly towards the chiral limit where up and down quarks become almost massless so that the relativistic limit $p_F \gg m$ can be taken. The relativistic energy per baryon number has the form [19]:

$$\varepsilon = \frac{\rho}{n_A} = \frac{(\chi N_C p_F^4)/4\pi^2 + V_n}{n} = \frac{3}{4} N_C p_F \chi + 3\pi^2 V_n / p_F^3, \tag{3.47}$$

where $N_C = 3$ is the colour factor and $\chi = \sum_i f_i^{4/3}$ is the flavour factor. V_n is the contribution for the meson potential along the non-strange direction, which can be treated as the effective bag constant. The valley of V_n is very shallow compared to that of V_s, and its magnitude is insensitive to the density change before strangeness turns on. Thus, we can approximate V_n as a constant and minimize the energy with respect to p_F, from which one obtains

$$\varepsilon_{\min} = 3\sqrt{2\pi}\left(\chi^3 V_n\right)^{1/4}, \text{ at which } \bar{p}_F \approx \left(\frac{12\pi^2 V_n}{N_C \chi}\right)^{1/4}. \tag{3.48}$$

The formulas above give a good match to the exact numerical result with a mere error of a fraction of one percent due to the tiny quark mass.

3.4.3 Hypothesis of Absolutely Stable Quark Matter

Bodmer [54], Witten [55] and Terazawa [56] proposed that the strange quark matter (SQM) may be the true ground state of cold matter. This is the so-called "Strange Quark Matter Hypothesis". In the following we give a simple reasoning.

For the ud quark matter (udQM), charge neutrality requires $n_u \approx 1/2\, n_d$, which leads to $\mu_d = 2^{1/3}\mu_u$ from Eq. (3.36). Thus, for the bound state where the external pressure goes to zero, Eq. (3.32) leads to the bag constant

$$B_2 = \sum_{u,d} P^f = (1 + 2^{4/3})\mu_u^4 / 4\pi^2. \tag{3.49}$$

For the strange quark matter, the fraction of each flavour is the same, so that they share a common chemical potential $\bar{\mu}$. Hence the bag constant is

$$B_3 = \sum_{u,d,s} P^f = \frac{3\bar{\mu}^4}{4\pi^2}. \tag{3.50}$$

For a universal bag constant, $B_2 = B_3 = B$. Thus, the ratio of energy per baryon E/A, which equals the ratio of average chemical potential referred to Eq. (3.9), is

$$\frac{E/A\big|_3}{E/A\big|_2} = \frac{\bar{\mu}}{\frac{1}{3}\mu_u + \frac{2}{3}2^{1/3}\mu_u} = \left(\frac{3}{1+2^{4/3}}\right)^{3/4} \approx 0.89. \tag{3.51}$$

Therefore, this simple argument suggests that the three-flavour quark matter (SQM) is always more stable than the two-flavour case. To see how the bag constant affects the overall stability, note that the inverse of Eq. (3.49) tells $\mu_u = (\frac{4\pi^2}{(1+2^{4/3})}B_2)^{1/4}$, thus

$$E/A\big|_2 = 3(\frac{1}{3}\mu_u + \frac{2}{3}2^{1/3}\mu_u) = 934 \text{ MeV} \times \frac{B_2^{1/4}}{145\,\text{MeV}}. \tag{3.52}$$

Similarly, for the three-flavour case,

$$E/A\big|_3 = 3\bar{\mu} = 934 \text{ MeV} \times \frac{B_3^{1/4}}{162.8\,\text{MeV}}. \tag{3.53}$$

Note that the 934 MeV denotes the sum of the $E/A = 930\,\text{MeV}$ for the most stable nuclei ^{56}Fe and a 4 MeV correction due to the surface effects of quark matter lumps [48]. Therefore,

$$B_{\text{SQM}} \in [145^4, 162.8^4]\,\text{MeV}^4 \approx [57.8, 91.9]\,\text{MeV/fm}^3 \tag{3.54}$$

for the absolute stable SQM. Note that the lower bound guarantees the stability of ^{56}Fe over the nonstrange quark matter.

However, as we note, this conclusion crucially depends on the validity of the relativistic limit and the assumption of $B_2 = B_3$. Later it was found that B_2 actually is significantly smaller than B_3 in realistic models like the quark-meson model. We can observe this directly from Figure 3.2 that the meson potential height in non-strange direction is much shallower in strange direction, leading to $B_2 < B_3$ since the meson potential amounts to the effective bag constant. Therefore, it was shown the two-flavour quark matter, udQM, actually is more stable than the three-flavour quark matter [57, 58], and even normal nuclei when the baryon number A is sufficiently large above $A_{\text{min}} \gtrsim 300$ [19]. We will consider the related details in Chapter 6. Note that the large A_{min} ensures the stability of ordinary nuclei in the current periodic table.

3.4.4 Finite-size effect and A_{min}

When the particle number decreases from the bulk limit, the surface effect and Coulomb effect become more important and tend to destabilize the bound state. The energy can be approximated as the following general form[1]:

$$E = \sum_i (\Omega_V + n_i\mu_i)V + \sigma S + \frac{3}{5}\frac{Z^2}{R} \tag{3.55}$$

where $V = 4/3\pi R^3$, $S = 4\pi R^2$ for a spherical system. σ denotes the surface tension. With the surface information input in Eq. (3.55), one can determine $A_{\rm min}$ below which the state becomes unbounded. In general, a large E/A or σ will result in a large $A_{\rm min}$.

A commonly adopted way to account for the finite-size effect is to modify the density of states using the multiple reflection expansion (MRE) as $k^2\rho_{\rm MRE}/(2\pi^2)$ [59, 60, 61], where

$$\rho_{\rm MRE} = 1 + \frac{6\pi^2}{kR} f_S\left(\frac{k}{m}\right), \tag{3.56}$$

where R is the radius of the sphere. And

$$f_S = -\frac{1}{8\pi}\left(1 - \frac{2}{\pi}\arctan\frac{k}{m}\right), \tag{3.57}$$

represents the surface contributions. The finite-size effect enters into calculations through the replacement of phase space integrals:

$$\int_0^\Lambda \cdots \frac{k^2\,dk}{2\pi^2} \longrightarrow \int_{\Lambda_{IR}}^\Lambda \cdots \frac{k^2\,dk}{2\pi^2}\rho_{MRE}, \tag{3.58}$$

where the IR cut-off Λ_{IR} is the largest solution of the equation $\rho_{MRE}(k) = 0$ with respect to the momentum k. We note that the surface tension that determines the value of $A_{\rm min}$ has large uncertainties depending on the methods used and effects included. The conventional MIT bag model [60], NJL model [62, 63, 64], and the linear sigma model [65, 66, 67] generally predict small surface tension $\sigma < 30\,{\rm MeV/fm^2}$. However, large values are obtained for the NJL model with the aforementioned "multiple reflection expansion (MRE)" framework [62] ($\sigma = 145 \sim 165\,{\rm MeV/fm^2}$), and models including charge screening effect ($\sigma = 50 \sim 150\,{\rm MeV/fm^2}$) [68], though smaller or larger values are not strictly excluded. Constraints of surface tension from the recent LIGO gravitational wave events are studied in [69].

A more exact way to study the finite size effect is by fitting the energy formula Eq. (3.55) with the exact value of energy for each particle number. The $E(A)$ information can be derived from the equation of motion that is numerically solved at each particle

[1]We neglect the discussion of curvature contribution here.

number. The related calculation details are presented in Appendix B. We adopted this approach in the study of udQM [19] to determine $A_{\rm min}$ and the corresponding surface tension, giving $A_{\rm min} \approx 300$ with a surface tension $\sigma \approx 20\,\mathrm{MeV/fm}^2$ that is robust against parameter variations.

3.5 Compact Stars

Compact stars have large masses and small radii, which result in high density and pressure in the interior. White dwarfs (WDs) are the compact stars composed of relativistic electrons, the degenerate pressure of which counterbalances the gravity pull, resulting in an upper bound for their masses, the so-called "Chandrasekhar limit" around $1.4\,M_\odot$. Beyond the Chandrasekhar limit, the stars may further collapse to black holes or neutron stars (NSs) where the high compactness leads to the neutron abundance from the process

$$p + e^- \to n + \nu, \tag{3.59}$$

so that the degenerate pressure of the neutron gas balances the gravitational pull. Direct observational evidence of NSs is from the electromagnetic radiation emitted by highly magnetized rotating NSs or WDs. The mass measurements taken from binary pulsar systems via radio signals give the typical masses $M \sim 1.4 M_\odot$ with maximum masses above $2M_\odot$ [73, 74, 75], while the radii measurements from the X-ray extraction result in a large uncertainty $R = 6.8 - 13$ km. From these, one can estimate the average mass density to be around three times the density of heavy nuclei. For compact stars composed of hadrons, the density falls to the density of iron ($\sim 7.85\,\mathrm{g/cm}^3$) at the star surface.

A neutron star typically has an atmosphere and an interior divided into four regions: the outer crust, the inner crust, the outer core, and the inner core. The outer crust composed of ions and electrons extends from the surface to the neutron drip density $\rho_{\rm drip} \approx 0.22\,\mathrm{MeV/fm}^3$.[2] Free neutrons start to appear in the inner crust, which ranges from $\rho_{\rm drip}$ to roughly $0.5\rho_0$, where $\rho_0 \approx 157\,\mathrm{MeV/fm}^3$ is the saturation nuclear matter density. The outer core that varies from $0.5\rho_0$ to $2\rho_0$ is a mixture of protons, neutrons, electrons, and muons in β equilibrium. A heavier neutron star can have an inner core with $\rho > 2\rho_0$, where the exotics like hyperon, Δ resonance, or defined quarks may appear.

The EOS models in these layers are very complicated and have large uncertainties. Measurements of masses and radii, tidal deformability during star mergers, and other astrophysical observations can help pin down a more accurate picture of hadronic EOS.

[2] Units conversion $1\,\mathrm{MeV/fm}^3 \approx 1.783 \times 10^{12}\mathrm{g/cm}^3$.

To see how the astrophysical constraints of masses and radii can map to the EOSs or vice versa, one starts from the TOV equation [70, 71]

$$\frac{dp(r)}{dr} = -\frac{[m(r) + 4\pi r^3 p(r)]\,[\rho(r) + p(r)]}{r(r - 2m(r))}\,, \qquad \frac{dm(r)}{dr} = 4\pi\rho(r)r^2\,,$$

with the boundary condition $p(R) = 0, m(R) = M$ for a given central pressure P_C. From this, one can obtain the (M, R) solution as a function of P_C for a given matter EOS $P(\rho)$. Oppositely, one can utilize this mapping to constrain matter EOSs from the (M, R) information.

Hadronic Matter and Hadronic Star

We can approximate the hadronic matter EOS by a polytrope form in different layers of neutron star:

$$P = K\rho^{\gamma}. \tag{3.60}$$

Different values of K and γ encode the information about the hadronic matter composition of neutron stars. With this polytrope approximation, an analytical expression of $M - R$ can be obtained [72]

$$\begin{aligned} M &= -\xi_1^2\theta_1'(4\pi)^{-1/(\gamma-1)}\left(\frac{K\gamma}{G(\gamma-1)}\right)^{1/(2-\gamma)}\left(\frac{R}{\xi_1}\right)^{(4-3\gamma)/(2-\gamma)} \\ &\propto R^{(4-3\gamma)/(2-\gamma)}, \end{aligned} \tag{3.61}$$

where ξ and θ' are γ-dependent variables. At low density, the matter composition is dominated by the relativistic electron gas so that $\gamma \sim 4/3$, while $\gamma \sim 2$ at the high-density region (around n_s). From Eq. 3.61, we see that this $4/3 \lesssim \gamma \lesssim 2$ range means that the magnitude of M is negatively correlated with that of R. Another observation is that at the low-density limit $M \propto K^{3/2}$, which is independent of R, approaching the minimum neutron star mass $\sim 0.1M_{\odot}$. And $R \propto K^{1/2}$ at large density limit, which is independent of M. These determine the general shape of $M - R$ curve for the hadronic stars. A general feature is that a stiffer EOS gives a larger mass and a larger radius with a smaller central density n_c. Stars with $\rho_c > \rho_c(M_{\max})$ are unstable against any radial mode of oscillations, due to the imbalance of the gravitational attraction over the repulsive force resulting from the degenerate fermion matter.

In one family scenario where it is assumed that all compact stars are within one family of hadronic matter EOS, the discovery of pulsars with large masses above $2\,M_{\odot}$ [73, 74, 75] ruled out a large amount of soft EOSs. Furthermore, the recent gravitational wave observation of the binary neutron star merger event (GW170817) tells the tidal deformability $\Lambda < 800$, ruling out a large number of too-steep EOSs. In contrast, one can also utilize the constrained EOSs to pin down the astrophysical observables that have large experimental uncertainties. For example, the X-ray extraction suggests $6.8 \lesssim R_{1.4\,M_\odot}/\mathrm{km} \lesssim 13.8$, and later studies utilizing the constrained EOS obtained a much narrower range [76, 77, 78].

At high density (above $2n_s$), hyperons and Δ resonances are expected to appear in the star interiors, which tend to soften the EOS and thus make it difficult to get a star mass larger than $2\,M_\odot$, in conflict with with the observations of massive pulsars [73, 74, 75]. This is the so-called "hyperon puzzle". Moreover, the lower bound of the average tidal deformability $\tilde{\Lambda}$ in the one-family scenario excludes compact stars with small radii, which may have tension with what the X-ray analyses suggest [79]. Therefore, it is natural to expect that the stars with large masses and large radii are the quark stars (QSs) composed of quark matter, and most of the ones with small maximum mass and small radii are the hadronic stars (HSs). This possibility is the so-called "two-families" scenario.

Quark Matter and Quark Star

The EOS of quark matter has the linear form

$$P = ac^2(\rho - \rho_s). \tag{3.62}$$

Causality requires $a \leq 1$. In the relativistic limit, $a = 1/3$, which can get modified by the finite quark mass effect. ρ_s is the density at the surface where the pressure goes to zero, and thus $\rho_s = 4B$ in bag model from Eq. (3.33), or $\rho_s = 4\,B_{\mathrm{eff}}$ in other effective models like the quark-meson model. The simple linear form makes it possible to perform a dimensionless rescaling [83, 84]

$$\bar{\rho} = \frac{\rho}{\rho_s},\ \bar{p} = \frac{p}{\rho_s},\ \bar{r} = r\sqrt{\rho_s},\ \bar{m} = m\sqrt{\rho_s}, \tag{3.63}$$

so that the TOV solution of Eq. (7.5) is also dimensionless, and thus is independent of any specific value of B_{eff}. The results on $\bar{M} = M\sqrt{4\,B_{\mathrm{eff}}}$ and $\bar{R} = R\sqrt{4\,B_{\mathrm{eff}}}$ of quark stars are shown in Fig. 3.3a. The TOV solution of any other EOS with a different B_{eff} value can be obtained directly from rescaling the dimensionless solution back. The maximum mass and the corresponding radius are thus obtained: $M_{\max} \approx 15.17/\sqrt{B_{\mathrm{eff}}}\ M_\odot$, $R_{\mathrm{Mmax}} \approx 82.8/\sqrt{B_{\mathrm{eff}}}$ km, where B_{eff} takes value in units of $\mathrm{MeV/fm^3}$. For strange quark stars composed of SQS, $B_{\mathrm{eff}} = B_{\mathrm{SQM}} \in [57.8, 91.9]\,\mathrm{MeV/fm^3}$ referring to Eq. (3.54). The

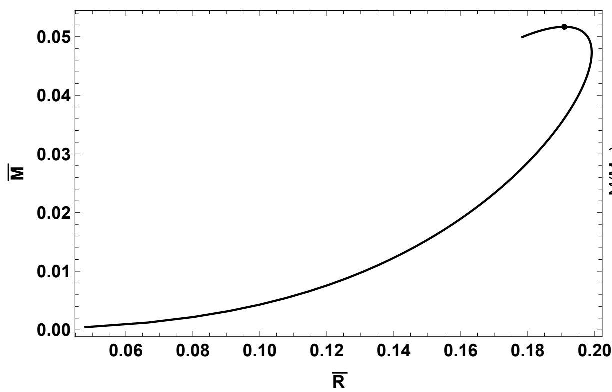

(a) The rescaled $\bar{M}$ vs radius $\bar{R}$ of quark stars. The black dot at $(\bar{M}, \bar{R}) = (0.0517, 0.191)$ denotes the maximum mass configuration.

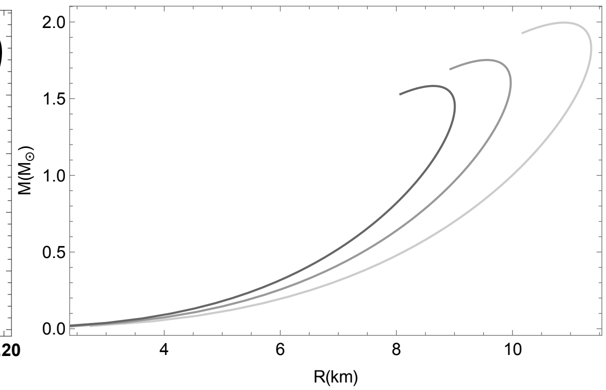

(b) The $M - R$ of SQSs. Lines with darker colour are with larger effective bag constant $B_{\rm eff}$, which samples $(57.8, 75, 91.9)\,{\rm MeV/fm^3}$ respectively.

Figure 3.3

explicit $M - R$ solution is shown in Fig. 3.3. The maximum mass that SQSs can possibly reach is $M_{\rm max} \approx 15.17/\sqrt{57.8}\ M_\odot \approx 1.99 M_\odot$. Therefore, SQSs based on the MIT bag model cannot satisfy the $2M_\odot$ constraint put by the experimental observations of massive pulsars [73, 74, 75], unless a large perturbative QCD (pQCD) effect or a colour-superconducting phase is included [80]. This difficulty can be naturally resolved by ud quark stars in the context of absolutely stable udQM. We will present the related details in Chapter 6 and Chapter 7.

Provided the hypothesis of stable quark matter is true, it is natural to expect that all compact stars are actually quark stars. On the one hand, one expects a rapid conversion from hadronic matter to quark matter inside compact stars due to the large energy difference and small surface tension between the two phases. On the other hand, the pollution of strangelet or udlet, a small chunk of SQM or udQM, may convert all hadronic stars into quark stars. There are many observation indications against this possibility, but most arguments tend to be model-dependent. For example, the phenomenon of the pulsar glitch, a sudden increase of pulsar spin frequency, observed in the pulsars like the Vela pulsar and the Crab pulsar, has been argued against the possibility that all pulsars are quark stars since conventional models of glitch phenomena involve a superfluid neutron state. However, there are some candidate models that have addressed this issue in the context of some particular forms of quark matter, such as the solid quake model [81], or the crystalline colour superconducting (CCSC) phase [82].

Chapter 4

UV: Stable Asymptotically Free Extensions of the Standard Model

In this chapter, we explore possible extensions of the Standard Model that are not only completely asymptotically free, but are such that the UV fixed point is completely UV attractive. We denote such extensions of the Standard Model as SAFEs. All couplings flow towards a set of fixed ratios in the UV. The fixed points can help relieving the notorious Landau pole problem, so that the extensions can be extrapolated to infinite energy scales. Motivated by low scale unification, semi-simple gauge groups with elementary scalars in various representations are explored, with a Pati-Salam type benchmark model. The text in this chapter is reproduced from [17].

4.1 Introduction

We start by considering an elementary Higgs boson in a world without low energy supersymmetry. In this world there are two conflicting demands on the nature of new physics on higher mass scales. Naturalness strongly constrains the new physics to prevent unwanted contributions to the Higgs mass. Either the new physics mass scale cannot be much higher than the Higgs mass or the Higgs coupling to the new physics must be extremely weak. The other demand on the new physics is that it must significantly alter the running of couplings, including the quartic coupling of the Higgs. This is because the Landau poles in the quartic coupling and the $U(1)$ hypercharge coupling would signal new mass scales of the dangerous type. To avoid this requires new massive degrees of freedom that do couple to standard model fields and thus are also dangerous for naturalness. These two demands are suggesting that if there is new physics to cure the Landau problem then it must enter at as low a scale as possible to minimize the naturalness problem.

The absence of Landau poles is a requirement for the theory to be UV complete, or in other words that there is a description of the theory on arbitrarily high energy scales in terms of elementary fields. The fermions and gauge bosons of asymptotically free gauge theories are prime examples of truly elementary fields. The standard model is not of this type, but it often thought that there is no reason it should be given the presence of gravity. The onset of gravitational effects at Planckian energies is usually taken to mean that the theory experiences a complete change of character on these scales. But once again this is at odds with naturalness. It is only if gravity somehow exerts only a very minimal effect on the scalar sector in a UV complete theory is there is any hope of naturalness.

There have been recent attempts to show how the effects of gravity in UV complete quantum field theories could be consistent with naturalness. Ref. [85] illustrated a proposed mechanism in a 2D model of quantum gravity. These authors introduce the concept of "gravitational dressing" of a QFT, where Planck mass effects modify the S-matrix directly without inducing any physical mass scales. Ref. [33] (see also [86]) suggests that the pure gravitational action in the high energy regime just contains two terms, an R^2 term and the Weyl term $\frac{1}{3}R^2 - R^2_{\mu\nu}$. The Einstein-Hilbert term is induced via the VEV of a new scalar field with non-minimal coupling to R. The point is that the gravitational interactions may then be both renormalizable and asymptotically free [32, 87, 88]. Ref. [33] argues that such a gravity sector could be arranged to couple sufficiently weakly to the standard model fields to preserve naturalness. The gravity sector here is not quite complete because of a ghost and a tachyon in the spectrum.

Our interest here is the other half of the problem, how to build UV complete quantum field theories containing truly elementary scalar fields. We approach this by searching for gauge theories containing both fermions and scalars where all couplings run to zero in the UV. This could provide a completely asymptotically free extension (CAFE) of the standard model. A nice study of this type was conducted long ago in [14]. There the constraints were found on theories with a simple gauge group with varying numbers of scalar fields in various representations and with fermions. Gauge, quartic and Yukawa couplings were considered. CAFEs were found and described in terms of UV fixed points (UVFPs) where ratios of couplings approached fixed values. The fixed points were also required to be UV attractive from all directions in coupling space. Thus these are CAFEs that also have complete UV stability, and we denote such an extension of the standard model as a SAFE. That such theories were found in [14] may have been of interest to the construction of grand unified theories. But the study showed that it was difficult for the scalars that were allowed to sufficiently break down the original gauge theory via the Higgs mechanism. For this reason and perhaps also because it was thought that gravity would nevertheless provide an ultraviolet cutoff, it appears that SAFEs were never considered to be of particular importance in GUTs.

Our work can be considered to be a continuation of this old work. Since we need to embed the standard model into a gauge group without a $U(1)$ factor at the lowest possible scale we are here dealing with low scale unification. Thus we must extend the original work to semi-simple gauge groups. A minimal requirement is that the scalar content of the theory must yield the Higgs doublet after symmetry breaking. We don't require that the scalars be entirely responsible for gauge symmetry breaking, other than electroweak symmetry breaking, since we leave open the possibility that strong interactions could dynamically break some symmetries.

After the work [14] there were attempts to find other realistic CAFEs, not necessarily grand unified. From our point of view these attempts were not completely successful since UV stability was dropped (see review [15] and references therein and in particular [89]). The fixed point was allowed to be UV repulsive in some directions in coupling space. In this case the space of couplings that do flow to the fixed point has reduced dimensionality. This amounts to constraints (sometimes called predictions) on the low energy couplings that are also affected by higher order corrections. Satisfying the constraints would require fine tuning the couplings order by order in perturbation theory. In our work we shall insist on complete UV stability.

Much more recently there has been another attempt to find UV complete theories with elementary scalars, but this time the search was for nontrivial UVFPs [25]. Unlike the case of asymptotic freedom, here the fixed point requires knowledge of the β-functions beyond lowest order. Interesting examples were found but here again complete UV stability was not attained. Also, in this context the work in [90] suggests that the transition from a regime of running couplings to a nontrivial UVFP is sufficient to cause a contribution to the Higgs mass. So in this case as well, the corresponding mass scale must be as low as possible.

The prototype of low scale unification is the Pati-Salam model [21], based on the gauge group $SU(4) \times SU(2)_L \times SU(2)_R$, with the fermions of one family in the $(4, 2, 1)_L + (4, 1, 2)_R$ representation. Our study will answer the question as to whether scalars can be added such that a SAFE results. But we shall set up our study in a more general context where we consider products of various $SU(N)$ gauge groups with various scalars that may transform simultaneously under two or three of these gauge groups. We only consider scalars in the fundamental representation since then we can expect a Higgs doublet to emerge after symmetry breaking. These results may be of more general interest for model building.

Since we are discussing theories that are UV complete above the Planck scale, one might wonder about the effect of gravity on the running couplings of the matter fields. This was discussed in the quadratic higher derivative gravity theories of [33, 86]. The coupling f_2^2, appearing as $1/f_2^2$ times the Weyl term, is always asymptotically free with both gravity and matter fields contributing with the same sign to the β-function. This means that f_2^2 is typically much smaller than the gauge couplings in the deep UV, and so its effect can be neglected. The coupling f_0^2 appearing in the R^2 term will be asymptoticallly free only if the ratio f_0^2/f_2^2 becomes negative in the UV. Depending on the matter content it is possible that f_0^2 could run relatively slowly and thus play a more significant role. Here we note a discrepancy in the calculated f_0^2 contribution to the scalar quartic β-functions in [33] and [86]. In the following we shall ignore the possible effect of gravity on the matter β-functions.

This chapter is organized as follows. In Sec. 4.2 we first review the basic idea to realize SAFEs with a simple Lie group. Then we generalize the study to a semi-simple gauge group in Sec. 4.3, as motivated by low scale unification. For quantitative study we choose several benchmarks for gauge groups and scalar representations. In Sec. 4.4 we present and discuss the numerical results. Based on these studies we consider the simplest example of a SAFE with low scale unification in Sec. 4.5. We conclude in Sec. 7.4.

4.2 SAFEs with Simple Lie Group

In this section we review the basic idea to realize SAFEs in [14]. This reference systematically studied the simple group $SU(N)$ or $O(N)$ case with fermions and scalars in various representations. Here we supplement their work with some numerical results for comparison with our later analysis.

Since we study UV asymptotic freedom, the one loop β-functions are sufficient to study the UV behavior. At one loop the coupled β-functions of gauge, Yukawa and quartic couplings can be solved sequentially. For the gauge coupling, its β-function only depends on itself and yields

$$\beta = \frac{dg}{dt} = \frac{bg^3}{(4\pi)^2} \Rightarrow g^2(t) = -\frac{8\pi^2}{bt} \tag{4.1}$$

with $t = \ln(\mu/\Lambda)$. $b < 0$ gives asymptotic freedom with an infrared Landau pole at $t = 0$ $(\mu = \Lambda)$. The β-function coefficient b gives the running speed of gauge coupling at large

t. For the Yukawa coupling y, its β-function has the generic form

$$(4\pi)^2\beta_y = a_y y^3 - a_g g^2 y, \tag{4.2}$$

where $a_y, a_g > 0$. The dependence on g can be eliminated with a change of variables $\bar{y} \equiv y^2/g^2$, and this gives

$$(4\pi)^2 g^{-2}\beta_{\bar{y}} = 2\bar{y}\left[a_y\bar{y} - (a_g + b)\right], \tag{4.3}$$

where dependence on b has appeared. To have asymptotically free y amounts to finding a UVFP for $\bar{y}$. When $a_g + b \leq 0$ and since $\bar{y} \geq 0$ by definition the only UVFP is $\bar{y} = 0$, which is UV repulsive. A stable UVFP requires that $a_g + b > 0$ in which case $\bar{y} = 0$ is the stable UVFP. The result is that $\bar{y}$ decreases asymptotically as

$$\bar{y}(t) \propto t^{\frac{a_g+b}{b}}. \tag{4.4}$$

As clarified in [14], the same conclusion applies to the more complicated case when the Yukawa couplings are described by a matrix. So in SAFEs, the contribution of Yukawa couplings is negligible in the β-functions of quartic couplings in the deep UV.

We may illustrate the general features with one scalar Φ_i in the fundamental representation of a $SU(N)$ gauge group. The gauge invariant scalar potential at dim $= 4$ has only one term,

$$V_4 = \lambda\, \Phi_i^* \Phi_i \Phi_j^* \Phi_j. \tag{4.5}$$

The one loop β-function for λ is

$$(4\pi)^2\beta_\lambda = 4\,(N+4)\,\lambda^2 - 6\lambda g^2\left(N - \frac{1}{N}\right) + \frac{3(N-1)(N^2+2N-2)}{4N^2}g^4. \tag{4.6}$$

This β-function is composed of three pieces: the positive pure quartic terms, negative gauge-quartic terms and positive pure gauge terms. To have $\beta_\lambda = 0$ the three contributions should be comparable and so this disfavors a large hierarchy between quartic and gauge couplings. In particular quartic couplings must also run as $1/t$ in the deep UV.

We may again eliminate the dependence on g by a change of variables $\bar{\lambda} \equiv \lambda/g^2$, which gives

$$(4\pi)^2 g^{-2}\beta_{\bar{\lambda}} = 4\,(N+4)\,\bar{\lambda}^2 - \bar{\lambda}\left[2b + 6\left(N - \frac{1}{N}\right)\right] + \frac{3(N-1)(N^2+2N-2)}{4N^2} \tag{4.7}$$

with b again appearing in the linear term. Defining $r \equiv b/b_M$ where $b_M = -11N/3$ is the pure gauge boson contribution, the regions with $2b+6(N-\frac{1}{N}) > 0$ and $2b+6(N-\frac{1}{N}) < 0$ meet at the value $r_0 = \frac{9}{11}(1-1/N^2)$. These two regions correspond to the slow gauge running ($r_s < r_0$) and fast gauge running ($r_f > r_0$) cases respectively, and there is a one-to-one mapping with $2r_s b_M + 6(N-\frac{1}{N}) = -(2r_f b_M + 6(N-\frac{1}{N}))$ and $\lambda \to -\lambda$.

$\beta_{\bar{\lambda}} = 0$ is simply a quadratic equation for $\bar{\lambda}$ and there are two real roots when

$$\left[2b + 6\left(N - \frac{1}{N}\right)\right]^2 - \frac{12}{N^2}(N+4)(N-1)(N^2+2N-2) > 0. \tag{4.8}$$

This inequality sets an upper (lower) bound on r in the slow (fast) running region with solutions $\bar{\lambda} > 0$ ($\bar{\lambda} < 0$). For the present example the lower bound on r in the branch $r > r_0$ is always above one and so this cannot be realized with any matter assignment. Also this region is disfavored due to the upper bound on r from the UV stability of Yukawa coupling and the vacuum stability condition for the quartic coupling $\bar{\lambda} > 0$. So we need only consider the slow running region, where the inequality (4.8) sets $N \geq 3$.

N	2	3	4	5	6	7	8	$N \gg 1$
Max r	0	0.02	0.09	0.13	0.17	0.19	0.21	0.35
Min n_F	0	16	20	24	28	31	35	3.6 N

Figure 4.1: The maximum $r = b/b_M$ for one fundamental scalar of $SU(N)$ and the minimum number n_F of Dirac fundamental fermions to achieve this.

For each $N \geq 3$, we present the upper bound on $0 \leq r \leq 1$ for various N in Fig. 4.1. We can determine the number of Dirac fermions n_F to satisfy this bound from

$$b = b_M + n_F b_F + \frac{1}{6}. \tag{4.9}$$

The minimum n_F basically grows with N, and it is shown for the fundamental representation $b_F = 2/3$ in the last row in Fig. 4.1.

For each N, b that satisfy (4.8) and $r < r_0$ there are two positive real roots $\bar{\lambda}_1 < \bar{\lambda}_2$. Given the positive contribution from the pure quartic and pure gauge terms, it is the smaller root $\bar{\lambda}_1$ that is stable, i.e. $d\beta/d\bar{\lambda} < 0$ at $\bar{\lambda} = \bar{\lambda}_1$. For each N we depict $\bar{\lambda}_1, \bar{\lambda}_2$ for all possible b in Fig. 4.2, where red and blue label stable and unstable UVFPs respectively. $b \to 0$ at the ends of each line. In large $N \gg 1$ limit, the stable and unstable UVFPs become insensitive to N and these end values approach 0.14 and 1.3 respectively. For a stable UVFP, $\bar{\lambda}$ is always smaller than one. Also, the stable UVFP $\bar{\lambda}_1$ is UV attractive

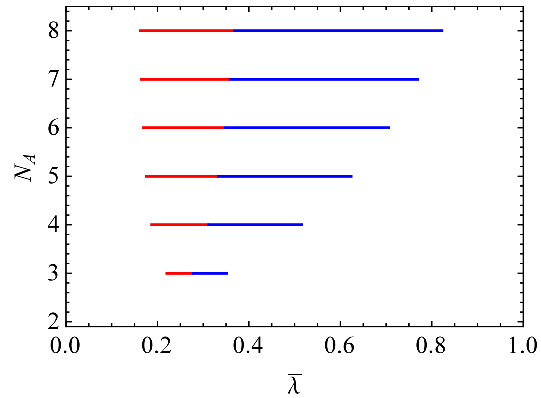

Figure 4.2: The values of $\bar{\lambda} = \lambda/g^2$ at stable (red) and unstable (blue) UVFPs as r varies over the allowed range.

with respect to all quartic couplings $\bar{\lambda} < \bar{\lambda}_2$.

By increasing the size and/or number of scalar representations, a larger N may be required to achieve a SAFE. This generally does not allow sufficient scalar fields to break the simple gauge group in some realistic manner [14]. For example $SU(5)$ grand unification typically requires two scalars, in the adjoint and fundamental representations, to break $SU(5)$ down to the SM. But with this set of scalars the theory is a SAFE only if $N \geq 7$.

For a given gauge group, the larger the total number of scalar degrees of freedom, the tighter is the constraint on b [14]. This general feature will carry over to our generalizations and it is another motivation to restrict ourselves to scalars in the fundamental representation.

4.3 Generalization to Semi-simple Lie Group

Motivated by low scale unification we shall focus on scalar fields transforming under the following two types of gauge groups with $N_i \geq 2$.

$$(1): \; SU(N_A) \times SU(N_B), \quad (2): \; SU(N_A) \times SU(N_B) \times SU(N_C) \tag{4.10}$$

We first discuss the behavior of Yukawa couplings for the semi-simple case. In the simplest case of a single Yukawa coupling y, as a generalization of the β-function in (4.3) we find

$$(4\pi)^2 g_j^{-2} \beta_{\bar{y}} = 2\bar{y} \left[a_y \bar{y} - \sum_{i \neq j} a_i g_i^2/g_j^2 - (a_j + b_j) \right], \tag{4.11}$$

where $\bar{y} = y^2/g_j^2$ and with g_j one of the gauge couplings. The a_i depend on the scalar and fermion representations. In the deep UV the gauge coupling g_i approaches its asymptotic form and becomes insensitive to its initial value. So we may replace the ratio of gauge couplings in (4.11) by their β-functions coefficients, i.e. $g_i^2/g_j^2 \to b_j/b_i$. If

$$1 + \sum_i \frac{a_i}{b_i} < 0 \tag{4.12}$$

then there is a stable UVFP and it is at $\bar{y} = 0$.

We have checked various fermion and scalar representations for the gauge groups in (4.10). It turns out that (4.12) is easy to satisfy since $a_i \sim N_i$ and b_i is negative. In some cases (4.12) may put a upper bound on b_i, but as we shall see below, in the parameter space of interest the constraint is much weaker than constraints from the quartic couplings. For a matrix of Yukawa couplings we expect these features will continue to hold, as in [14]. Therefore in our study of SAFEs for semi-simple gauge group we will focus on the quartic couplings and neglect the contribution of Yukawa couplings in their β-functions.

We now build four benchmarks for semi-simple Lie groups in (4.10).

Case A: $SU(N_A) \times SU(N_B)$ with (N_A, N_B)

For the gauge group $SU(N_A) \times SU(N_B)$ the simplest nontrivial setup is to have one scalar field Φ_{ik} that transforms in the fundamental representation of both groups, i.e. (N_A, N_B). The most general dim $= 4$ scalar potential is

$$V_4 = \lambda_d \Phi^*_{ik}\Phi_{ik}\Phi^*_{jl}\Phi_{jl} + \lambda_s \Phi^*_{ik}\Phi_{il}\Phi^*_{jl}\Phi_{jk} \tag{4.13}$$

when at least one $N_i > 2$. λ_d and λ_s denote double trace and single trace couplings respectively. In the deep UV, the β-functions for these quartic couplings are

$$\begin{aligned}
(4\pi)^2\beta_{\lambda_d} &= 4\left[(N_A N_B + 4)\,\lambda_d^2 + 2\,(N_A + N_B)\,\lambda_d\lambda_s + 3\lambda_s^2\right] - 6\lambda_d\left[\left(N_A - \frac{1}{N_A}\right)g_A^2\right.\\
&\quad \left.+\left(N_B - \frac{1}{N_B}\right)g_B^2\right] + \frac{3}{4}\left[\left(1+\frac{2}{N_A^2}\right)g_A^4 + \left(1+\frac{2}{N_B^2}\right)g_B^4\right] + 3g_A^2 g_B^2\left(1+\frac{1}{N_A N_B}\right)\\
(4\pi)^2\beta_{\lambda_s} &= 4\lambda_s\left[(N_A+N_B)\lambda_s + 6\lambda_d\right] - 6\lambda_s\left[\left(N_A - \frac{1}{N_A}\right)g_A^2 + \left(N_B - \frac{1}{N_B}\right)g_B^2\right]\\
&\quad + \frac{3}{4}\left[\left(N_A - \frac{4}{N_A}\right)g_A^4 + \left(N_B - \frac{4}{N_B}\right)g_B^4\right] - 3g_A^2 g_B^2\left(\frac{1}{N_A}+\frac{1}{N_B}\right)
\end{aligned} \tag{4.14}$$

It is straightforward to verify that (4.14) reduces to (4.6) in the single gauge group case with $N_B \to 1, g_B \to 0$ and $\lambda_d + \lambda_s \to \lambda$. The $N_A = N_B = 2$ case corresponds to the bidoublet in the left-right symmetric model and it has a larger set of couplings [91].

Case B: $SU(N_A) \times SU(N_B)$ with (N_A, N_B) and $(N_A, 1)$

In the second benchmark we consider the same gauge group with two scalars. We don't expect to learn much by considering two copies of (N_A, N_B), especially since the replication of scalars was considered in [14]. For the combination $(N_A, 1) + (1, N_B)$ there is a limit where the two scalars decouple and so this case is also of not much interest. So we will study two different scalars that share a common gauge group.

$$\Phi^{(1)}_{ik} : (N_A,\, N_B), \quad \Phi^{(2)}_{j} : (N_A,\, 1) \tag{4.15}$$

N_A specifies the common gauge group. The most general scalar potential when at least one $N_i > 2$ has five terms,

$$\begin{aligned} V_4 = {} & \lambda_{d1}\Phi^{(1)*}_{ik}\Phi^{(1)}_{ik}\Phi^{(1)*}_{jl}\Phi^{(1)}_{jl} + \lambda_{s1}\Phi^{(1)*}_{ik}\Phi^{(1)}_{il}\Phi^{(1)*}_{jl}\Phi^{(1)}_{jk} + \lambda_2\Phi^{(2)*}_{i}\Phi^{(2)}_{i}\Phi^{(2)*}_{j}\Phi^{(2)}_{j} \\ & + 2\lambda_{d12}\Phi^{(1)*}_{ik}\Phi^{(1)}_{ik}\Phi^{(2)*}_{j}\Phi^{(2)}_{j} + 2\lambda_{s12}\Phi^{(1)*}_{ik}\Phi^{(1)}_{jk}\Phi^{(2)*}_{j}\Phi^{(2)}_{i}. \end{aligned} \tag{4.16}$$

Here there are two mixing couplings $\lambda_{d12}, \lambda_{s12}$. The one loop β-functions are presented in (4.31) in Appendix A. Due to the presence of the common gauge group we shall find that there is no UVFP solution where the mixing couplings vanish and the two scalars decouple.

Case C: $SU(N_A)\times SU(N_B)\times SU(N_C)$ with $(N_A, N_B, 1)$ and $(N_A, 1, N_C)$

With the enlarged gauge symmetry $SU(N_A) \times SU(N_B) \times SU(N_C)$, the next interesting scalar content starts with two scalars. It is again interesting to study the case with two different scalars sharing a common gauge group. The case different from Case B is the following.

$$\Phi^{(1)}_{ik} : (N_A,\, N_B,\, 1), \quad \Phi^{(2)}_{ja} : (N_A,\, 1,\, N_C) \tag{4.17}$$

We set $N_A > 2$ for the common gauge group. In the context of the Pati-Salam model, this setup may correspond to left-right symmetric scalars $(4, 2, 1)$ and $(4, 1, 2)$. The scalar potential is

$$V_4 = \lambda_{d1}\Phi^{(1)*}_{ik}\Phi^{(1)}_{ik}\Phi^{(1)*}_{jl}\Phi^{(1)}_{jl} + \lambda_{s1}\Phi^{(1)*}_{ik}\Phi^{(1)}_{il}\Phi^{(1)*}_{jl}\Phi^{(1)}_{jk} + \lambda_{d2}\Phi^{(2)*}_{ia}\Phi^{(2)}_{ia}\Phi^{(2)*}_{jb}\Phi^{(2)}_{jb} + \lambda_{s2}\Phi^{(2)*}_{ia}\Phi^{(2)}_{ib}\Phi^{(2)*}_{jb}\Phi^{(2)}_{ja}$$

$$+ 2\lambda_{d12}\Phi^{(1)*}_{ik}\Phi^{(1)}_{ik}\Phi^{(2)*}_{ja}\Phi^{(2)}_{ja} + 2\lambda_{s12}\Phi^{(1)*}_{ik}\Phi^{(1)}_{jk}\Phi^{(2)*}_{ja}\Phi^{(2)}_{ia}, \tag{4.18}$$

where $\lambda_{d12}, \lambda_{s12}$ are mixing couplings. We may consider a simplified version of this theory by imposing a Z_2 symmetry, the analogy of left-right symmetry in the Pati-Salam model.

$$\text{Case C1}\,(Z_2 \text{ symmetry}): \;\; N_B = N_C,\; g_B = g_C,\; \lambda_{d2} = \lambda_{d1},\; \lambda_{s2} = \lambda_{s1} \tag{4.19}$$

This Case C1 amounts to picking a special slice in the whole parameter space, with only two gauge couplings and four quartic couplings. The β-functions are presented in (4.32).

We denote by case C2 the general case with six quartic couplings. The β-functions are in (4.33).

In the case of the Pati-Salam model with $\Phi_L = (4,2,1)$ and $\Phi_R = (4,1,2)$ we may construct a gauge invariant quartic term with the Levi-Civita symbol,

$$V_4 \supset \frac{1}{2}\lambda_\epsilon \epsilon_{iji'j'}\epsilon_{kl}\epsilon_{k'l'}\left[\Phi^{(1)}_{ik}\Phi^{(1)}_{jl}\Phi^{(2)}_{i'k'}\Phi^{(2)}_{j'l'} + h.c.\right]. \tag{4.20}$$

This amounts to Det(Φ) for 4×4 matrix $\Phi \equiv (\,\Phi_L\ \Phi_R\,)$, which vanishes for $\Phi_L = \Phi_R$. The modified β-functions with the λ_ϵ contribution are presented in (4.34), (4.35).

Case D: $SU(N_A) \times SU(N_B) \times SU(N_C)$ with (N_A, N_B, N_C)

In the last benchmark we study a scalar representation charged under all three groups. In particular we consider the fundamental representation $\Phi_{ika} : (N_A, N_B, N_C)$. This type of scalar field is less studied in literature since its VEV breaks all gauge symmetries at the same scale. But in view of finding SAFEs it is intriguing to ask whether it helps to have a scalar transforming under more gauge groups. The scalar potential is

$$\begin{aligned} V_4 = {} & \lambda_d \Phi^*_{ika}\Phi_{ika}\Phi^*_{jlb}\Phi_{jlb} + \lambda_{s1}\Phi^*_{ika}\Phi_{jka}\Phi^*_{jlb}\Phi_{ilb} \\ & + \lambda_{s2}\Phi^*_{ika}\Phi_{ila}\Phi^*_{jlb}\Phi_{jkb} + \lambda_{s3}\Phi^*_{ika}\Phi_{ikb}\Phi^*_{jlb}\Phi_{jla}. \end{aligned} \tag{4.21}$$

There are now three single trace couplings. The one loop β-functions are presented in (4.36), and they are symmetric under interchanges between (N_A, λ_{s1}), (N_B, λ_{s2}) and (N_C, λ_{s3}). One can verify that (4.36) reduces to (4.14) with $N_C \to 1$, $g_C \to 0$ and $\lambda_d + \lambda_{s3} \to \lambda_d$, $\lambda_{s1} + \lambda_{s2} \to \lambda_s$.

In the Pati-Salam model with one $(4,2,2)$ scalar we may construct another Levi-Civita term,

$$V_4 \supset \frac{1}{6}\lambda_\epsilon \epsilon_{iji'j'}\epsilon_{kl}\epsilon_{mn}\epsilon_{ac}\epsilon_{bd}\left[\Phi_{ika}\Phi_{jlb}\Phi_{i'mc}\Phi_{j'nd} + h.c.\right]. \tag{4.22}$$

The β-functions involving λ_ϵ are presented in (4.37) and (4.38).

4.4 Numerical results and analysis

In this section we present the numerical results and analysis of the four benchmarks. As before we change variables $\bar{\lambda}_i = \lambda_i/g_j^2$ where g_j is one of the gauge couplings. Then we replace the ratios of different gauge couplings by their asymptotic values, $g_i^2/g_j^2 \to b_j/b_i$. This leaves us with coupled quadratic equations of the $\bar{\lambda}_i$. Taking case A as an example, the β-functions in (4.14) become

$$\begin{aligned}(4\pi)^2 g_A^{-2}\beta_{\bar{\lambda}_d} =& \, 4\left[(N_A N_B+4)\,\bar{\lambda}_d^2 + 2\,(N_A+N_B)\,\bar{\lambda}_d\bar{\lambda}_s + 3\bar{\lambda}_s^2\right] - \bar{\lambda}_d b_A\left[2+\frac{6}{b_A}\left(N_A-\frac{1}{N_A}\right)\right.\\ &\left.+\frac{6}{b_B}\left(N_B-\frac{1}{N_B}\right)\right] + \frac{3}{4}b_A^2\left[\frac{1}{b_A^2}\left(1+\frac{2}{N_A^2}\right)+\frac{1}{b_B^2}\left(1+\frac{2}{N_B^2}\right)+\frac{4}{b_A b_B}\left(1+\frac{1}{N_A N_B}\right)\right]\\ (4\pi)^2 g_A^{-2}\beta_{\bar{\lambda}_s} =& \, 4\bar{\lambda}_s\left[(N_A+N_B)\bar{\lambda}_s + 6\bar{\lambda}_d\right] - \bar{\lambda}_s b_A\left[2+\frac{6}{b_A}\left(N_A-\frac{1}{N_A}\right)+\frac{6}{b_B}\left(N_B-\frac{1}{N_B}\right)\right]\\ &+\frac{3}{4}b_A^2\left[\frac{1}{b_A^2}\left(N_A-\frac{4}{N_A}\right)+\frac{1}{b_B^2}\left(N_B-\frac{4}{N_B}\right)-\frac{4}{b_A b_B}\left(\frac{1}{N_A}+\frac{1}{N_B}\right)\right],\end{aligned} \tag{4.23}$$

where $\bar{\lambda}_i = \lambda_i/g_A^2$.

With these we can solve for the UVFP of $\{\bar{\lambda}_i\}$ as functions of N_i and b_i. Since the coupled quadratic equations are usually difficult to solve analytically, we find numerical solutions for a parameter scan over N_i, b_i. To illustrate the pattern, we choose $2 \le N_i \le 8$. The β-function coefficients b_i depend on the matter and are model dependent. For convenience we use $r_i \equiv b_i/b_{i,M}$, where $b_{i,M} = -11N_i/3$, and we consider the range $0 < r_i \le 1$. The $\{\bar{\lambda}_{0,i}\}$ at UVFPs should be real but need not be positive.

To find UV stability we study the RG flows in vicinity of the UVFP. At linear order it is characterized by the matrix

$$D_{ij}(\bar{\lambda}_{0,i}) \equiv \left.\frac{\partial\beta_{\bar{\lambda}_i}}{\partial\bar{\lambda}_j}\right|_{\bar{\lambda}_i=\bar{\lambda}_{0,i}}. \tag{4.24}$$

The UVFP is absolutely stable as long as all eigenvalues κ_k of $D_{ij}(\bar{\lambda}_{0,i})$ are negative. The UVFP for the $\bar{\lambda}_i$'s is approached along the directions of the eigenvectors as $t^{-\kappa_k/2b_A}$.

4.4.1 Constraints on $r_i \equiv b_i/b_{i,M}$ from the parameter scan

We find that the distribution of solutions as a function of the r_i's share similar features for all our benchmarks. For each N_i set we scan over r_i space with the step $\delta r_i = 0.01$ for

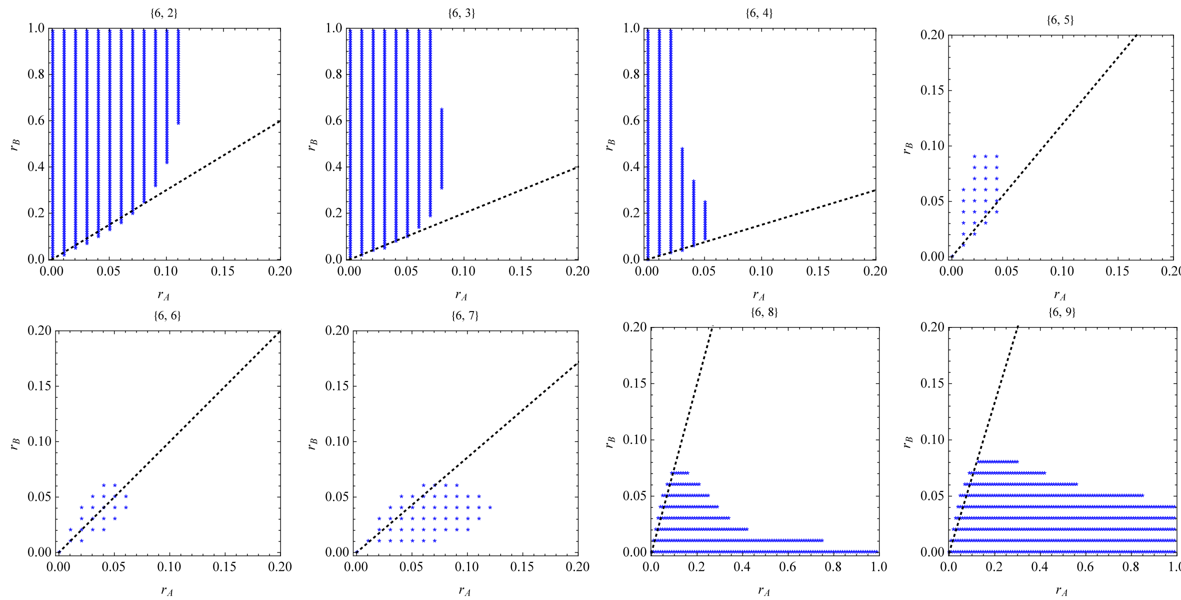

Figure 4.3: The projection of the parameter scan on the r_A-r_B plane in Case A for different $\{N_A, N_B\}$. The step size of the parameter scan is $\delta r_i = 0.01$.

$0 < r_i \leq 1$. This step is comparable to the minimum matter contribution for $N_i \lesssim 10$. The projections on the r_A-r_B plane for Case A with $N_A = 6$ and $2 \leq N_B \leq 9$ are presented in Fig. 4.3. In each panel the black dot line denotes $b_A = b_B$. This figure highlights the fact that it is a large hierarchy between N_A and N_B that helps most to achieve a SAFE. And when there is a hierarchy it is the r_i of the larger gauge group that is bounded from above.

We present the upper bounds on r_i for all our benchmark models in Fig. 4.4 and Fig. 4.5. This information can be used to constrain the matter content to achieve SAFEs. To illustrate the number fraction of viable points for each N_i set, we use dark (light) blue for more (less) viable points. Fig. 4.4(a) for Case A is symmetric under $N_A \leftrightarrow N_B$ and the general features mentioned above are quite clear. Well off the diagonal only the r_i of the large gauge group is constrained and this constraint becomes more relaxed for increasing hierarchy between N_A and N_B. For the near-diagonal elements there are upper bounds on both r_B (upper) and r_A (lower) for the two gauge β-functions. The $N_A = N_B = 2$ case has a larger set of quartic couplings and we have checked that it does not yield a SAFE.

We may briefly consider the fate of the fast running solutions, as we did for the simple gauge group. The vanishing of the linear terms in (4.23) defines a boundary on

(a) Case A

N	2	3	4	5	6	7	8
2	0	0	0.03	0.08	0.11	0.14	0.15
3	0	0	0	0.04	0.08	0.10	0.13
4	0.03	0	0	0.02 0.06	0.05	0.08	0.10
5	0.08	0.04	0.06 0.02	0.03 0.03	0.04 0.09	0.06	0.08
6	0.11	0.08	0.05	0.09 0.04	0.06 0.06	0.06 0.12	0.07
7	0.14	0.10	0.08	0.06	0.12 0.06	0.08 0.08	0.07 0.13
8	0.15	0.13	0.10	0.08	0.07	0.13 0.07	0.09 0.09

(b) Case B

N	2	3	4	5	6	7	8
2	0	0	0	0	0	0	0
3	0	0	0	0	0*	0*	0*
4	0	0	0	0	0.01 0.08	0.01 0.08	0.01 0.08
5	0.02	0	0	0	0.01 0.06	0.02 0.13	0.02 0.13
6	0.07	0.03	0.03 0.01	0.01 0.01	0.02 0.03	0.03 0.09	0.03 0.16
7	0.10	0.06	0.04	0.07 0.03	0.04 0.03	0.03 0.05	0.04 0.10
8	0.12	0.09	0.06	0.05	0.08 0.04	0.05 0.04	0.05 0.07

(c) Case C1

N	2	3	4	5	6	7	8
2	0	0	0.03	0.08	0.11	0.13	0.14
3	0	0	0	0.04	0.07	0.10	0.12
4	0	0	0	0	0.04	0.07	0.09
5	0	0	0	0	0	0.04	0.06
6	0.03	0	0	0	0	0	0.04
7	0.06	0	0	0	0	0	0
8	0.09	0.03	0	0	0	0	0

(d) Case D

N	(2,2)	(3,2)	(i,j)
2	0	0	0
3	0	0	0
4	0	0	0
5	0	0	0
6	0.03	0	0
7	0.06	0	0
8	0.08	0.02	0

Figure 4.4: The upper bounds of r_i where 0 means no solutions. For the first three cases they are functions of N_A (row) and N_B (column); the last one is a function of N_A (row) and (N_B, N_C) (column). A single number gives the upper bound on the r_i with the largest N_i. Two numbers provide limits on r_B (upper) and r_A (lower). 0^* denotes marginal cases where the existence of solutions goes beyond our parameter scan accuracy.

the $r_A - r_B$ plane as follows,

$$2 + \frac{6}{r_A b_{A,M}}\left(N_A - \frac{1}{N_A}\right) + \frac{6}{r_B b_{B,M}}\left(N_B - \frac{1}{N_B}\right) = 0\,. \tag{4.25}$$

The region below (above) the boundary features slow (fast) running, and the UVFP solutions in the two regions are related by a rescaling of the r_i and $\lambda_i \to -\lambda_i$. In this Case A we find that the boundary (4.25) and thus all fast running UVFP solutions are outside of the physical region $0 < r_i \le 1$.

For Case B in Fig. 4.4(b), since the two scalars are charged differently under $SU(N_A)\times SU(N_B)$, the pattern becomes asymmetric. The rows and columns denote the common

(a) $N_A=2$

N	2	3	4	5	6	7	8
2	0	0	0	0	0	0	0
3	0	0	0	0	0	0	0
4	0	0	$1^{.03}_{.03}$	$1^{.08}_{.03}$	$1^{.11}_{.03}$	$1^{.13}_{.03}$	$1^{.15}_{.03}$
5	0	0	$1^{.03}_{.08}$	$1^{.08}_{.08}$	$1^{.11}_{.08}$	$1^{.13}_{.08}$	$1^{.15}_{.08}$
6	0	0	$1^{.03}_{.11}$	$1^{.08}_{.11}$	$1^{.11}_{.11}$	$1^{.13}_{.11}$	$1^{.15}_{.11}$
7	0	0	$1^{.03}_{.13}$	$1^{.08}_{.13}$	$1^{.11}_{.13}$	$1^{.13}_{.13}$	$1^{.15}_{.13}$
8	0	0	$1^{.03}_{.15}$	$1^{.08}_{.15}$	$1^{.11}_{.15}$	$1^{.13}_{.15}$	$1^{.15}_{.15}$

(b) $N_A=4$

N	2	3	4	5	6	7	8
2	0	0	0	0	0^*	0^*	0^*
3	0	0	0	0	0	0	0
4	0	0	0	0	0	0	0
5	0	0	0	0	0	0	0
6	0^*	0	0	0	$1^{.05}_{.05}$	$1^{.08}_{.05}$	$1^{.10}_{.05}$
7	0^*	0	0	0	$1^{.05}_{.08}$	$1^{.08}_{.08}$	$1^{.10}_{.08}$
8	0^*	0	0	0	$1^{.05}_{.10}$	$1^{.08}_{.10}$	$1^{.10}_{.10}$

(c) $N_A=6$

N	2	3	4	5	6	7	8
2	$.03^{1}_{1}$	0	0	0	0	0	$.11^{.02}_{1}$
3	0	0	0	0	0	0	0^*
4	0	0	0	0	0	0	0^*
5	0	0	0	0	0	0	0^*
6	0	0	0	0	0	0	0^*
7	0	0	0	0	0	0	$.05^{.02}_{.02}$
8	$.11^{1}_{.02}$	0^*	0^*	0^*	0^*	$.05^{.02}_{.02}$	$1^{.07}_{.07}$

(d) $N_A=8$

N	2	3	4	5	6	7	8
2	$.09^{1}_{1}$	$.06^{1}_{1}$	$.03^{1}_{1}$	$.02^{.06}_{1}$	$.01^{.02}_{1}$	$.02^{.02}_{1}$	$.04^{.02}_{1}$
3	$.06^{1}_{1}$	$.03^{1}_{1}$	0	0	0	0	0
4	$.03^{1}_{1}$	0	0	0	0	0	0
5	$.02^{1}_{.06}$	0	0	0	0	0	0
6	$.01^{1}_{.02}$	0	0	0	0	0	0
7	$.02^{1}_{.02}$	0	0	0	0	0	0
8	$.04^{1}_{.02}$	0	0	0	0	0	0

Figure 4.5: In Case C2 the upper bounds on r_i for various N_A as functions of N_B (row) and N_C (column). The three constraints are presented with the notation $(r_A)^{r_C}_{r_B}$.

gauge group $SU(N_A)$ and $SU(N_B)$ respectively. When $N_A \geq N_B$ we see the similar pattern as Case A in the lower left part of the table but with a smaller viable parameter space. In the upper right corner, i.e. $N_B > N_A$, the common group is small and then for the $(N_A, 1)$ scalar it is difficult to obtain solutions.

In Fig. 4.4(c) we present the bounds for Case C1 with Z_2 symmetry, with row and column for $SU(N_A)$ and $SU(N_B)$ respectively. The $N_A > N_B$ region, the lower left corner, now has a more stringent constraint on r_A compared to Cases A and B. This is due to enhanced pure quartic terms in the β-functions of (4.32). For the $N_B > N_A$ region, the upper right corner, there are more solutions compared to Case B since the two copies of $SU(N_B)$ enhance the gauge-quartic terms. Here the constraint on r_B applies to both of the large $SU(N_B)$ gauge groups. For the special case $N_A = 4, N_B = N_C = 2$ where we see zero solutions, one more coupling λ_ϵ in (4.20) gets involved. Given that its β-function is proportional to λ_ϵ, its UVFP is at zero, and so whether or not it is stable it cannot alter the lack of a UVFP in the other couplings.

For Case D we only find a small number of (N_A, N_B, N_C) values with viable solutions, as shown in Fig. 4.4(d). Here we assume N_A (row) is the largest while (N_B, N_C) (column) has $N_B \geq N_C$. The paucity of solutions here is basically due to the appearance of a $4N_AN_BN_C\bar{\lambda}_d^2$ term in β_{λ_d}. Again the extra coupling λ_ϵ in (4.22) for the special case $N_A = 4, N_B = N_C = 2$ does not affect the lack of a UVFP.

Finally we turn to Case C2. It depends on all three N_A, N_B, N_C and the results cannot be summarized in one 2D plane. But we do find that the constraints when $N_B = N_C$ are quite similar to Case C1 in Fig. 4.4(c). The general upper bounds on r_A, r_B, r_C for various N_A are displayed in Fig. 4.5 as functions of N_B (row) and N_C (column). We present these limits using the notation $(r_A)_{r_B}^{r_C}$. From the four tables one can see that solutions tend to appear when some hierarchy develops between the three values N_A, N_B, N_C. Among the possibilities, a hierarchy with a large common gauge group is the most efficient. And it can be seen that the upper bound on r_i is typically relaxed or nonexistent $(= 1)$ in those cases where the associated N_i is small relative to some other N_j.

4.4.2 $\bar{\lambda}_j$ values from the parameter scan

Next we show results for the values of the quartic couplings at the UVFPs. We define $\bar{\lambda}_j \equiv \lambda_j/g_i^2$ where g_i is the coupling of the largest gauge group. We saw in previous section that this coupling runs most slowly in the UV (has the smallest b_i) and thus is the largest gauge coupling.

We start from the simplest Case A with only two quartic couplings. In Fig. 4.6, for some typical (N_A, N_B), the first row shows the projection of the parameter scan on the $\bar{\lambda}_d$-$\bar{\lambda}_s$ plane, while the second row shows the r_A-r_B projection for comparison. Among all UVFP of (4.23) we depict the stable and unstable solutions by red and blue dots respectively. The situation is clearest for the left plots where the ratio N_A/N_B is the greatest. For each (r_A, r_B), there are always a pair of solutions, one stable and one unstable with smaller and larger $\bar{\lambda}_d$ respectively. With decreasing r_A we go through different arcs from inside out, where the arc length depends on the number of viable r_B. In $r_A \to 0$ limit, the solutions become independent of r_B and reach the corners of the red and blue regions that possess the largest distance between stable and unstable UVFPs. When N_A, N_B are similar both gauge couplings play significant roles and the solution pattern becomes more involved.

The unstable solution in each case is actually a saddle point, with one direction UV attractive and the other one repulsive. Also, at least for $2 \leq N_i \leq 8$, we find that the quartic couplings at the UVFPs are positive and typically of order 0.1 or 0.2 times the

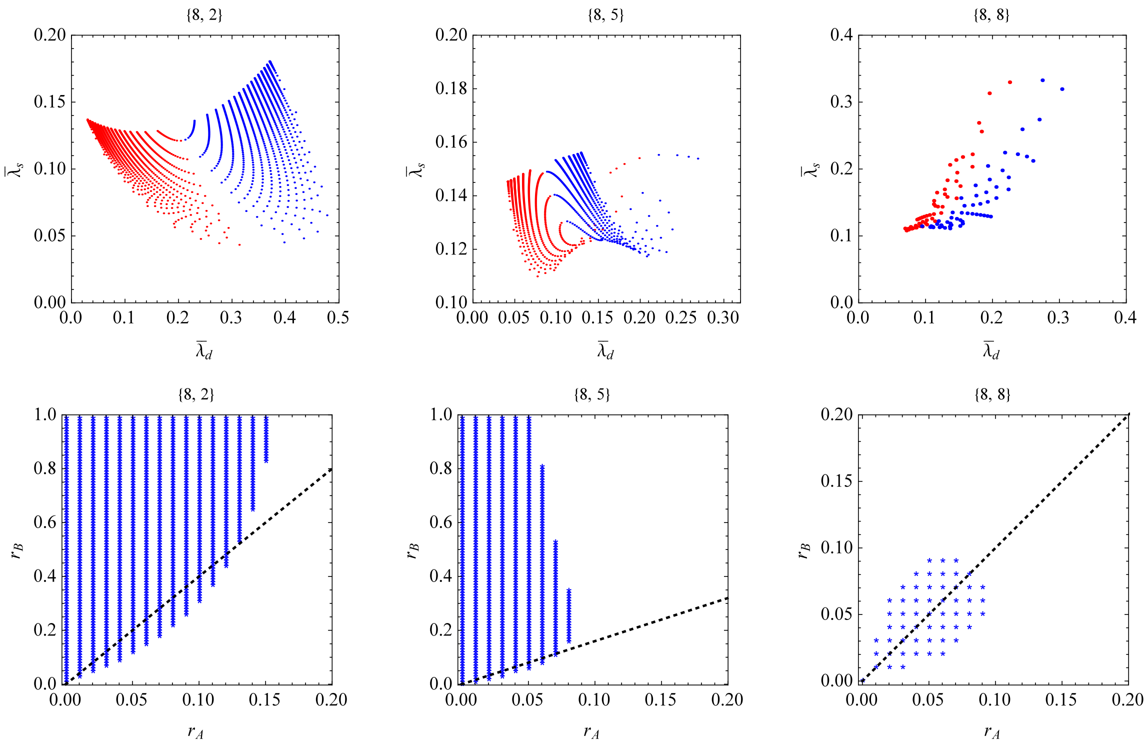

Figure 4.6: The projection of the parameter scan on the $\bar{\lambda}_d - \bar{\lambda}_s$ (first row) and r_A-r_B (second row) planes for different $\{N_A, N_B\}$. The quartic couplings are normalized by the largest gauge coupling. The red and blue dots represent stable and unstable UVFPs respectively. Note that some characteristics of these plots are determined by the step size of the parameter scan.

largest gauge coupling. The stability of tree level potential demands the conditions

$$\bar{\lambda}_d + \bar{\lambda}_s > 0, \quad 2\bar{\lambda}_d + \bar{\lambda}_s > 0\,, \tag{4.26}$$

but here they put no further constraint.

In comparison to these slow running UVFPs the unphysical fast running UVFPs again come in pairs, but one is a saddle point and the other is completely unstable. Another curiosity occurs when one of the N_i is very large, e.g. $N_A \geq 26$ and $N_B = 2$. Then four slow running UVFPs can occur, one stable, two saddle points, and one completely unstable. The two new UVFPs correspond to a large $\bar{\lambda}_s > 0$, with which the coefficient of linear $\bar{\lambda}_d$ term in $\beta_{\bar{\lambda}_d}$ becomes positive and the root of $\bar{\lambda}_d$ is negative. The fast running version of these UVFPs would be characterized by the same four types, which is more interesting here because one is stable. But at least for the cases we have considered the fast running solutions are outside the physical range of the r_i's, and they produce tension for Yukawa couplings and vacuum stability.

For Case B with five quartic couplings we project the higher dimensional space onto three 2D planes. In Fig. 4.7 we show the case $N_A = 8, N_B = 2$. Compared with the

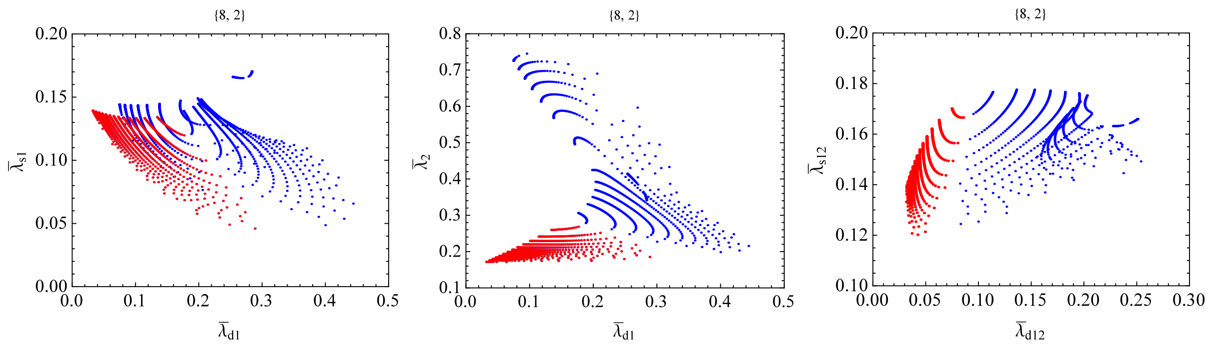

Figure 4.7: Projection of the parameter scan on some coupling planes for Case B with $N_A = 8, N_B = 2$.

counterpart in Case A we see a similar pattern of stable and unstable UVFP pairings on the $\bar{\lambda}_{d1}$-$\bar{\lambda}_{s1}$ plane. For some r_i there are four UVFPs and the additional pair of solutions are saddle points. They correspond to different $\bar{\lambda}_2$ as shown on $\bar{\lambda}_{d1}$-$\bar{\lambda}_2$ plane. The mixing couplings $\bar{\lambda}_{s12}$ and $\bar{\lambda}_{d12}$ are both positive and away from zero. They make considerable positive contribution to $\beta_{\lambda_{d1}}, \beta_{\lambda_{s1}}, \beta_{\lambda_2}$, causing the number of solutions to decrease.

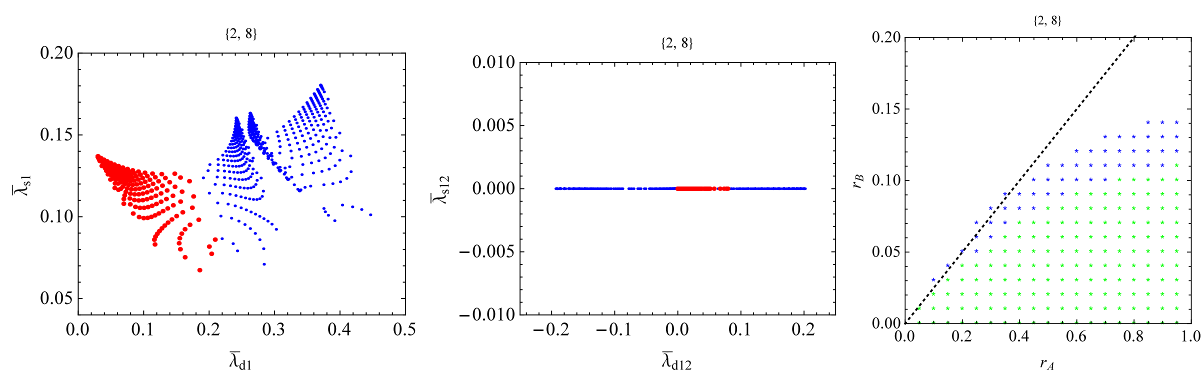

Figure 4.8: Projection of the parameter scan on some coupling planes for Case C1 with $N_A = 2, N_B = 8$. The right panel is a r_i projection, where blue and green denote the points with 2 and 4 UVFPs respectively.

For Case C1 the large common group case $N_A > N_B$ has quite similar features to Case A. Given the dominance of the common gauge group there are two UVFPs for each viable r_i and the one with the smaller $\bar{\lambda}_d$ is UV stable. In the small common gauge group case, $N_A < N_B$, some new types of solutions emerge. For illustration we present the UVFPs for $N_A = 2, N_B = 8$ in the left and middle panels of Fig. 4.8. For some r_i there are again an extra pair of UVFPs at saddle points. They possess a large $\bar{\lambda}_{d1}$ (left) and a negative $\bar{\lambda}_{d12}$ (middle). The corresponding r_i with four UVFPs are denoted by the green dots in the right panel.

With a large positive $\bar{\lambda}_{d1}$ we find that the mixing coupling $\bar{\lambda}_{d12}$ can be negative, but then the coefficient of $\bar{\lambda}_{d12}$ in $\beta_{\bar{\lambda}_{d12}}$ is positive and the solution becomes unstable.

Mixing couplings are usually positive for stable UVFPs, but a new feature we see here is that they can be close to zero. This is due to the suppressed pure gauge terms in the β-functions of the mixing couplings, which only receives a small contribution from the common gauge group (it is 0 for $N_A = 2$ case). Finally the general picture of UVFPs for Case C2 without the Z_2 symmetry is similar to Case C1.

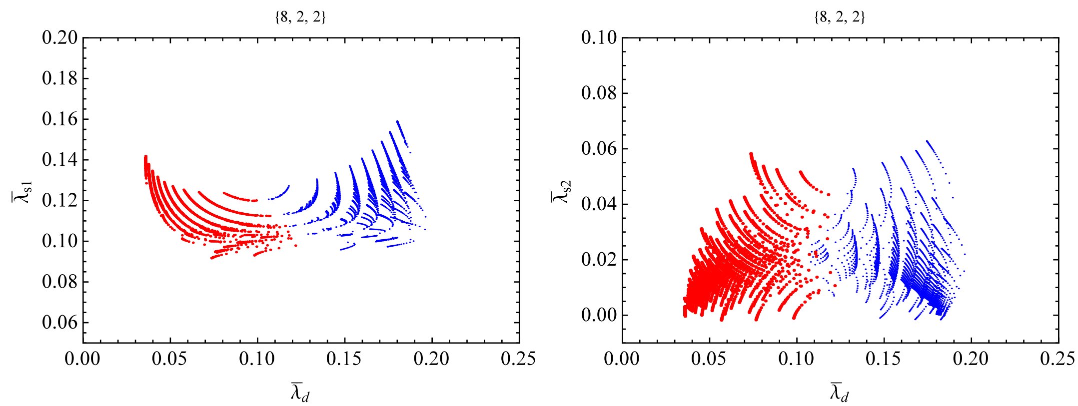

Figure 4.9: Projection of the parameter scan on some coupling planes for Case D with $N_A = 8, N_B = 2, N_C = 2$.

Case D has four quartic couplings, one double trace and three that are single trace. We depict the projections $\bar{\lambda}_{s1}$-$\bar{\lambda}_d$ and $\bar{\lambda}_{s2}$-$\bar{\lambda}_d$ in Fig. 4.9 for $N_A = 8$, $N_B = N_C = 2$. The typical feature is reflected on the range of single trace couplings at UVFPs. We find that the coupling with a single trace associated with the largest gauge group $\bar{\lambda}_{s1}$ has comparable size with other couplings at UVFPs, while those associated with small gauge groups, $\bar{\lambda}_{s2}$ or $\bar{\lambda}_{s3}$, could be close to zero or even slightly negative. Again this is determined by the dominant pure gauge terms in the β-functions.

4.5 The Simplest Model

As a general feature of the previous results, when a hierarchy in the sizes of the different gauge groups helps to achieve SAFEs, the gauge coupling associated with the largest group is constrained to run quite slowly. A small ratio $r_i = b_i/b_{i,M}$ requires a sufficient number of fermions. We first check whether some number of chiral fermions gauged under $SU(N_A) \times SU(N_B) \times SU(N_B)$ could work. We assume the fermion content

$$\Psi_L : (N_A, N_B, 1), \quad \Psi_R : (N_A, 1, N_B), \quad Q_L : (1, \bar{N}_B, N_B), \tag{4.27}$$

with n_F copies of $\Psi_L + \Psi_R$ and n_Q copies of chiral fermions Q_L. To be anomaly free when $N_B > 2$ we need an integer ratio $n_F/n_Q = N_B/N_A$. (For $N_B = 2$ we only need

$n_F N_A + n_Q N_B$ to be even [92].) The β-function coefficients of two gauge couplings are

$$b_A = -\frac{11}{3}N_A + n_F\frac{2N_B}{3} + b_{A,s}, \quad b_B = -\frac{11}{3}N_B + n_F\frac{2N_A}{3} + b_{B,s}, \tag{4.28}$$

if we use $n_Q = N_A n_F/N_B$. $b_{i,s}$ is the scalar contribution and for instance $b_{A,s} = N_B/3, b_{B,s} = N_B/6$ for Case C. Since the scalar contributions are small we need n_F sufficiently large to render b_i of the largest gauge group small for SAFEs as in Fig. 4.4. On the other hand, n_F is bounded from above by the requirement that all gauge couplings are asymptotically free, i.e. $b_A, b_B < 0$. It turns out that no n_F may satisfy both requirements. The alternative then is to introduce the appropriate number of fermions that only transform under the large gauge group.

Two low scale unification models with a long history in the literature are both based on a product of three gauge groups. One is the triunification model based on $SU(3) \times SU(3) \times SU(3)$ [93] and the other is the Pati-Salam model $SU(4) \times SU(2)_L \times SU(2)_R$ [21]. Our results show that the former cannot be SAFE and so we turn to the latter. In this case of all the SAFEs that we have found there is only one that is of relevance. From the results for Case A we find that we can add a single scalar Φ transforming as $(4, 2, 1)$. We choose $(4, 2, 1)$ rather than $(4, 1, 2)$ to ensure that Φ will yield the SM Higgs doublet.

As we have just discussed, the constraint on the $SU(4)$ β-function from Fig. 4.4, $|b_4| \lesssim 0.44$, requires additional fermions. Thus in addition to the n_F families of standard fermions $F_{L/R}$ we have a number n_f of Dirac fermions $f_{L/R}$ transforming only under $SU(4)$. These fermions are vector-like, they can have mass without breaking the gauge symmetries. These masses are additional parameters in the model. The particle content is then as shown in Table 4.1. Upon the breakdown $SU(4) \to SU(3)$ we see that the model predicts a coloured scalar doublet in addition to the Higgs doublet.

Table 4.1: Matter fields in the simplest model.

Fields	Number	$SU(4)$	$SU(2)_L$	$SU(2)_R$
F_L	n_F	4	2	1
F_R	n_F	4	1	2
$f_{L,R}$	n_f	4	1	1
Φ	1	4	2	1

The one loop β-functions are

$$b_4 = \frac{2}{3}(2n_F + n_f) + \frac{1}{3} - \frac{44}{3}, \quad b_L = \frac{4}{3}n_F + \frac{2}{3} - \frac{22}{3}, \quad b_R = \frac{4}{3}n_F - \frac{22}{3} \tag{4.29}$$

where n_F and n_f are defined in Table 4.1. As shown in Fig. 4.10(a) there are only two

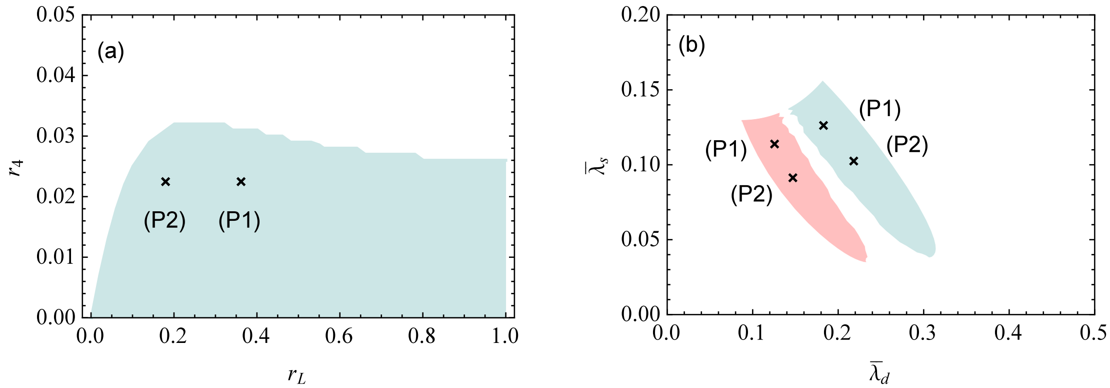

Figure 4.10: The two viable points in (4.30) showing (a) the β-function coefficients and (b) the coupling ratios at the UVFPs.

viable points with $n_F \geq 3$,

$$\text{P1}: \; n_F = 3, \, n_f = 15; \quad \text{P2}: \; n_F = 4, \, n_f = 13, \tag{4.30}$$

that give SAFEs. The corresponding fixed point values of the coupling ratios, for both the stable and unstable cases, are shown in Fig. 4.10(b).

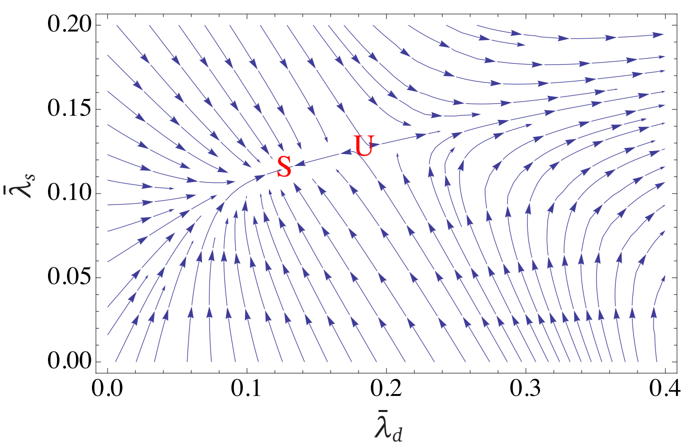

Figure 4.11: Quartic coupling flow towards the UV for the case P1, showing the stable and unstable fixed points. g_L/g_4 is set to its fixed point value.

Fig. (4.11) shows how the quartic couplings flow towards the UV for the case P1. The basin of attraction lies to the left of a line on which the unstable fixed point sits. Although the $SU(2)_L$ gauge coupling g_L is given by its fixed point value $g_L/g_4 = 1/8$ for this plot, the basin of attraction hardly changes as long as $g_L/g_4 \lesssim 1$ down to some IR scale of interest. For $g_L/g_4 \gtrsim 1$ the boundary starts to move significantly to the left, until at $g_L/g_4 \approx 2$ the quartic couplings can no longer both be positive at that IR scale. By also imposing the vacuum stability conditions in (4.26) on the basin of attraction, we find that the viable flows for the $\bar{\lambda}_i$ are restricted to a finite region that shrinks if g_L/g_4 grows larger.

$SU(4)$ must break at a high enough scale, at least higher than $\mathcal{O}(100)$ TeV, due to constraints for example from the rare decay $K \to e\mu$. (The constraints on $SU(2)_R$ breaking are not so strong.) On the other hand the $(4, 2, 1)$ scalar Φ is not available to break $SU(4)$ since the VEV $\langle\Phi\rangle$ would also break $SU(2)_L$. The VEV of an additional $(4, 1, 2)$ scalar would be sufficient to break the Pati-Salam gauge group down to $SU(3) \times SU(2)_L \times U(1)$, but then the model would not be SAFE. This leaves strong dynamics as the possible origin for this breakdown. We note that the fermion content includes the right-handed neutrino, and a right-handed neutrino condensate does break the Pati-Salam gauge group down in the desired manner.[1] Lepton number is violated, but baryon number and proton stability is preserved.

Here we see the remaining tension in a low scale unification model because there is still some hierarchy between the unification scale and the Higgs mass that remains unexplained. In our case the neutrino condensate would give rise to a massive $SU(4)$ gauge boson which in turn will contribute to the Higgs mass via the diagram in Fig. 4.12. Some other peculiar property of the strong interactions would be needed to explain the suppression of $K \to e\mu$ and the small Higgs mass simultaneously.

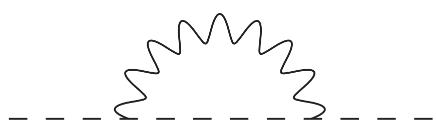

Figure 4.12: One loop correction to the Higgs mass from an $SU(4)$ gauge boson.

Another property of the model is that no Yukawa couplings are allowed by the Pati-Salam gauge symmetries. So Yukawa couplings would have to be induced by the same strong interactions that break these symmetries. The resulting couplings are not too constrained by symmetries since they need only respect the unbroken SM symmetries. $SU(2)_R$ is broken and so there is no reason to expect $m_t = m_b$ and $SU(4)$ is broken and so there is no reason to expect $m_b = m_\tau$ etc. Dynamically generated Yukawa couplings may seem peculiar but they just correspond to certain induced three-point amplitudes with soft UV behavior, just as dynamical masses are induced two-point amplitudes with soft UV behavior.

With regard to a strong $SU(4)$ there are two other requirements to meet. The first concerns the impact of higher loop corrections on the $SU(4)$ β-function. Because the

[1]The $SU(4)$ preserving condensate $\langle\bar{F}F\rangle$ would break $SU(2)_L \times SU(2)_R$ but the resistance offered by $SU(2)_L \times SU(2)_R$ to this breaking is enhanced by the number of chiral doublets.

one loop contribution is restricted to be small, the higher order contributions can be relatively large. If these contributions are positive then an infrared fixed point (IRFP) can arise that is approached from below. We need to check that it is large enough for dynamical symmetry breaking. The second requirement is that we need the $SU(3)$ β-function to turn sufficiently positive below this breaking scale, so that α_s can approach the desired ~ 0.12 value at the electroweak scale. The fact that it does turn positive is to be expected since $SU(4)$ has a small negative β-function, and the removal of a negative gauge contribution due to $SU(4)$ breaking can turn it positive. In other words it is the additional vector-like fermions in the model that can produce a positive $SU(3)$ β-function. Here we find a $SU(3)$ IRFP that is approached from above, but only down to the mass scale of these fermions. These fermion masses could thus be close to a TeV.

From the first requirement the number n'_f of vector-like fermions present in the theory at the $SU(4)$ breaking scale needs to be less than the number n_f listed in (4.30). (The fermions not present must have some larger mass.) From the second requirement n'_f cannot be too small. By considering 4-loop β-functions [94] we find that perhaps the best compromise is $2n_F + n'_f = 15$. Then the $SU(4)$ IRFP is at $\alpha_4 \sim 0.43$ while the $SU(3)$ IRFP is at $\alpha_s \sim 0.12$. The difference between these two numbers is interesting but it is not certain that it is large enough.

4.6 Conclusions

In this chapter we explore the construction of UV complete quantum field theories containing truly elementary scalar fields without UV Landau poles. We extend the old study in [14] to search for SAFEs for semi-simple gauge groups, which is well motivated to achieve low scale unification. The UV property of gravity is far from clear and we restrict ourselves to study β-functions of the coupled system of gauge, Yukawa and quartic couplings.

We review the basic idea of a SAFE in Sec. 4.2 and present numerical results of simple gauge group for comparison with latter analysis. In Sec. 4.3 we generalize the analysis to the semi-simple gauge groups in (4.10), which includes the Pati-Salam model and other low scale unification models as examples. We only consider scalars in fundamental representations, both to incorporate the SM Higgs and to minimize the number of scalar degrees of freedom. We build up four benchmarks for quantitative study and the β-functions are presented in (4.14) and Appendix 4.7. Our main numerical results and analysis are presented in Sec. 4.4. We search for solutions by parameter scan over gauge group size N_i and β-function coefficients b_i. For each N_i set, we find the upper bounds on $r_i \equiv b_i/b_{i,M}$. To provide a guide for model building, we present these upper bounds in Fig. 4.4 and Fig. 4.5 for all benchmarks. In Sec. 4.5 we consider the simplest model that illustrates some of the issues to be faced in SAFE model building.

We list here the properties of the UVFP in SAFEs that we have observed.

- The gauge couplings and typically most of the quartic couplings are running as $1/t$ in fixed ratios.
- Stability demands that the Yukawa couplings vanish more rapidly, $1/t^{\alpha}$ with $\alpha > 1$, as do those quartic couplings that have vanishing $\bar{\lambda}_i$.
- Fewer scalar degrees of freedom helps to achieve SAFEs.
- A hierarchy in the sizes of the different gauge groups helps to achieve SAFEs.
- Among all UVFPs there is always one that is UV stable.
- SAFEs with negative quartic couplings are rare.
- The gauge coupling associated with the largest group is typically constrained to run the slowest of all the couplings. Since its associated b is the smallest, it is the largest coupling in the UV.
- To achieve this small b the theory typically needs some number of vector-like fermions that are only charged under the largest gauge group(s).

If the coupling ratios remain anywhere in the vicinity of the fixed point as the couplings themselves grow larger, then it will be the case that the largest gauge group grows strong first in the infrared. This situation may be related to the real world where the quartic couplings and the gauge couplings of the small electroweak gauge groups are observed to be small. In fact in our simplest model we saw that the IR flow of couplings was such that a linear combination of the quartic couplings was bounded from above.

Yukawa β-functions often have the additional property that they are proportional to the Yukawa couplings to all orders. Thus if they are actually set to their stable fixed point values they are in fact identically vanishing. In our simplest model we saw that the Yukawa couplings identically vanished by gauge symmetry, and thus were only allowed to be generated once the symmetry was broken. It appears that this breakdown and generation of the Yukawa couplings occurs at the scale where the largest gauge group grows strong. The picture is that Yukawa couplings have a dynamical origin in contrast to the truly fundamental gauge and scalar quartic couplings.

It is interesting to compare a SAFE involving several gauge groups to the case of grand unification. In the latter case relations between gauge couplings are fixed by the unification of several gauge groups at some scale. In the SAFE, the ratios of all couplings are flowing to fixed values at the UVFP. But while the theory is fixed in the UV, the theory in the IR is dependent on which flow path the theory is on. A SAFE could be extended to gravity if gravity is also asymptotically free, as is the case for quadratic higher derivative gravity theories. In such a theory all coupling ratios, including gravitational couplings, may be fixed in the deep UV. In this case the ratios of the non gravitational couplings at this ultimate fixed point may differ from what we have described here.

In summary our results show that it might be possible to construct realistic completely asymptotically free gauge theories with complete UV stability containing both fermions and scalars in context of semi-simple gauge groups. This is in contrast to the studies reviewed in [15] that typically suffer from UV instability. Our results may be of interest to unification model building beyond the Pati-Salam model, and it can be generalized to incorporate other scalar representations that may be of interest in that context.

Note Added: As we were finalizing this work we saw the new paper [16]. This paper discusses CAFEs that are not SAFEs, since nonvanishing Yukawa couplings at unstable fixed points are utilized. We also noticed a particular quartic term (third term in their (A.3f)) that we missed that would be present in our Case C with $(4,2,1)$ and $(4,1,2)$ scalars. This term has the same property we discussed for the Levi-Civita term and it does not change the absence of a SAFE in this case. Otherwise our β-functions agree where they overlap up to the normalization of the quartic couplings.

4.7 Appendix: β-functions

In this appendix, we present the one loop β-functions for the quartic couplings for Cases B, C and D. As explained in Sec. 4.3, Yukawa couplings can be neglected in the scalar β-functions in the context of SAFEs. Thus our expressions only contain quartic and gauge couplings terms.

For Case B, we deduce the five one loop β-functions from the potential (4.16),

$$
\begin{aligned}
(4\pi)^2\beta_{\lambda_{d1}} = {} & 4\left[\left(N_AN_B+4\right)\lambda_{d1}^2 + 2\left(N_A+N_B\right)\lambda_{d1}\lambda_{s1} + 3\lambda_{s1}^2\right] + 4\lambda_{d12}\left(N_A\lambda_{d12}+2\lambda_{s12}\right) \\
& - 6\lambda_{d1}\left[\left(N_A - \frac{1}{N_A}\right)g_A^2 + \left(N_B - \frac{1}{N_B}\right)g_B^2\right] \\
& + \frac{3}{4}\left[\left(1+\frac{2}{N_A^2}\right)g_A^4 + \left(1+\frac{2}{N_B^2}\right)g_B^4\right] + 3g_A^2g_B^2\left(1+\frac{1}{N_AN_B}\right)
\end{aligned}
$$

$$
\begin{aligned}
(4\pi)^2\beta_{\lambda_{s1}} &= 4\lambda_{s1}\left[(N_A+N_B)\lambda_{s1}+6\lambda_{d1}\right]+4\lambda_{s12}^2-6\lambda_{s1}\left[\left(N_A-\frac{1}{N_A}\right)g_A^2+\left(N_B-\frac{1}{N_B}\right)g_B^2\right]\\
&+\frac{3}{4}\left[\left(N_A-\frac{4}{N_A}\right)g_A^4+\left(N_B-\frac{4}{N_B}\right)g_B^4\right]-3g_A^2g_B^2\left(\frac{1}{N_A}+\frac{1}{N_B}\right)\\
(4\pi)^2\beta_{\lambda_2} &= 4\left[(N_A+4)\lambda_2^2+N_B\lambda_{d12}(N_A\lambda_{d12}+2\lambda_{s12})+N_B\lambda_{s12}^2\right]-6\lambda_2\left(N_A-\frac{1}{N_A}\right)g_A^2\\
&+\frac{3}{4}g_A^4\left[\left(N_A-\frac{4}{N_A}\right)+\left(1+\frac{2}{N_A^2}\right)\right]\\
(4\pi)^2\beta_{\lambda_{d12}} &= 4\Big[2\lambda_{d12}^2+\lambda_{s12}^2+\lambda_{d1}\left(\left(N_AN_B+1\right)\lambda_{d12}+N_B\lambda_{s12}\right)+\lambda_{s1}\left(\left(N_A+N_B\right)\lambda_{d12}+\lambda_{s12}\right)\\
&+\lambda_2\left(\left(N_A+1\right)\lambda_{d12}+\lambda_{s12}\right)\Big]\\
&-3\lambda_{d12}\left[2\left(N_A-\frac{1}{N_A}\right)g_A^2+\left(N_B-\frac{1}{N_B}\right)g_B^2\right]+\frac{3}{4}\left(1+\frac{2}{N_A^2}\right)g_A^4\\
(4\pi)^2\beta_{\lambda_{s12}} &= 4\lambda_{s12}\left(N_A\lambda_{s12}+4\lambda_{d12}+N_B\lambda_{s1}+\lambda_{d1}+\lambda_2\right)\\
&-3\lambda_{s12}\left[2\left(N_A-\frac{1}{N_A}\right)g_A^2+\left(N_B-\frac{1}{N_B}\right)g_B^2\right]+\frac{3}{4}\left(N_A-\frac{4}{N_A}\right)g_A^4 \qquad (4.31)
\end{aligned}
$$

where N_A denotes the common gauge group.

Case C is split into two benchmarks. In Case C1, by imposing Z_2 symmetry as in (4.18), we deduce one loop β-functions for the four quartic couplings from (4.19).

$$
\begin{aligned}
(4\pi)^2\beta_{\lambda_{d1}} &= 4\left[\left(N_AN_B+4\right)\lambda_{d1}^2+2\left(N_A+N_B\right)\lambda_{d1}\lambda_{s1}+3\lambda_{s1}^2\right]+4N_B\lambda_{d12}\left(N_A\lambda_{d12}+2\lambda_{s12}\right)\\
&-6\lambda_{d1}\left[\left(N_A-\frac{1}{N_A}\right)g_A^2+\left(N_B-\frac{1}{N_B}\right)g_B^2\right]\\
&+\frac{3}{4}\left[\left(1+\frac{2}{N_A^2}\right)g_A^4+\left(1+\frac{2}{N_B^2}\right)g_B^4\right]+3g_A^2g_B^2\left(1+\frac{1}{N_AN_B}\right)\\
(4\pi)^2\beta_{\lambda_{s1}} &= 4\lambda_{s1}\left[(N_A+N_B)\lambda_{s1}+6\lambda_{d1}\right]+4N_B\lambda_{s12}^2-6\lambda_{s1}\left[\left(N_A-\frac{1}{N_A}\right)g_A^2+\left(N_B-\frac{1}{N_B}\right)g_B^2\right]\\
&+\frac{3}{4}\left[\left(N_A-\frac{4}{N_A}\right)g_A^4+\left(N_B-\frac{4}{N_B}\right)g_B^4\right]-3g_A^2g_B^2\left(\frac{1}{N_A}+\frac{1}{N_B}\right)\\
(4\pi)^2\beta_{\lambda_{d12}} &= 4\Big[2\lambda_{d12}^2+\lambda_{s12}^2+2\lambda_{d1}\left(\left(N_AN_B+1\right)\lambda_{d12}+N_B\lambda_{s12}\right)+2\lambda_{s1}\left(\left(N_A+N_B\right)\lambda_{d12}+\lambda_{s12}\right)\\
&-6\lambda_{d12}\left[\left(N_A-\frac{1}{N_A}\right)g_A^2+\left(N_B-\frac{1}{N_B}\right)g_B^2\right]+\frac{3}{4}\left(1+\frac{2}{N_A^2}\right)g_A^4\\
(4\pi)^2\beta_{\lambda_{s12}} &= 4\lambda_{s12}\left(N_A\lambda_{s12}+4\lambda_{d12}+2N_B\lambda_{s1}+2\lambda_{d1}\right)\\
&-6\lambda_{s12}\left[\left(N_A-\frac{1}{N_A}\right)g_A^2+\left(N_B-\frac{1}{N_B}\right)g_B^2\right]+\frac{3}{4}\left(N_A-\frac{4}{N_A}\right)g_A^4 \qquad (4.32)
\end{aligned}
$$

Case C2 denotes the general case without Z_2 symmetry. The one loop β-functions for the six quartic couplings are

$$\begin{aligned}
(4\pi)^2\beta_{\lambda_{d1}} &= 4\left[(N_A N_B+4)\,\lambda_{d1}^2 + 2\,(N_A+N_B)\,\lambda_{d1}\lambda_{s1} + 3\lambda_{s1}^2\right] + 4N_C\lambda_{d12}\,(N_A\lambda_{d12}+2\lambda_{s12})\\
&\quad - 6\lambda_{d1}\left[\left(N_A-\frac{1}{N_A}\right)g_A^2 + \left(N_B-\frac{1}{N_B}\right)g_B^2\right]\\
&\quad + \frac{3}{4}\left[\left(1+\frac{2}{N_A^2}\right)g_A^4 + \left(1+\frac{2}{N_B^2}\right)g_B^4\right] + 3g_A^2 g_B^2\left(1+\frac{1}{N_A N_B}\right)\\
(4\pi)^2\beta_{\lambda_{s1}} &= 4\lambda_{s1}\left[(N_A+N_B)\lambda_{s1}+6\lambda_{d1}\right] + 4N_C\lambda_{s12}^2 - 6\lambda_{s1}\left[\left(N_A-\frac{1}{N_A}\right)g_A^2 + \left(N_B-\frac{1}{N_B}\right)g_B^2\right]\\
&\quad + \frac{3}{4}\left[\left(N_A-\frac{4}{N_A}\right)g_A^4 + \left(N_B-\frac{4}{N_B}\right)g_B^4\right] - 3g_A^2 g_B^2\left(\frac{1}{N_A}+\frac{1}{N_B}\right)\\
(4\pi)^2\beta_{\lambda_{d2}} &= (4\pi)^2\beta_{\lambda_{d1}}(N_B\to N_C,\, g_B\to g_C,\, \lambda_{d1}\to\lambda_{d2},\, \lambda_{s1}\to\lambda_{s2})\\
(4\pi)^2\beta_{\lambda_{s2}} &= (4\pi)^2\beta_{\lambda_{s1}}(N_B\to N_C,\, g_B\to g_C,\, \lambda_{d1}\to\lambda_{d2},\, \lambda_{s1}\to\lambda_{s2})\\
(4\pi)^2\beta_{\lambda_{d12}} &= 4\Big[2\lambda_{d12}^2 + \lambda_{s12}^2 + \lambda_{d1}\left((N_A N_B+1)\,\lambda_{d12} + N_B\lambda_{s12}\right) + \lambda_{s1}\left((N_A+N_B)\,\lambda_{d12}+\lambda_{s12}\right)\\
&\quad + \lambda_{d2}\left((N_A N_C+1)\,\lambda_{d12}+N_C\lambda_{s12}\right) + \lambda_{s2}\left((N_A+N_C)\,\lambda_{d12}+\lambda_{s12}\right)\Big]\\
&\quad - 3\lambda_{d12}\left[2\left(N_A-\frac{1}{N_A}\right)g_A^2 + \left(N_B-\frac{1}{N_B}\right)g_B^2 + \left(N_C-\frac{1}{N_C}\right)g_C^2\right]\\
&\quad + \frac{3}{4}\left(1+\frac{2}{N_A^2}\right)g_A^4\\
(4\pi)^2\beta_{\lambda_{s12}} &= 4\lambda_{s12}\left(N_A\lambda_{s12}+4\lambda_{d12}+N_B\lambda_{s1}+N_C\lambda_{s2}+\lambda_{d1}+\lambda_{d2}\right) - 3\lambda_{s12}\left[2\left(N_A-\frac{1}{N_A}\right)g_A^2\right.\\
&\quad \left. + \left(N_B-\frac{1}{N_B}\right)g_B^2 + \left(N_C-\frac{1}{N_C}\right)g_C^2\right] + \frac{3}{4}\left(N_A-\frac{4}{N_A}\right)g_A^4
\end{aligned} \tag{4.33}$$

They are symmetric under interchange $\lambda_{d1}\to\lambda_{d2}$, $\lambda_{s1}\to\lambda_{s2}$, $N_B\to N_C$ and $g_B\to g_C$. When $N_A=4, N_B=N_C=2$, a new quartic coupling can be constructed by the Levi-Civita symbol as in (4.20). The β-functions are then modified as

$$(4\pi)^2\beta_{di}\to(4\pi)^2\beta_{di}+8\lambda_\epsilon^2,\quad (4\pi)^2\beta_{si}\to(4\pi)^2\beta_{si}-8\lambda_\epsilon^2. \tag{4.34}$$

The β-function of this new coupling is

$$(4\pi)^2\beta_\epsilon = 4\lambda_\epsilon\left[\lambda_{d1}+\lambda_{d2}-\lambda_{s1}-\lambda_{s2}+4(\lambda_{d12}-\lambda_{s12})\right] - \frac{9}{2}\lambda_\epsilon(5g_4^2+g_L^2+g_R^2). \tag{4.35}$$

For Case D, there are one double trace and three single trace couplings. From potential (4.21), we deduce following β-functions,

$$(4\pi)^2\beta_{\lambda_d} = 4\Big[\lambda_d^2\,(N_A N_B N_C+4) + 2\lambda_d\left(\lambda_{s1}\,(N_A+N_B N_C) + \lambda_{s2}\,(N_A N_C+N_B) + \lambda_{s3}\,(N_A N_B+N_C)\right)$$

$$
\begin{aligned}
&+ 2N_A\lambda_{s2}\lambda_{s3} + 2N_B\lambda_{s1}\lambda_{s3} + 2N_C\lambda_{s1}\lambda_{s2} + 3\left(\lambda_{s1}^2 + \lambda_{s2}^2 + \lambda_{s3}^2\right)\Big] \\
&- 6\lambda_d\left[\left(N_A - \frac{1}{N_A}\right)g_A^2 + \left(N_B - \frac{1}{N_B}\right)g_B^2 + \left(N_C - \frac{1}{N_C}\right)g_C^2\right] \\
&+ \frac{3}{4}\left[\left(1 + \frac{2}{N_A^2}\right)g_A^4 + \left(1 + \frac{2}{N_B^2}\right)g_B^4 + \left(1 + \frac{2}{N_C^2}\right)g_C^4\right] + 3\left(\frac{g_A^2 g_B^2}{N_A N_B} + \frac{g_A^2 g_C^2}{N_A N_C} + \frac{g_B^2 g_C^2}{N_B N_C}\right) \\
(4\pi)^2\beta_{\lambda_{s1}} &= 4\Big[\lambda_{s1}^2\left(N_B N_C + N_A\right) + 2\lambda_{s1}\left(3\lambda_d + N_B\lambda_{s2} + N_C\lambda_{s3}\right) + 4\lambda_{s2}\lambda_{s3}\Big] \\
&- 6\lambda_{s1}\left[\left(N_A - \frac{1}{N_A}\right)g_A^2 + \left(N_B - \frac{1}{N_B}\right)g_B^2 + \left(N_C - \frac{1}{N_C}\right)g_C^2\right] \\
&+ \frac{3}{4}g_A^4\left(N_A - \frac{4}{N_A}\right) + 3\left[g_B^2 g_C^2 - g_A^2\left(\frac{g_B^2}{N_B} + \frac{g_C^2}{N_C}\right)\right] \\
(4\pi)^2\beta_{\lambda_{s2}} &= 4\Big[\lambda_{s2}^2\left(N_A N_C + N_B\right) + 2\lambda_{s2}\left(3\lambda_d + N_A\lambda_{s1} + N_C\lambda_{s3}\right) + 4\lambda_{s1}\lambda_{s3}\Big] \\
&- 6\lambda_{s2}\left[\left(N_A - \frac{1}{N_A}\right)g_A^2 + \left(N_B - \frac{1}{N_B}\right)g_B^2 + \left(N_C - \frac{1}{N_C}\right)g_C^2\right] \\
&+ \frac{3}{4}g_B^4\left(N_B - \frac{4}{N_B}\right) + 3\left[g_A^2 g_C^2 - g_B^2\left(\frac{g_A^2}{N_A} + \frac{g_C^2}{N_C}\right)\right] \\
(4\pi)^2\beta_{\lambda_{s3}} &= 4\Big[\lambda_{s3}^2\left(N_A N_B + N_C\right) + 2\lambda_{s3}\left(3\lambda_d + N_A\lambda_{s1} + N_B\lambda_{s2}\right) + 4\lambda_{s1}\lambda_{s2}\Big] \\
&- 6\lambda_{s3}\left[\left(N_A - \frac{1}{N_A}\right)g_A^2 + \left(N_B - \frac{1}{N_B}\right)g_B^2 + \left(N_C - \frac{1}{N_C}\right)g_C^2\right] \\
&+ \frac{3}{4}g_C^4\left(N_C - \frac{4}{N_C}\right) + 3\left[g_A^2 g_B^2 - g_C^2\left(\frac{g_A^2}{N_A} + \frac{g_B^2}{N_B}\right)\right]
\end{aligned} \tag{4.36}
$$

For $N_A = 4, N_B = N_C = 2$ case, the modification of β-functions from the Levi-Civita term in (4.22) is quite similar to that in Case C. We find

$$(4\pi)^2\beta_d \to (4\pi)^2\beta_d + 8\lambda_\epsilon^2, \quad (4\pi)^2\beta_{s1} \to (4\pi)^2\beta_{s1} - 8\lambda_\epsilon^2. \tag{4.37}$$

The β-function of this new coupling is

$$(4\pi)^2\beta_\epsilon = 24\lambda_\epsilon\left(\lambda_d - \lambda_{s1}\right) - \frac{9}{2}\lambda_\epsilon(5g_4^2 + 2g_L^2 + 2g_R^2). \tag{4.38}$$

Chapter 5

UV: Asymptotically Safe Standard Model via Vectorlike Fermions

In this chapter, we explore the asymptotically safe extensions of the Standard Model with the large number-of-flavour techniques. The text in this chapter is reproduced from [18].

5.1 Introduction

Although the Standard Model (SM) of particle interactions is an extremely successful theory of nature, it is an effective theory but not a fundamental one. Following Wilson [2, 3], a theory is fundamental if it features an ultraviolet fixed point. The latter can be either non-interacting (asymptotic freedom) [17, 4, 5, 14, 15, 16, 98, 99, 100, 102, 177] or interacting (asymptotically safe) [25, 103, 104] or mixed [99, 104, 105, 106]. Except for the non-abelian gauge couplings none of the remaining SM couplings features an ultraviolet fixed point.

Here we extend the idea of a safe QCD scenario in [107] to the entire SM. We argue that an asymptotically safe completion of the SM can be realized via new vector-like fermions[1]. Our work relies on the limit of a large number of fermion matter fields, which allows us to perform a $1/N_F$ expansion [26, 109]. Here the relevant class of diagrams can be summed up to arbitrary loop order, leading to an UV interacting fixed point for the (non) abelian interactions of the SM. Thus, we go beyond the cornerstone work of [25] where UV safety is realized in the Veneziano-Witten limit by requiring both N_c and N_F to go to infinity with their ratio fixed, and adjusting it close to the value for which asymptotic freedom is lost. Depending on how these new vector-like fermions obtain

[1]An interesting complementary approach appeared in [108]. Here the authors add new fermions in higher dimensional representations of the SM gauge groups, hoping for a (quasi) perturbative UV fixed point. The models were unable to lead to a safe hypercharge and Higgs self-coupling.

their masses, we can either introduce new scalars that generate fermion masses through new Yukawa operators or, simply introduce explicit vector-like mass operators.

5.2 Building Asymptotic Safety

In the following, we focus on the latter most economical case and explore the following three distinct SM $\mathrm{SU}(3) \times \mathrm{SU}_L(2) \times \mathrm{U}(1)$ charge assignments and multiplicity:

i) N_F $(3, 2, 1/6)$;

ii) N_{F3} $(3, 1, 0) \oplus$ N_{F2} $(1, 2, 1/2)$;

iii) N_{F3} $(3, 1, 0) \oplus N_{F2}$ $(1, 3, 0) \oplus N_{F1}$ $(1, 1, 1)$.

To the above one needs to add, for each model, the associated right charge-conjugated fermions. The above models are to be viewed as templates that allow us to exemplify our novel approach in the search of an asymptotically safe extension of the SM. The basic criterion is that different fermions should have the same charge if it is non-zero; otherwise the summation technique fails (see Eq. (5.4) and the corresponding discussion). In fact we have checked that other models (e.g. $N_{F3}\,(3, 1, 2/3) \oplus N_{F2}\,(1, 3, 0)$ featuring new top primes) lead to similar results as the ones used here[2]. Finally, we neglect (in model (i)) possible mixing among the new vector-like fermions and SM quarks. We start by considering the RG equations describing the gauge-Yukawa-quartic to two loop order including vector-like fermions. We have checked that our results agree for the SM case with the ones in [110, 111]. We used [112, 113] for the vector-like fermions contributions to gauge couplings and [114, 115] for the contributions to the Higgs quartic. The associated

[2]Following our innovative approach, a recent follow-up paper appeared [178], in which the set N_{F3} is abandoned. Here QCD remains asymptotically free while the rest of the SM gauge couplings are still safe.

beta functions read:

$$
\begin{aligned}
\beta_1 &= \frac{d\alpha_1}{dt} = \left(b_1 + c_1\alpha_1 + d_1\alpha_3 + e_1\alpha_2 - \frac{17}{3}\alpha_{y_t}\right)\alpha_1^2 \\
\beta_2 &= \frac{d\alpha_2}{dt} = \left(-b_2 + c_2\alpha_2 + d_2\alpha_3 + e_2\alpha_1 - 3\alpha_{y_t}\right)\alpha_2^2 \\
\beta_3 &= \frac{d\alpha_3}{dt} = \left(-b_3 + c_3\alpha_3 + d_3\alpha_2 + e_3\alpha_1 - 4\alpha_{y_t}\right)\alpha_3^2 \\
\beta_{y_t} &= \frac{d\alpha_{y_t}}{dt} = \left(9\alpha_{y_t} - \frac{9}{2}\alpha_2 - 16\alpha_3 - \frac{17}{6}\alpha_1\right)\alpha_{y_t} + \beta_{y_t}^{2\mathrm{loop}} \\
\beta_{\alpha_h}^{1\mathrm{loop}} &= \frac{d\alpha_h}{dt} = \frac{3}{8}\left(\alpha_1^2 + 3\alpha_2^2 + 2\alpha_1\left(\alpha_2 - 4\alpha_h\right) + \right. \\
&\qquad \left. + 64\alpha_h^2 - 24\alpha_2\alpha_h + 32\alpha_h\alpha_{y_t} - 16\alpha_{y_t}^2\right) \\
\beta_{\alpha_h}^{2\mathrm{loop}} &= \frac{1}{6}\left(-4D_{R_3}S_2\left(R_2\right)\alpha_2^2 N_{F2}\left(2\alpha_1 + 6\alpha_2 - 15\alpha_h\right)\right. \\
&\left. - 4D_{R_3}D_{R_2}\alpha_1^2 Y^2 N_{F1}\left(2\alpha_1 + 2\alpha_2 - 5\alpha_h\right)\right) + \beta_{\alpha_h\,2\mathrm{loop}}^{\mathrm{SM}} \\
\beta_{\alpha_h\,2\mathrm{loop}}^{\mathrm{SM}} &= \frac{1}{48}\left(-379\alpha_1^3 - 559\alpha_2\alpha_1^2 - 289\alpha_2^2\alpha_1 + 915\alpha_2^3\right) \\
&\quad + \frac{1}{48}\left(1258\alpha_1^2 + 468\alpha_2\alpha_1 - 438\alpha_2^2\right)\alpha_h - 312\alpha_h^3 \\
&\quad + \frac{1}{48}\left(1728\alpha_1 + 5184\alpha_2\right)\alpha_h^2
\end{aligned}
\tag{5.1}
$$

where $t = \ln\left(\mu/M_Z\right)$ and α_1, α_2, α_3, α_{y_t}, α_h are the U(1), SU(2), SU(3), top-Yukawa and Higgs self-couplings respectively and we have used the normalization

$$
\alpha_i = \frac{g_i^2}{(4\pi)^2}, \quad \alpha_{y_t} = \frac{y_t^2}{(4\pi)^2}, \quad \alpha_h = \frac{\lambda_h}{(4\pi)^2}\,. \tag{5.2}
$$

$\beta_{\alpha_h\,2\mathrm{loop}}^{\mathrm{SM}}$ and $\beta_{y_t}^{2\mathrm{loop}}$ represent two loop SM contributions to the RG functions of α_h and α_{y_t}, which are not shown explicitly. D_{R_2}, D_{R_3} represent the dimensions of the representations (R_2, R_3) under $SU(2)$ and $SU(3)$ while $S_2\left(R_2\right)$ represents the Dynkin index of the representation R_2. The contributions of the SM chiral fermions are encoded in $b_1, b_2, b_3, c_1, c_2, c_3, d_1, d_2, e_2, e_3$ in Eq.(5.3) and can be distinguished from the new vector-like contributions that are all proportionals to a "D_R" coefficient

$$\begin{aligned}
b_1 &= \frac{41}{3} + \frac{8}{3}Y^2 N_{\rm F} D_{R_2} D_{R_3}, \quad c_1 = \frac{199}{9} + \frac{8}{3}Y^4 N_F D_{R_2} D_{R_3} \\
b_2 &= \frac{19}{3} - \frac{4N_F}{3} D_{R_3}, \quad c_2 = \frac{35}{3} + \frac{49N_F}{3} D_{R_3} \\
b_3 &= 14 - \frac{4N_F}{3} D_{R_2}, \quad c_3 = -52 + \frac{76N_F}{3} D_{R_2} \\
d_1 &= \frac{88}{3} + \frac{32}{3}Y^2 N_F D_{R_2} D_{R_3}, \ e_1 = 9 + 6Y^2 N_F D_{R_2} D_{R_3} \\
d_2 &= 24 + \frac{16}{3} N_F D_{R_3}, \quad e_2 = 3 + 4Y^2 N_{\rm F} D_{R_3} \\
d_3 &= 9 + 3N_F D_{R_2}, \quad e_3 = \frac{11}{3} + 4N_F Y^2 D_{R_2} \,,
\end{aligned} \tag{5.3}$$

where for simplicity, the above explicit coefficients only apply to fundamental representations (models (i) and (ii)); for higher dimension representations the corresponding Casimir invariants and the Dynkin index should be incorporated.

The following diagrams (see Fig. 5.1) encode the infinite tower of higher order contributions to the self-energies related to the gauge couplings. These diagrams can be summed up analytically (the abelian and non-abelian cases were first computed respectively in [27] and [28]).

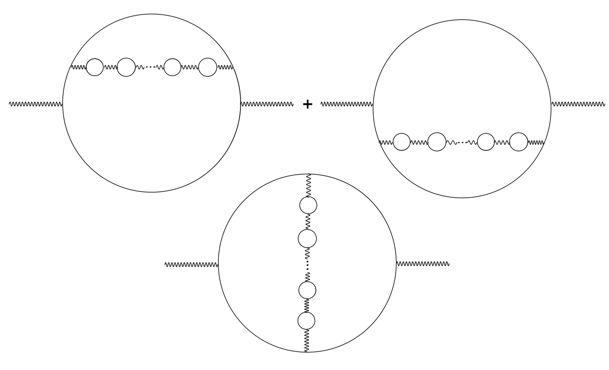

Figure 5.1: Higher order self-energy diagram

To the leading $1/N_F$ order, the higher order (ho) contributions to the RG functions of β_2 and β_3 are given by [26] and have been generalized to the case with any hypercharge Y and semi-simple group (F_1 first appeared in [27]):

$$\beta_{\rm ho1} = \frac{2A_1\alpha_1}{3}\frac{F_1(A_1)}{N_F}; \quad \beta_{\rm hoi} = \frac{2A_i\alpha_i}{3}\frac{H_{1i}(A_i)}{N_F} \quad (i = 2, 3) \,, \tag{5.4}$$

where

$$
\begin{aligned}
A_1 &\equiv 4\alpha_1 N_F Y^2 D_{R_2} D_{R_3}; \quad A_2 \equiv 2\alpha_2 N_F D_{R_3} \\
A_3 &\equiv 2\alpha_3 N_F D_{R_2} \\
F_1 &= \int_0^{A/3} I_1(x) dx \\
H_{1i} &= \frac{-11}{2} N_{ci} + \int_0^{A/3} I_1(x) I_2(x) dx \qquad (N_{ci} = 2, 3) \\
I_1(x) &= \frac{(1+x)(2x-1)^2(2x-3)^2 \sin(\pi x)^3}{(x-2)\pi^3} \\
&\times \left(\Gamma(x-1)^2 \Gamma(-2x)\right) \\
I_2(x) &= \frac{N_{ci}^2 - 1}{N_{ci}} + \frac{(20 - 43x + 32x^2 - 14x^3 + 4x^4)}{2(2x-1)(2x-3)(1-x^2)} N_{ci} \, .
\end{aligned}
$$

We recall that the validity of the summation depends on our first criterion which implies that for each gauge group we have only a single A_i, constraining the possible vector-like models. F_1 has poles at $A = 15/2 + 3n$ while H_{1i} has poles at $A = 3, 15/2, \cdots, 3n + 9/2$. In this chapter we concentrate on the first UV pole branch ($A = 15/2$ for F_1 and $A = 3$ for H_{1i}). Note that the pole structure of H_{1i} is the same for all the non-abelian groups, implying that when N_F is fixed, the non-abelian gauge coupling values will be very close to each other if $D_{R_2} = D_{R_3}$. The presence of the UV poles at F_1 and H_{1i} guarantees the existence of an UV safe fixed point for the gauge couplings. Note that the functions F_1 and H_{1i} are scheme independent according to [116]. We therefore expect the pole structure and the related UV fixed points to be scheme independent. Physical quantities, such as scaling exponents, were computed in [25]. The $1/N_F^2$ terms are negligible for N_F sufficiently large. Specifically, as pointed out in [26], for $SU(3)$ one finds that N_F needs to be larger than 32 while for $U(1)$ one finds $N_F \geq 16$.

Thus the total RG functions for the gauge-Yukawa subsystem can be written as:

$$
\begin{aligned}
\beta_{1tot} &= \beta_1(\alpha_{1tot}, \alpha_{2tot}, \alpha_{3tot}, \alpha_{y_t tot}) + \beta_{\text{ho1}}(\alpha_{1tot}) \\
\beta_{3tot} &= \beta_3(\alpha_{1tot}, \alpha_{2tot}, \alpha_{3tot}, \alpha_{y_t tot}) + \beta_{\text{ho3}}(\alpha_{3tot}) \\
\beta_{2tot} &= \beta_2(\alpha_{1tot}, \alpha_{2tot}, \alpha_{3tot}, \alpha_{y_t tot}) + \beta_{\text{ho2}}(\alpha_{2tot}) \\
\beta_{y_t tot} &= \left(9\alpha_{y_t tot} - \frac{9}{2}\alpha_{2tot} - 16\alpha_{3tot}\right) \alpha_{y_t tot} + \beta^{\text{2loop}}_{y_t tot} ,
\end{aligned}
\tag{5.5}
$$

where α_{itot} corresponds to the gauge couplings including the leading $1/N_F$ contribution to the self-energy diagrams, and $\alpha_{y_t tot}$ is the accordingly modified Yukawa coupling. We also avoided the double counting problem due to the simultaneous presence of the

c_i $(i = 1, 2, 3)$ terms in Eq. (5.1) and the leading terms of β_{ho2}, β_{ho3} in Eq. (5.4). We employ the MS scheme, which is a mass independent RG scheme allowing us to investigate the running of the couplings independently of the running vector-like masses, except for threshold corrections that can be shown to be controllably small.

Solving Eqs. (5.5), we obtain the running coupling solutions depicted in Fig. 5.2 by the blue, green, red and purple curves, corresponding respectively to the U(1), SU(2), SU(3) gauge couplings and top Yukawa coupling; the orange curve corresponding to the Higgs coupling has not yet been included. It is clear that all the gauge couplings are UV asymptotically safe while the top Yukawa coupling is asymptotically free. Note that the sub-system encounters an interacting UV fixed point at 3.2×10^{13} GeV which is safely below the Planck scale and so gravity contributions can be safely ignored. For the UV fixed point to exist, the choice of the initial value of the gauge coupling is not crucial since the only requirement is $\alpha_i\,(t_0) < \alpha_i\,(t_*)\,,\ (i = 1, 2, 3)$ where $t_0 = \ln\left(\mu_0/M_Z\right)$ is an arbitrary initial scale and t_* is the scale for the UV fixed point. For simplicity, instead of sequentially introducing new vectorlike fermions, we assume they are introduced all at once at a particular scale[3] near their MS-scheme mass $m(m) = m$ ($m \approx \mu = 2\,\text{TeV}$ (or $t = 3$) in Fig. 5.2). Note that a too small N_F will fail the $1/N_F$ expansion. To produce

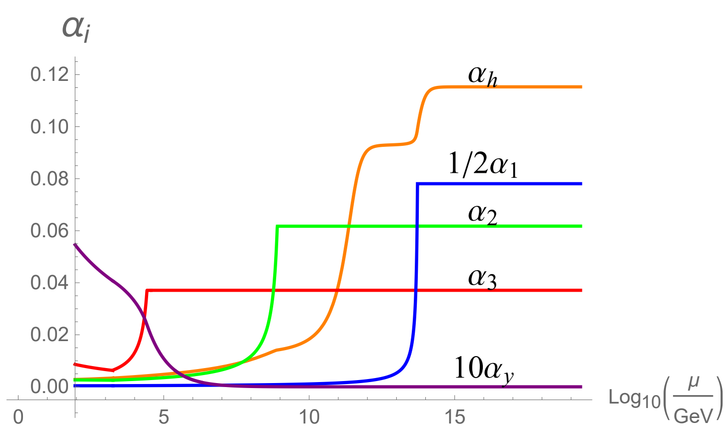

Figure 5.2: Running of the gauge-Yukawa couplings as function of the RG time with $\log_{10}$ base using model (ii) (N_{F3} $(3, 1, 0) \oplus N_{F2}$ $(1, 2, 1/2)$). The blue, green, red and purple curves correspond respectively to the U(1), SU(2), SU(3) gauge and top Yukawa couplings. The top Yukawa coupling α_y and $U(1)$ gauge coupling α_1 have been rescaled by a factor 10 and 1/2 respectively to fit all couplings on one figure. The orange curve depicts the two loop level Higgs quartic coupling α_h in the same model. Here $N_{F3} = 40, N_{F2} = 24$ and the initial values of the gauge and Yukawa couplings are chosen to be the SM coupling values at 2 TeV while the Higgs quartic coupling is chosen to be 0.0034.

Fig. 5.2, we have used model (ii) with $N_{F3} = 40, N_{F2} = 24$ with the initial values of the

[3] We have checked that our results change very little if we employ different vector-like fermion masses corresponding to a larger matching scale e.g. $m \approx \mu = 100\,\text{TeV}$; the UV fixed point transition scale increases accordingly to around 10^{16} GeV.

gauge and Yukawa couplings chosen to be the SM coupling values at 2 TeV corresponding to $t_0 = 3$:

$$\begin{aligned} \alpha_3(t_0) &= 0.00661 \quad \alpha_2(t_0) = 0.00256 \\ \alpha_1(t_0) &= 0.00084 \quad \alpha_y(t_0) = 0.00403 \end{aligned} \tag{5.6}$$

We emphasize that the basic features of the gauge and Yukawa curves in Fig. 5.2 are generic and not limited only to model (ii). Figures similar to Fig. 5.2 result for all three vector-like fermion models (i, ii, iii).

We next consider the Higgs quartic coupling whose beta function to two loop order is given in Eq. (5.1). We first plot β_{α_h} as a function of α_h for model (ii) with the values of the gauge and Yukawa couplings at the fixed point and $N_{F3} = 40, N_{F2} = 24$. Fig. 5.3 shows that there exist four different regions denoted as I, II, III, IV. Depending on the choice of the initial value of α_h, the Higgs self-coupling can be in any of these distinct phases. Because we are searching for asymptotic safety we are only interested in phase III. To guide the reader we mark with a red dot in Fig. 5.3 the ultraviolet critical value[4] of α_h. The plot shows that for the Higgs self-coupling to be asymptotically safe it must run towards the ultraviolet to values within region III, where the other couplings have already reached their fixed point values. If, however, the dynamics is such that it will run towards ultraviolet values immediately below the critical one the ultimate fate, dictated by phase II, is vacuum instability.

Fig. 5.3 also provides a few insights for constraining viable vector-like fermion models. The expression of $\beta_{\alpha_h}^{\text{2loop}}$ in Eq. (5.1) shows the new vector-like fermions will only provide negative contributions to $\beta_{\alpha_h}^{\text{2loop}}$ when N_{F2} is order of 10. In conjunction with Fig. 5.3, we expect that the smaller the negative contribution of these new vector-like fermions, the smaller the critical value of α_h, and the easier to enter phase III. Actually, we find that the pure SM RG function of α_h (without new vector-like fermion contributions to β_{α_h} only) provides the smallest critical value of α_h, commensurate with the above expectation. Alternatively, if these negative contributions are too large, the cubic curve of β_{α_h} will never intersect the α_h axis and we will never achieve an asymptotically safe solution (only two phases remain in this limiting case). We learn that the smaller the hypercharge and dimension of the representation, the smaller will be the critical value of α_h (making it easier to realize asymptotic safety for the Higgs quartic). Following this

[4]We distinguish the ultraviolet critical value with the initial critical value of α_h, discussed later. The former quantity is scale dependent; thus the ultraviolet critical α_h is at a scale close to the UV fixed point. The latter quantity is an IR quantity, above which the Higgs self-coupling flows to an UV fixed point; we shall take this inital critical α_h to be at 2 TeV.

criterion, model (ii) should have the smallest critical value of α_h.

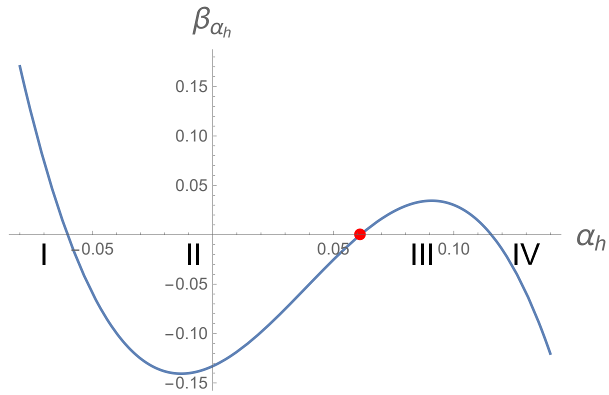

Figure 5.3: This figure shows β_{α_h} with α_h with the values of the gauge and Yukawa couplings at the fixed point and $N_{F3} = 40, N_{F2} = 24$. There exists four different kinds of phases denoted as I, II, III, IV dependent on the initial value of α_h. The red point denotes the ultraviolet critical value of α_h which determines whether we could have a UV safe fixed point with positive or negative α_h value.

We obtain the same results for the gauge and Yukawa couplings as before, taking their initial values to be the SM ones at 2 TeV as in (5.6). We find that to obtain an asymptotically safe solution for α_h we must choose its initial value to be (at least) $\alpha_h(t = 3) = 0.0034$, about six times the SM value at that scale. For the SM initial value $\alpha_h(t_0) = 0.00054$ the theory achieves the negative value $\alpha_h = -0.06$ at the UV fixed point, yielding an unstable vacuum. The results for model (ii) (again using $N_{F3} = 40, N_{F2} = 24$) are shown in Fig. 5.2, with the Higgs quartic coupling in orange.

We thus attain UV completion for the whole gauge-Yukawa-Higgs system with gauge and Higgs quartic couplings $(\alpha_1, \alpha_2, \alpha_3, \alpha_h)$ asymptotically safe and top Yukawa coupling α_t asymptotically free. The UV fixed point occurs at 3.6×10^{14} GeV – well below the Planck scale and so gravity contributions can be safely ignored. The unique feature in Fig. 5.2 occurs because when α_2 reaches its fixed point value β_{α_h} almost vanishes. However when α_1 increases to its final value the almost fixed point in the scalar coupling settles to its true fixed point value. In addition this feature, for fixed $N_{F3} = 40$, disappears gradually when increasing N_{F2} from 18 to 25. This is because the larger N_{F2}, the smaller α_2 is; consequently the self-coupling is more sensitive to the change in α_1.

We have further explored which regions of parameter space $(\alpha_h, N_{F3}, N_{F2})$ can yield asymptotic safety. We find that α_h reaches its lowest critical value of 0.0027 when $N_{F2} = 18$ and $32 \leq N_{F3} \leq 220$ (insensitive to N_{F3} and the bounds of N_{F3} are discussed below). This critical α_h value can be further decreased by considering large N_F of order a few hundred. Interestingly, there exists an upper value of N_F above which the A in Eq. (5.4) goes beyond the first UV pole, moving therefore to the second branch of F_1 and

H_1. Within the first branch, the smallest critical α_h with large N_F occurs for $\alpha_h = 0.002$ with N_{F2} near and slightly below the boundary (say $N_{F2} = 590$) above which one needs to move to the second branch. The result is insensitive to N_{F3} as well and $32 \leq N_{F3} \leq 220$ where the upper bound $N_{F3} = 220$ is due to the second branch of α_3 while the lower bound $N_{F3} = 32$ is to satisfy leading $1/N_F$ expansion. The UV fixed point occurs below but near the Planck scale. An initial investigation of these other branches suggest that a SM Higgs self-coupling value might be reached, but we leave in-depth investigations for future studies.

Comparing models (i) and (ii), we find that the critical value of α_h is overall much higher for model (i). However, similar to model (ii), at very large N_F one can decrease α_h below $\alpha_h(t_0) = 0.0049$, corresponding to the lowest critical value one can achieve for small N_F. For example, for an initial value of $\alpha_h = 0.0035$ one encounters a UV fixed point provided $N_F \geq 105$. It is possible to further decrease α_h with increasing N_F.

For model (iii), we have a similar trend as the previous models. For simplicity, we consider the case where $N_{F1} = N_{F2}$ and note that to achieve $\alpha_h = 0.0035$ (still quite large compared to the SM), one needs $N_{F3} = 40$ and $N_{F1} = N_{F2} \geq 131$. Here we find the smallest critical Higgs self-coupling occurs for $\alpha_h = 0.00176$ with $N_{F1} = 2200, N_{F2} = 147, N_{F3} = 138$. These values correspond to the uppermost values allowed by the first branches of the corresponding F_1 and H_1 functions. This Higgs quartic value is, however, still three times its SM one at 2 TeV, which is roughly two times the value at the electroweak scale. We expect that the critical α_h further decreases in the second branch when considering even larger N_F. We have checked that our results are stable against the introduction of known higher order terms in $1/N_F$ proportional to the $F_{2\sim4}$ and $H_{2\sim4}$ functions.

5.3 Conclusion

Summarising, for all three vector-like-fermion models, with SM gauge and top Yukawa couplings values as initial conditions at IR, we are able to realize UV completion of the gauge-Yukawa subsystem (gauge couplings asymptotically safe and Top Yukawa coupling asymptotically free). Upon including the Higgs quartic coupling, we find that its initial low energy value must attain a certain threshold for a given choice of the number of vector-like fermions. Above this critical value, we attain a UV asymptotically safe completion, whereas below this value the system is UV unstable. For the three vector-like-fermion models we studied, model (ii) possesses the lowest critical value of $\alpha_h = 0.0027$ for a relatively small number of flavours N_F. This value is still larger than the (as yet unmeasured) SM Higgs quartic coupling. If at future colliders the Higgs quartic coupling is found to be $5-6$ times larger (predicted in some studies without altering the SM RG functions e.g. [117]), model (ii) could realize asymptotic safety for the whole gauge-Yukawa-Higgs system. Intriguingly an α_h close to the SM value, say around 2 times at electroweak scale, can be achieved for very large values of N_{F1} in model (iii) within the first branch of the F_1 and H_1 functions. This allows complete asymptotic safety at energies below but near the Planck scale.

Our results pave the way to new approaches for making the SM fully asymptotically safe[5].

[5]Indeed, building on the present approach in [178] it has been shown that one can construct related asymptotically safe SM extensions in which the Higgs quartic coupling matches the SM value. In [182] instead, asymptotic safety is achieved via dynamical symmetry breaking of a calculable UV fixed point.

Chapter 6

IR: Quark matter may not be strange

We finished our exploration of UV physics in previous chapters. Now we switch our discussion to the dense matter physics at the infrared scale in this chapter. With a phenomenological quark-meson model that can accommodate the density-dependent and flavour-dependent feedback of QCD vacuum, we obtain an unprecedented result that non-strange quark matter (udQM) is more stable than the strange quark matter and normal nuclear matter for baryon number $A > A_{\rm min}$ with $A_{\rm min} \gtrsim 300$. The text in this chapter is reproduced from [19].

6.1 Introduction

Hadronic matter is usually thought to be the ground state of baryonic matter (matter with net baryon number) at zero temperature and pressure. Then quark matter only becomes energetically favorable in an environment like at a heavy ion collider or deep inside the neutron star. However as proposed by Witten [55] (with some relation to earlier work [54, 56, 119, 120]), quark matter with comparable numbers of u, d, s, also called strange quark matter (SQM), might be the ground state of baryonic matter, with the energy per baryon $\varepsilon \equiv E/A$ even smaller than 930 MeV for the most stable nuclei ^{56}Fe.

With the lack of a first-principles understanding of the strong dynamics, the MIT bag model [121] has long been used as a simple approximation to describe quark matter. In this model constituent quark masses vanish inside the bag, and SQM is found to reach lower energy than quark matter with only u, d quarks (udQM). If SQM is the ground state down to some baryon number $A_{\rm min}$, as long as the transition of ordinary heavy nuclei with $A > A_{\rm min}$ to SQM needs a simultaneous conversion of a sufficiently large number of down quarks to strange quarks, the conversion rate can be negligibly small [52]. A faster catastrophic conversion could occur if the ground state was instead udQM. So quite often the energy per baryon is required to satisfy $\varepsilon_{\mathrm{SQM}} \lesssim 930\,\mathrm{MeV} \lesssim \varepsilon_{ud\mathrm{QM}}$ [52, 122].

On the other hand, since the periodic table of elements ends for $A \gtrsim 300$, this catastrophe can be avoided if $A_{\mathrm{min}} \gtrsim 300$ for udQM. It is also recognized that the bag model may not adequately model the feedback of a dense quark gas on the QCD vacuum. How the u, d, s constituent quark masses respond to the gas should account for the fact that flavour symmetry is badly broken in QCD. This can be realized in a quark-meson model by incorporating in the meson potential the flavour breaking effects originating in the current quark masses. Through the Yukawa term the quark densities drive the scalar fields away from their vacuum values. The shape of the potential will then be important to determine the preferred form of quark matter. This effect has already been seen in NJL and quark-meson models [57, 58, 123, 124, 125]. These are studies in the bulk limit and they tend to find that udQM has lower ε than SQM with the conclusion that neither is stable.

The possibility that udQM is actually the ground state of baryonic matter has been ignored in the literature, but it shall be our focus in this letter. With an effective theory for only the scalar and pseudoscalar nonets of the sub-GeV mesons with Yukawa coupling to quarks, we demonstrate a robust connection between the QCD spectrum and the conditions for a udQM ground state in the bulk, i.e. $\varepsilon_{ud\mathrm{QM}} \lesssim 930\,\mathrm{MeV}$ and $\varepsilon_{ud\mathrm{QM}} < \varepsilon_{\mathrm{SQM}}$. We shall also show that surface effects are of a size that can ensure that $A_{\mathrm{min}} \gtrsim 300$ by numerically solving the scalar field equation of motion. This points to the intriguing possibility that a new form of stable matter consisting only of u, d quarks might exist not far beyond the end of the periodic table.

6.2 The meson model

Here we study an effective theory describing the mass spectra and some decay rates of the scalar and pseudoscalar nonets of the sub-GeV mesons. The QCD degrees of freedom not represented by these mesons are assumed to be integrated out and encoded in the parameters of the phenomenological meson potential. We view our description as dual to one that contains vector mesons [126]. With the parameters determined from data, we can then extrapolate from the vacuum field values to the smaller field values of interest for quark matter.

We find that a linear sigma model provides an adequate description without higher dimensional terms,

$$\mathcal{L}_m = \mathrm{Tr}\left(\partial_\mu \Phi^\dagger \partial^\mu \Phi\right) - V, \quad V = V_{\mathrm{inv}} + V_b. \tag{6.1}$$

$\Phi = T_a(\sigma_a + i\pi_a)$ is the meson field and $T_a = \lambda_a/2$ ($a = 0, \ldots, 8$) denotes the nine generators of the flavour $U(3)$ with $\mathrm{Tr}(T_a T_b) = \delta_{ab}/2$. V_{inv} is chirally invariant,

$$V_{\mathrm{inv}} = \lambda_1 \left(\mathrm{Tr}\,\Phi^\dagger\Phi\right)^2 + \lambda_2\,\mathrm{Tr}\left((\Phi^\dagger\Phi)^2\right) + m^2\,\mathrm{Tr}\left(\Phi^\dagger\Phi\right) - c\left(\det\Phi + h.c.\right). \tag{6.2}$$

The c term is generated by the 't Hooft operator. Boundedness from below requires that $\lambda_1 + \lambda_2/2 > 0$. For there to be spontaneous symmetry breaking in the absence of V_b requires that $8m^2(3\lambda_1 + \lambda_2) < c^2$.

$V_b = \sum_{i=1}^{8} V_{bi}$ describes the explicit $SU(3)$ flavour breaking by incorporating the current quark mass matrix $\mathcal{M} = \mathrm{diag}(m_{u0}, m_{d0}, m_{s0})$.

$$\begin{aligned}
V_{b1} &= b_1\,\mathrm{Tr}\left(\Phi^\dagger\mathcal{M} + h.c.\right), \\
V_{b2} &= b_2\epsilon_{ijk}\epsilon_{mnl}\mathcal{M}_{im}\Phi_{jn}\Phi_{kl} + h.c., \\
V_{b3} &= b_3\,\mathrm{Tr}\left(\Phi^\dagger\Phi\Phi^\dagger\mathcal{M}\right) + h.c., \\
V_{b4} &= b_4\,\mathrm{Tr}\left(\Phi^\dagger\Phi\right)\mathrm{Tr}\left(\Phi^\dagger\mathcal{M}\right) + h.c., \\
V_{b5} &= b_5\,\mathrm{Tr}\left(\Phi^\dagger\mathcal{M}\Phi^\dagger\mathcal{M}\right) + h.c., \\
V_{b6} &= b_6\,\mathrm{Tr}\left(\Phi\Phi^\dagger\mathcal{M}\mathcal{M}^\dagger + \Phi^\dagger\Phi\mathcal{M}^\dagger\mathcal{M}\right), \\
V_{b7} &= b_7\left(\mathrm{Tr}\,\Phi^\dagger\mathcal{M} + h.c.\right)^2, \\
V_{b8} &= b_8\left(\mathrm{Tr}\,\Phi^\dagger\mathcal{M} - h.c.\right)^2.
\end{aligned} \tag{6.3}$$

Other possible terms have been eliminated by a field redefinition [127]. We adopt $m_{s0} = 94\,\mathrm{MeV}$ and $m_{ud0} = 3.4\,\mathrm{MeV}$ [37]. This general set of terms is successful at describing the lightest scalar and pseudoscalar nonets, with all masses below 1 GeV, which is typically not possible when keeping the V_{b1} term only [36, 38, 40]. The size of the b_i coefficients are made more meaningful by normalizing w.r.t. the estimates of Naive Dimensional Analysis (NDA) [128] to obtain dimensionless NDA couplings,

$$\begin{aligned}
\bar{\lambda}_{1,2} &= \frac{f_\pi^2}{\Lambda^2}\lambda_{1,2}, \ \bar{m}^2 = \frac{1}{\Lambda^2}m^2, \ \bar{c} = \frac{f_\pi}{\Lambda^2}c, \ \bar{b}_1 = \frac{1}{f_\pi\Lambda}b_1, \\
\bar{b}_2 &= \frac{1}{\Lambda}b_2, \ \bar{b}_{3,4} = \frac{f_\pi}{\Lambda}b_{3,4}, \ \bar{b}_{5-8} = b_{5-8}.
\end{aligned} \tag{6.4}$$

f_π is the pion decay constant and $\Lambda = 4\pi f_\pi$ is an effective cutoff.

In the meson model chiral symmetry breaking of QCD is realized by the non-zero vacuum expectation values of the neutral scalar meson fields at the potential minimum,

$\langle\Phi\rangle = T_0 v_0 + T_8 v_8 = \frac{1}{2}\text{diag}(v_n, v_n, \sqrt{2}v_s)$, where we use the non-strange and strange flavour basis: $\sigma_n = \frac{\sqrt{2}}{\sqrt{3}}\sigma_0 + \frac{1}{\sqrt{3}}\sigma_8$, $\sigma_s = \frac{1}{\sqrt{3}}\sigma_0 - \frac{\sqrt{2}}{\sqrt{3}}\sigma_8$. The deformation by $\mathcal{M}$ naturally implies an $SU(3)$ breaking vacuum $v_n \neq \sqrt{2}v_s$. A standard gauging of the model then leads to $v_n = f_\pi = 92\,\text{MeV}$, $v_s = \sqrt{2}f_K - f_\pi/\sqrt{2} = 90.5\,\text{MeV}$ [37, 38].

The mass spectra for the scalar and pseudoscalar nonets are derived by $\mathbb{M}^2_{s,ab} = \partial^2 V/\partial\sigma_a\partial\sigma_b$ and $\mathbb{M}^2_{p,ab} = \partial^2 V/\partial\pi_a\partial\pi_b$. With isospin symmetry the eight independent masses are $m^2_{a_0} = \mathbb{M}^2_{s,11}$, $m^2_\kappa = \mathbb{M}^2_{s,44}$, $m^2_\pi = \mathbb{M}^2_{p,11}$, $m^2_K = \mathbb{M}^2_{p,44}$ and $m^2_\sigma, m^2_{f_0}, m^2_\eta, m^2_{\eta'}$ after diagonalizing the $(0,8)$ sectors. The rotations are defined as: $\sigma_0 = \cos\theta_s\sigma - \sin\theta_s f_0$, $\sigma_8 = \sin\theta_s\sigma + \cos\theta_s f_0$ and $\pi_0 = \cos\theta_p\eta' - \sin\theta_p\eta$, $\pi_8 = \sin\theta_p\eta' + \cos\theta_p\eta$.

We solve the 12 free parameters (λ_1, λ_2, c, m^2, b_1, ..., b_8) in (6.1) in terms of two decay constants, eight meson masses and two mixing angles. θ_p is related to the diphoton radiative decay widths of η', η and the strong decay widths of a_0, κ. θ_s needs to fit the small and large $\pi\pi$ widths of f_0 and σ respectively, which implies that the σ meson is quite close to the non-strange direction.

Table 6.1: The NDA couplings for benchmarks

	$\bar{\lambda}_1$	$\bar{\lambda}_2$	$\bar{m}^2$	$\bar{c}$	$\bar{b}_1$	$\bar{b}_2$
Set 1	-0.06	0.33	-0.13	0.33	-4.4	0.19
Set 2	0.04	0.16	0.05	0.27	-1.6	-0.14
	$\bar{b}_3$	$\bar{b}_4$	$\bar{b}_5$	$\bar{b}_6$	$\bar{b}_7$	$\bar{b}_8$
Set 1	-4.2	2.5	-3.0	50	1.4	4.7
Set 2	-0.18	0.09	4.0	5.2	-3.9	-5.5

Table 6.1 presents two benchmarks for the meson model. The parameters of set 1 are chosen to give a good fit to the data, however this leads to a rather large value for the NDA coupling $\bar{b}_6$. Given the theoretical uncertainties associated with the neglected higher dimensional terms, allowing the masses and decay widths to depart from the experimental values could be more sensible. An example with up to 10% departures gives the smaller NDA couplings of set 2.

Table 6.2 compares the experimental values [37] with the results of the two benchmarks, including predictions for some decay widths. The f_0, a_0 widths have large KK threshold corrections and so for these Flatté [129] rather than Breit-Wigner widths are used. In these cases we also compare to ratios R_{f_0}, R_{a_0} that involve the strange and non-

Table 6.2: The meson masses (in MeV), mixing angles, and decay widths (in MeV, keV for scalar, pseudoscalar).

	m_π	m_K	m_η	m'_η	θ_p
Exp	138	496	548	958	NA
Set 1	138	496	548	958	$-15.0°$
Set 2	148	454	569	922	$-10.8°$
	m_{a_0}	m_κ	m_σ	m_{f_0}	θ_s
Exp	980 ± 20	700-900	400-550	990 ± 20	NA
Set 1	980	900	555	990	31.5°
Set 2	887	916	555	955	21.7°
	$\Gamma_{\eta\to\gamma\gamma}$	$\Gamma_{\eta'\to\gamma\gamma}$	$\Gamma_{\sigma\to\pi\pi}$	$\Gamma_{\kappa\to K\pi}$	
Exp	0.52-0.54	4.2-4.5	400-700	~ 500	
Set 1	0.59	4.90	442	451	
Set 2	0.54	4.87	422	537	
	$\Gamma_{f_0\to\pi\pi}$	R_{f_0}	$\Gamma_{a_0\to\eta\pi}$	R_{a_0}	
Exp	10-100	3.8-4.7	50-100	1.2-1.6	
Set 1	11	4.3	37.4	2.4	
Set 2	20	4.0	52.0	1.2	

strange amplitudes [130, 131]. We have checked that turning on explicit isospin breaking ($m_{u0} \neq m_{d0}$) has negligible impact on this study. But it does turn on the $\pi^0 - \eta(\eta')$ mixing angles, ϵ and ϵ'. ϵ is found roughly consistent with experiments [132, 133], while ϵ' can be compared to future measurements.

6.3 Quark matter in general

Now we can employ the meson model to study quark matter. Quark matter can become energetically favorable due to the reduction of the constituent quark masses in the presence of the quark densities. QCD confinement on the other hand prevents net colour charge from appearing over large volumes. We suppose that these residual QCD effects on the energy per baryon are minor, similar to the way they are minor for the constituent quark model description of much of the QCD spectrum.

With the Yukawa coupling to quarks, $\mathcal{L}_y = -2g\bar{\psi}\Phi\psi$, the equations of motion for the spherically symmetric meson fields of interest are [134, 135]

$$\begin{aligned}\nabla^2\sigma_n(r) &= \frac{\partial V}{\partial \sigma_n} + g\sum_{i=u,d}\langle\bar{\psi}_i\psi_i\rangle,\\ \nabla^2\sigma_s(r) &= \frac{\partial V}{\partial \sigma_s} + \sqrt{2}g\langle\bar{\psi}_s\psi_s\rangle.\end{aligned} \tag{6.5}$$

$\nabla^2 = \frac{d^2}{dr^2} + \frac{2}{r}\frac{d}{dr}$ and there are $N_C = 3$ colours of quarks. The quark gas is described by the Fermi momentum for each flavour $p_{Fi} = p_F f_i^{1/3}$ where the quark fractions are $f_i = n_i/(N_C n_A)$, $p_F = (3\pi^2 n_A)^{1/3}$ and n_A is the baryon number density. The r dependence of these quantities is determined by the equations of hydrostatic equilibrium.

The forces driving the field values are from the scalar potential and the quark gas densities $\langle\bar{\psi}_i\psi_i\rangle = \frac{2N_C}{(2\pi)^3}\int_0^{p_{Fi}} d^3p\, m_i/\sqrt{p^2+m_i^2}$. In the interior the quark masses $m_{u,d}(r) = g\sigma_n(r) + m_{ud0}$ and $m_s(r) = \sqrt{2}g\sigma_s(r) + m_{s0}$ become smaller than the vacuum values m_{udv} and m_{sv}. The radius R of the bound state is defined where $\sigma_i(r)$ and $p_{Fi}(r)$ quickly approach their vacuum values.

Electrons play a minor role for any A, and they need not be contained when R becomes smaller than the electron Compton wavelength, i.e. $A \lesssim 10^7$ [52]. The quark, scalar and Coulomb energy densities are [52, 53]

$$\begin{aligned}\rho_\psi &= \sum_{i=u,d,s}\frac{2N_C}{(2\pi)^3}\int_0^{p_{Fi}} d^3p\sqrt{p^2+m_i^2},\\ \rho_\phi &= \Delta V + \frac{1}{2}\sum_{i=n,s}(\nabla\sigma_i)^2, \quad \rho_Z = \frac{1}{2}\sqrt{\alpha}V_C\, n_Z\,.\end{aligned} \tag{6.6}$$

ΔV is the potential energy w.r.t. the vacuum. $n_Z = \frac{2}{3}n_u - \frac{1}{3}(n_d+n_s)$ is the charge density, V_C is the electrostatic potential and $\alpha = 1/137$. The flavour composition of the quark gas and the radius R can be determined by minimizing the energy of the bound state $E = \int_0^R d^3r(\rho_\psi + \rho_\phi + \rho_Z)$ [60].

6.4 Quark matter in the bulk limit

At large A, finite size effects can be ignored and then both the meson fields and quark densities can be taken to be spatially constant. From (6.5) and for given $(p_F,\, f_i)$ the meson fields take values where the two forces balance. Among these force balancing points we can find the values of $(\bar{p}_F,\, \bar{f}_i)$ that minimize the energy per baryon $\varepsilon = (\rho_\psi + \rho_\phi + \rho_Z)/n_A$, with the uniform charge density $\rho_Z = \frac{4\pi}{5}\alpha R^2 n_Z^2$. The flavour composition $\bar{f}_i$ is driven to charge neutrality in the large A limit to avoid the dominance of ρ_Z.

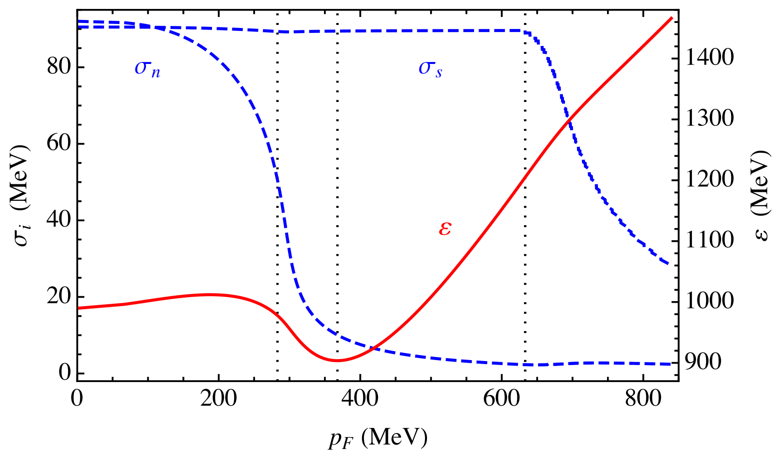

Figure 6.1: The field values σ_n, σ_s (blue dashed, left axis) and the energy per baryon number ε (red solid, right axis) in the bulk limit. The vertical lines denote the values of $p_F^{(n)}$, $\bar{p}_F$ and $p_F^{(s)}$.

Fig. 6.1 presents the field values and the energy per baryon as functions of p_F, after minimization w.r.t. the f_i, for the Set 1 benchmark with $m_{udv} = 330$ MeV (which implies $g = 3.55$ and $m_{sv} = 548$ MeV). The minimum energy per baryon is $\bar{\varepsilon} = 903.6$ (905.6) MeV at $\bar{p}_F = 367.8$ (368.5) MeV with $\bar{f}_s \approx 0$ for Set 1 (Set 2). For both sets udQM is the ground state of baryonic matter in the bulk.

As p_F increases from small values the fields move away from the vacuum along the least steep direction, which is a valley oriented close to the σ_n direction. σ_n drops rapidly at $p_F^{(n)}$ and at $\bar{p}_F$ the minimal energy per baryon $\bar{\varepsilon}$ is reached. $\bar{p}_F$ can be estimated by minimizing the relativistic quark and potential energies

$$\varepsilon \approx \frac{3}{4} N_C p_F \chi + 3\pi^2 \frac{\Delta V_n}{p_F^3} \tag{6.7}$$

w.r.t. p_F only. $\chi = \sum_i f_i^{4/3}$ and ΔV_n is the potential difference along the valley. This gives

$$\bar{\varepsilon} \approx N_C \bar{\chi} \bar{p}_F \tag{6.8}$$

and

$$\bar{p}_F^4 \approx \frac{12\pi^2 \Delta V_n}{(N_C \bar{\chi})}, \tag{6.9}$$

with only u and d quarks contributing in $\bar{\chi}$. f_s will finally turn on for $p_F \gtrsim p_F^{(s)}$ when it is energetically favorable to produce strange quarks (that may or may not be relativistic).

Our conclusion regarding udQM relies on the features that $p_F^{(n)} \lesssim \bar{p}_F \lesssim p_F^{(s)}$ and $\bar{\varepsilon} \lesssim 930$ MeV. These quantities can be estimated with a parameter scan of the meson model along with $m_{udv} \approx$ 330-360 MeV. The scan is constrained to be no more than about 10% outside the experimental ranges and with NDA coupling magnitudes less than 15. We find the ranges $p_F^{(n)} \approx 280$-305 MeV, $\bar{p}_F \approx 355$-395 MeV, $p_F^{(s)} \gtrsim 550$ MeV and $\bar{\varepsilon} \approx 875$-$960$ MeV. As an example of sensitivity to the lightest meson masses, Fig. 6.2 shows a $\bar{\varepsilon}$ vs m_σ projection of the parameter space where we see that realistic values of m_σ favor stable udQM.

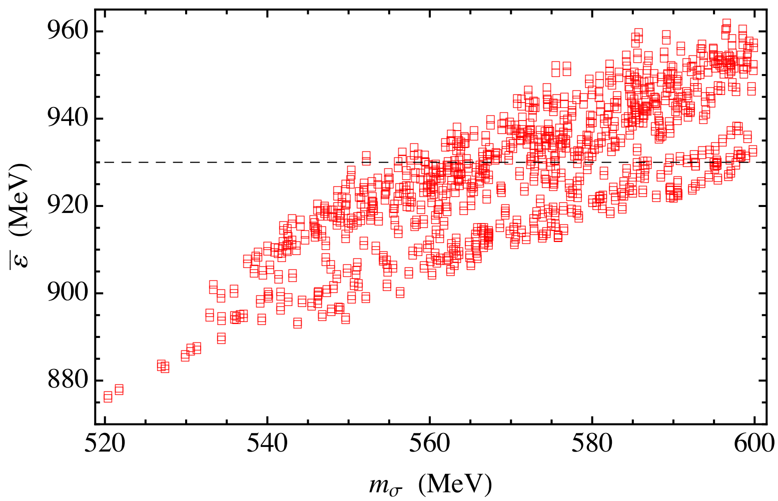

Figure 6.2: $\bar{\varepsilon}$ vs m_σ from the parameter scan.

6.5 Determination of $A_{\rm min}$ for udQM

At smaller A we need to include finite size effects and the Coulomb energy contribution. We adopt the approximation that the values of p_F and f_i are constants, nonvanishing only for $r < R$, which has been found to give a good approximation for the binding energy [196]. For each A we solve for the profile of the field $\sigma_n(r)$ moving along the valley using (6.5) and find the configuration, including the radius R, that minimizes the energy E.

For the Set 1 benchmark with $m_{udv} = 330$ MeV, the numerical solutions of the electric charge and the minimal energy per baryon as functions of A are presented by blue dots in Fig. 6.3 and Fig. 6.4 respectively. It turns out that the electric charge of udQM can be well estimated by simply minimizing the quark and Coulomb energies of the relativistic u, d gas with charge $Z = N_C A(\bar{f}_u(A) - 1/3)$, as shown by the blue line in Fig. 6.3. We find $Z \approx \frac{0.86}{\alpha N_C} A^{1/3}$ for large A. The shaded region denotes configurations that are stable against decays into ordinary nuclei.

Fig. 6.4 shows that the surface effect increases the energy and destabilizes the udQM configuration for $A < A_{\rm min}$. For Set 1 (Set 2) $A_{\rm min} \approx 320$ (450) is large enough to prevent normal nuclei from decaying to udQM. The numerical results of $\bar{\varepsilon}(A)$ can be well

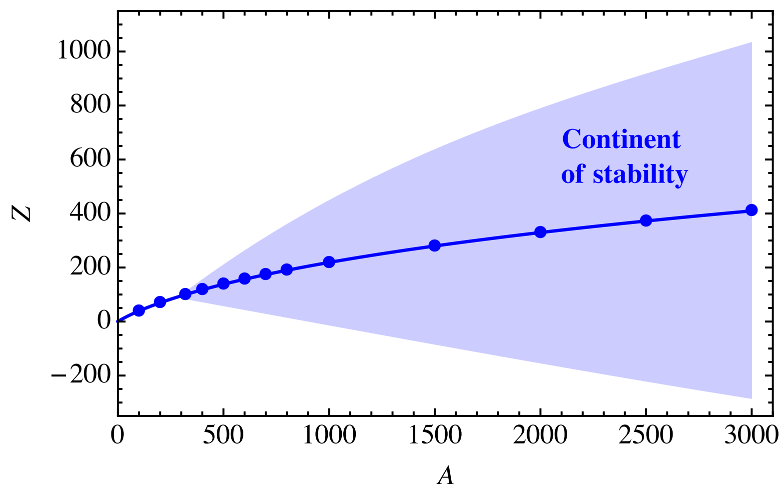

Figure 6.3: The electric charge of udQM: full result (blue dots) and the bulk approximation (blue line).

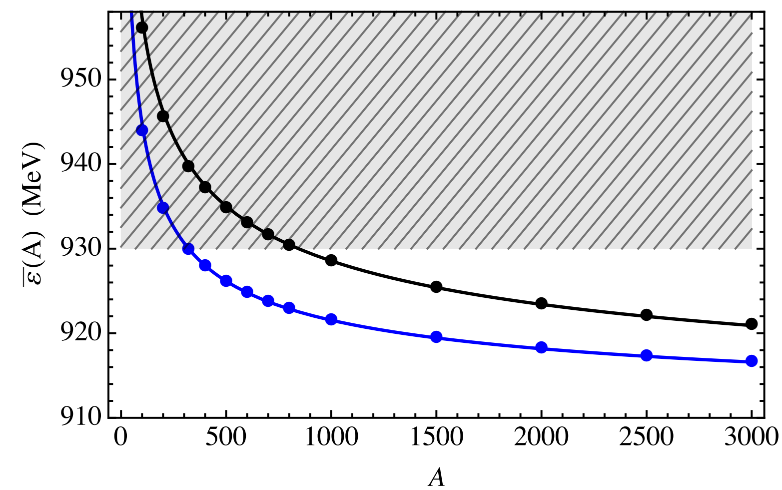

Figure 6.4: The minimal energy per baryon $\bar{\varepsilon}(A)$ for udQM (lower), compared to the charge neutral configuration (upper).

approximated by incorporating a surface tension term $4\pi R^2\Sigma$ into the bulk analysis:

$$\bar{\varepsilon}(A) \approx \bar{\varepsilon} + 46\,\frac{\Sigma}{\bar{p}_F^2 A^{1/3}} + 0.31\,\frac{\alpha\, Z^2 \bar{p}_F}{A^{4/3}}. \tag{6.10}$$

Here $\bar{\varepsilon}$ and $\bar{p}_F$ reflect the value of $\bar{\chi}$ for given Z and A. From fits from the two Sets and other examples we find that $\Sigma \approx (91\,\mathrm{MeV})^3$, and that it varies less than $\bar{\varepsilon}$ as displayed in Fig. 6.2. So as long as $\bar{\varepsilon} \gtrsim 903\,\mathrm{MeV}$ we can expect that $A_{\mathrm{min}} \gtrsim 300$. The surface term dominates the Coulomb term for all A, and so the analog of fission that ends the periodic table does not occur for udQM.

6.6 Discussion

If $A_{\min}$ for udQM is close to the lower limit, it raises the hope to produce this new form of stable matter by the fusion of heavy elements. With no strangeness to produce this may be an easier task than producing SQM. Due to the shape of the curve in Fig. 6.3, there would still be the issue of supplying sufficient neutrons in the reaction to produce udQM, as in the attempts to produce normal superheavy nuclei in the hypothetical "island of stability" around $A \approx 300$ [136]. udQM may instead provide a new "continent of stability" as shown in Fig. 6.3, in which the largest values of Z/A are of interest for production and subsequent decay to the most stable configuration. As with SQM, the further injection of neutrons (or heavy ions [137, 138]) can cause the piece of udQM to grow with the release of an indefinite amount of energy [139].

Neutron stars could convert to ud quark stars. Due to the potential barrier generated by the surface effects, the limiting process for the conversion of a neutron star is the nucleation of a bubble of quark matter initially having the same local flavour composition as the neutron star, via a quantum or thermal tunneling process [140]. There is then a subsequent weak decay to the stable state, SQM or udQM, as the bubble grows. The barrier for conversion leads to the possibility that there can co-exist both neutron stars and quark stars [141]. In comparison to SQM, udQM predicts a smaller $\bar{\rho} = 4\Delta V_n$ given the same $\bar{\varepsilon}$. So ud quark stars allow a larger maximum mass, which is of interest for pulsars with $M \sim 2M_\odot$ [73, 74]. The possible superconducting nature of quark matter in stars may have interesting implications, more so for its transport rather than bulk properties [49].

Chapter 7

IR: Probing udQM via Gravitational Waves

As previous chapter has discussed, udQM can be the ground state of matter for baryon number $A > A_{\min}$ with $A_{\min} \gtrsim 300$. In this chapter, we explore the ud quark stars (udQSs) that are composed of stable udQM, in the context of the two-families scenario in which udQSs and hadronic stars (HSs) can co-exist. Here we show that the requirements of $A_{\min} \gtrsim 300$ and the most-massive compact star observed being udQS together put stringent constraints on the allowed parameter space of udQSs. Then we study the related gravitational-wave probe of the tidal deformability in binary star mergers, including the udQS-udQS and udQS-HS cases. The obtained values of the tidal deformability at 1.4 solar mass and the average tidal deformability are all in good compatibility with the experimental constraints of GW170817/AT2017gfo. This study points to a new possible interpretation of the GW170817 binary merger event, where udQS may be at least one component of the binary system detected. The text in this chapter is reproduced from [20].

7.1 Introduction

In the conventional picture of nuclear physics, quarks are confined in the state of hadrons. However, it is also possible that quark matter, a state consisting of deconfined quarks, exists. Bodmer [54], Witten [55] and Terazawa [56] proposed the hypothesis that quark matter with comparable numbers of u, d, s quarks, also called strange quark matter (SQM), might be the ground state of baryonic matter. However, this hypothesis is based on the bag model that cannot adequately model the flavor-dependent feedback of the quark gas on the QCD vacuum. Improved models have shown that quark matter with u, d quarks (udQM) only is more stable than SQM [57, 51, 19, 142], but with the common conclusion that neither is more stable than ordinary nuclei. In a recent study [19], with a phenomenological quark-meson model that can give good fits to all the masses and decay widths of the light meson nonets and can account for the flavor-dependent feedback [143, 144], the authors demonstrated that udQM can be more stable than the ordinary nuclear matter and SQM when the baryon number A is sufficiently large above $A_{\rm min} \gtrsim 300$. The absolute stability of udQM is tested to be robust within 10% departures of the experimental data. The large $A_{\rm min}$ ensures the stability of ordinary nuclei in the periodic table, which also results in a large positive charge. Recently, a collider search for such high-electric-charge objects was attempted using LHC data [145].

One can also look for the evidence of udQM from the gravitational-wave detections experiments. The binary merger of compact stars produces strong gravitational wave fields, the waveforms of which encode the information of the tidal deformation that is sensitive to the matter equation of state (EOS). In general, stars with stiff EOSs can be tidally deformed easily due to their large radii.

The GW170817 event detected by LIGO [146] is the first confirmed merger event of compact stars. Together with the subsequent detection of the electromagnetic counterpart, GRB 170817A and AT2017gfo [147], they inspired a lot of studies that greatly move our understanding of nuclear matter forward [148, 149, 150, 151, 152, 153, 154, 156, 76, 157, 158, 159, 160, 155]. The initial analysis [146] determines the chirp mass of the binary is determined to be $M_c = 1.188\, M_\odot$. For the low spin case, the binary mass ratio $q = M_2/M_1$ is constrained to the range $q = 0.7 - 1.0$. Upper bounds have been placed on the tidal deformability at 1.4 solar mass $\Lambda(1.4M_\odot) \lesssim 800$, and on the average tidal deformability $\tilde{\Lambda} \leq 800$ at 90% confidence level. Later, an improved LIGO analysis [161] gives $M_c = 1.186^{+0.001}_{-0.001}\, M_\odot$, and a 90% highest posterior density inverval of $\tilde{\Lambda} = 300^{+420}_{-230}$ with $q = 0.73 - 1.00$ for the low spin prior. Lower bounds have been placed from AT2017gfo with kilonova models [149, 151, 150]. However, to the author's knowledge, the more strict lower bounds obtained in such analysis, including $\Lambda(1.4M_\odot) \gtrsim 200$ [150] and $\tilde{\Lambda} \gtrsim 242$ [151], are all assuming neutron star EOS. Therefore, we will not use them to constrain our study of quark stars here.

Conventionally, binary mergers are studied in the one-family scenario where it is assumed that all compact stars are within one family of hadronic matter EOS [146, 152, 153, 154, 156]. However, the discovery of pulsars with large masses above $2\, M_\odot$ [73, 74, 75] ruled out a large number of soft EOSs that were expected with the presence of hyperons and Δ resonances in the interiors. Therefore, it is natural to expect that the stars with masses above $2\, M_\odot$ and large radii are actually quark stars (QSs), and most of the ones with small masses and small radii are the hadronic stars (HSs). This possibility is the so-called "two-families" scenario, which is based on the hypothesis that absolutely stable quark matter (either SQM or udQM) exists, and that the hadronic stars can coexist with quark stars [162]. The binary merger in the two-families scenario includes three cases: HS-HS [155], HS-QS [156] and QS-QS [163]. Alternatively, dropping the hypothesis that quark matter is the ground state gives the twin-stars scenario [156, 159, 160], where quark matter only appears in the interiors of hybrid stars.

Several things make ud quark stars (udQSs), which are composed of udQM, very distinct compared to the strange quark stars (SQSs) that are composed of SQM. Firstly, udQSs can satisfy $2\,M_{\odot}$ constraint more easily than HSs and SQSs [19, 164] due to the non-hyperonic composition and the small effective bag constant. Secondly, the co-existence of HSs and QSs requires that the conversion of hadronic matter to quark matter is neither too fast nor too slow compared to the age of our universe. In contrast to the co-existence study for SQSs where the conversion requires the presence of hyperons which only emerge above 1.5 solar mass, the conversion regarding udQSs can happen at a smaller mass range since no hyperonic composition is needed. Therefore, it is possible that udQSs can co-exist with HSs even at the small mass range below $1.5M_{\odot}$. This reasoning raises the possibility for GW170817 being a udQS-udQS merger or a udQS-HS merger despite the smallness of the chirp mass $1.186M_{\odot}$ and high mass ratio $q = 0.73-1.00$. Besides, the possibility of QS-QS case sometimes is disfavoured for GW170817/AT2017gfo because of the kilonova observation of nuclear radioactive decay [165]. However, it is possible that the udQM ejected is quickly destabilized by the finite-size effects and converts into ordinary or heavy nuclei. The conversion is far more rapid for udQM than for SQM, due to a much larger $A_{\rm min}$ and the non-strange composition so that there is no need to involve extra weak interactions to convert away strangeness. Note that the radii constraints derived from GW170817 are mostly for hadronic EOSs in the context of the one-family scenario [152, 153, 154], so that they have no much relevance to the udQSs in the two-families scenario we are discussing here.

Motivated by these considerations, we explore the properties of udQSs and the related gravitational-wave probe in the two-families scenario, including the binary merger cases udQS-udQS and udQS-HS. We will discuss the related compatibility and constraints from GW170817. Note that we ignore the discussion of the HS-HS case since this possibility is not directly related to the study of quark stars and is disfavoured to some extent for GW170817 based on the consideration of prompt collapse [155].

7.2 Properties of udQSs

The EOS of udQM can be well approximated by the simple form $p = 1/3\,(\rho - \rho_s)$, where ρ_s is the finite density at the surface. For the EOS of SQM, the coefficient 1/3 is modified by the strange quark mass effect, with the ρ_s value also being different. In the region of interest for udQM, we can take the relativistic limit where energy per baryon number in the bulk limit takes the form: $E/A = \rho/n_A \approx (\chi N_C p_F^4/4\pi^2 + B_{\rm eff})/n_A = 3/4\,N_C p_F \chi + 3\pi^2 B_{\rm eff}/p_F^3$ [19], where $N_C = 3$ is the color factor and $\chi = \sum_i f_i^{4/3}$ is the flavour factor, with the fraction $f_u = 1/3 = 1/2\,f_d$ for udQM. The effective Fermi momentum is $p_F = (3\pi^2 n_A)^{1/3}$. $B_{\rm eff}$ is the effective bag constant that accounts for the QCD vacuum contribution. Note that in this udQM study, we can approximate $B_{\rm eff}$ as an effective constant since its dependence on flavor and density only causes a substantial effect when strangeness turns on at very large density [19, 57, 51]. Minimizing the energy per baryon number with respects to p_F for fixed flavour composition gives

$$\frac{E}{A} = 3\sqrt{2\pi}\left(\chi^3 B_{\rm eff}\right)^{1/4}, \tag{7.1}$$

at which $p = 0$, $\rho = \rho_s = 4B_{\rm eff}$. Eq. (7.1) matches the exact numerical result of the phenomenological meson model [19] extremely well with a mere error $\sim 0.3\%$ due to a tiny $u(d)$ quark mass. It was shown in [19, 57, 51] that $B_{\rm eff}$ has a smaller value in the two-flavour case than in the three-flavour case, so that udQM is more stable than SQM in the bulk limit. Absolute stability of udQM in the bulk limit implies $E/A \lesssim 930\,\text{MeV}$, which corresponds to

$$B_{\rm eff} \lesssim 56.8\,\text{MeV/fm}^3. \tag{7.2}$$

from Eq. (7.1). In general, a larger E/A or $B_{\rm eff}$ gives a larger $A_{\rm min}$. The stability of ordinary nuclei against udQM requires $A_{\rm min} \gtrsim 300$, which translates to $E/A \gtrsim 903\,\text{MeV}$ or

$$B_{\rm eff} \gtrsim 50\,\text{MeV/fm}^3 \tag{7.3}$$

for the quark-meson model that matches the low energy phenomenology [19]. This quark-meson model also results in a quark-vacuum surface tension $\sigma \approx (91\,\text{MeV})^3$ that is robust against parameter variations.

The linear feature of udQM EOS makes it possible to perform a dimensionless rescaling on parameters [83, 84]

$$\bar\rho = \frac{\rho}{4\,B_{\rm eff}},\ \bar p = \frac{p}{4\,B_{\rm eff}},\ \bar r = r\sqrt{4\,B_{\rm eff}},\ \bar m = m\sqrt{4\,B_{\rm eff}}, \tag{7.4}$$

which enter the TOV equation [71, 70]

$$\begin{aligned} \frac{dp(r)}{dr} &= -\frac{[m(r)+4\pi r^3 p(r)]\,[\rho(r)+p(r)]}{r(r-2m(r))}\,, \\ \frac{dm(r)}{dr} &= 4\pi\rho(r)r^2, \end{aligned} \tag{7.5}$$

so that the rescaled solution is also dimensionless, and thus is independent of any specific value of B_{eff}. The TOV solution with a specific B_{eff} value can be obtained directly from rescaling the dimensionless solution back with Eq. (7.4). Solving the rescaled TOV equation with udQM EOS gives the dimensionless result shown in Figure 7.1, with the maximum rescaled mass at $(\bar{M}, \bar{R}) = (M\sqrt{4\,B_{\text{eff}}}, R\sqrt{4\,B_{\text{eff}}}) = (0.0517, 0.191)$, mapping to $M_{\text{max}} \approx 15.174/\sqrt{B_{\text{eff}}}\ M_\odot$, $R_{\text{Mmax}} \approx 82.79/\sqrt{B_{\text{eff}}}$ km. Therefore, the requirement that udQS has maximum mass not smaller than the recently observed most-massive compact star J0740+6620 ($M \approx 2.14^{+0.10}_{-0.09}\,M_\odot$) [75] implies

$$B_{\text{eff}} \lesssim 50.3^{+4.5}_{-4.4}\,\text{MeV/fm}^3, \tag{7.6}$$

which constrains more strictly than what Eq. (7.2) imposes. Interestingly, the central value of the upper bound Eq. (7.6) is very close to the lower bound Eq. (7.3) at the critical value $B_c \approx 50\,\text{MeV/fm}^3$. To be more conservative, we can take 10% departures considering the theoretical and experimental uncertainties [60, 62, 63, 64, 65, 66, 67, 75], so that the allowed window of B_{eff} for udQS is:

$$\{B_{ud\text{QS}}\} \approx [45,\ 55]\,\text{MeV/fm}^3 \tag{7.7}$$

with central value $B_c \approx 50\,\text{MeV/fm}^3$. The corresponding $M-R$ solution is shown in Figure 7.2.

Note that some SQS studies [156, 163, 80] exploited similar small B_{eff} to have maximum masses above $2\,M_\odot$, but the smallness is not natural considering the appearance of strangeness, and a large perturbative QCD (pQCD) effect or a color-superconducting phase has to be included to guarantee the stability.

The response of compact stars to external disturbance is characterized by the Love

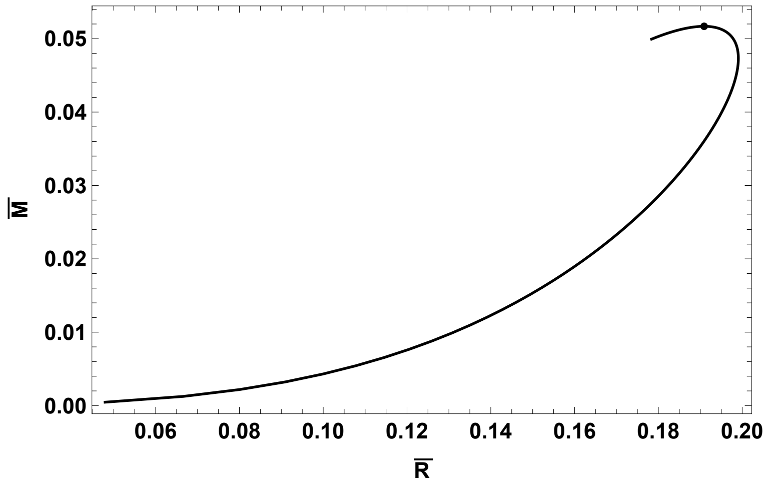

Figure 7.1: $\bar{M}$-$\bar{R}$ of udQS. The black dot at $(\bar{M}, \bar{R})$= $(0.0517, 0.191)$ denotes the maximum mass configuration.

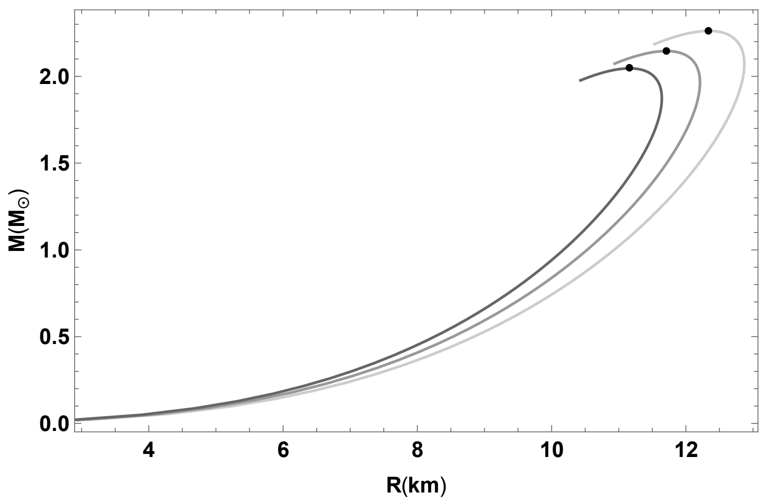

Figure 7.2: M-R of udQSs. Lines with darker color are with larger effective bag constant $B_{\rm eff}$, which samples $(45, 50, 55)\,{\rm MeV/fm^3}$ respectively. The black dots denote the maximum mass location.

number k_2 [166, 167, 168, 169],

$$\begin{aligned} k_2 = &\frac{8C^5}{5}(1-2C)^2[2+2C(y_R-1)-y_R] \\ &\times \{2C[6-3y_R+3C(5y_R-8)]+4C^3[13-11y_R \\ &+C(3y_R-2)+2C^2(1+y_R)] \\ &+3(1-2C)^2[2-y_R+2C(y_R-1)]\log(1-2C)\}^{-1}\ . \end{aligned} \tag{7.8}$$

Here $C = M/R = C(\bar{M})$. And y_R is $y(r)$ evaluated at the surface, which can be obtained by solving the following equation [169]:

$$\begin{aligned} & r y'(r) + y(r)^2 + r^2 Q(r) \\ & + y(r) e^{\lambda(r)} \left[1 + 4\pi r^2 (p(r) - \rho(r))\right] = 0\,, \end{aligned} \tag{7.9}$$

with boundary condition $y(0) = 2$. Here

$$\begin{aligned} Q(r) = & \, 4\pi e^{\lambda(r)} (5\rho(r) + 9p(r) + \frac{\rho(r) + p(r)}{c_s^2(r)}) \\ & - 6\frac{e^{\lambda(r)}}{r^2} - (\nu'(r))^2\,, \end{aligned} \tag{7.10}$$

and

$$e^{\lambda(r)} = \left[1 - \frac{2m(r)}{r}\right]^{-1}, \; \nu'(r) = 2e^{\lambda(r)} \frac{m(r) + 4\pi p(r) r^3}{r^2}. \tag{7.11}$$

$c_s^2(r) \equiv dp/d\rho$ denotes the sound speed squared. For stars with a finite surface density like quark stars, a matching condition should be used at the boundary $y_R^{\rm ext} = y_R^{\rm int} - 4\pi R^3 \rho_s / M$ [170]. Solving Eq. (7.9) with the $\rho(r)$ and $p(r)$ obtained from Eq. (7.5), one obtains the function $k_2(C)$. The dimensionless tidal deformability $\Lambda = 2k_2/(3C^5)$ as a function of mass $\bar{M}$ is thus obtained accordingly. The result is shown in Fig. 7.3.

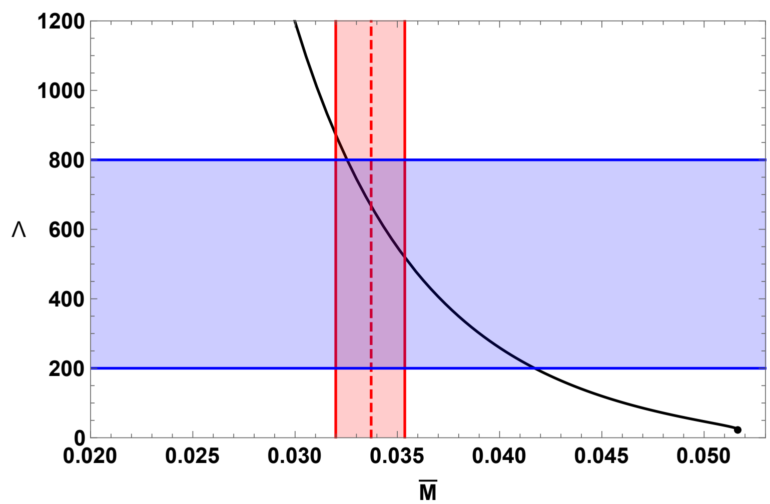

Figure 7.3: The tidal deformability Λ vs rescaled star mass $\bar{M}$ for udQSs. For $\bar{M}$ with $M = 1.4 M_\odot$, red band represents the region with $B_{\rm eff} \in \{B_{ud{\rm QS}}\}$, and red dashed line is with $B_{\rm eff} = B_{\rm c}$. Blue band is the GW170817 constraints on $\Lambda(1.4M_\odot)$ [146].

We see from Fig. 7.3 that for $M = 1.4\,M_\odot$ and $B_{\rm eff} \in \{B_{ud{\rm QS}}\}$, one has $\bar{M} = M\sqrt{4B_{\rm eff}} \in [0.032, 0.035]$, as the red band in Figure 7.3 represents. Mapping this range to Fig. 7.3 gives $\Lambda(1.4M_\odot) \in [530, 857]$. And $\Lambda(1.4M_\odot) \approx 670$ for $B_{\rm eff} = B_c$. We see that these results are well compatible with the GW170817 constraint $\Lambda(1.4M_\odot) \lesssim 800$ [146]. In particular, the point where $\Lambda(1.4M_\odot)$ reaches the upper bound $\Lambda(1.4M_\odot) \sim 800$ puts a more stringent lower bound that $B_{ud\mathrm{QS}} \gtrsim 47.9\,\mathrm{MeV/fm^3}$. We also see that the result is not sensitive to the possible uncertainties related to the lower bound of $\Lambda(1.4M_\odot)$ constraint.

7.3 Binary Merger in the Two-Families Scenario

The average tidal deformability of a binary system is defined as:

$$\tilde{\Lambda} = \frac{16}{13}\frac{(1+12q)}{(1+q)^5}\Lambda(M_1) + \frac{16}{13}\frac{q^4(12+q)}{(1+q)^5}\Lambda(M_2), \tag{7.12}$$

where M_1 and M_2 are the masses of the binary components. And $q = M_2/M_1$, with M_2 being the smaller mass so that $0 < q \leq 1$. Then for any given chirp mass $M_c = (M_1M_2)^{3/5}/(M_1+M_2)^{1/5}$, one has $M_2 = (q^2(q+1))^{1/5}M_c$ and $M_1 = ((1+q)/q^3)^{1/5}M_c$.

7.3.1 udQS-udQS Merger

In this case, the average tidal deformability can be expressed as a function of the rescaled mass parameter $\bar{M} = M\sqrt{4B_{\mathrm{eff}}}$:

$$\tilde{\Lambda} = \frac{16}{13}\frac{(1+12q)}{(1+q)^5}\Lambda(\bar{M}_1) + \frac{16}{13}\frac{q^4(12+q)}{(1+q)^5}\Lambda(\bar{M}_2). \tag{7.13}$$

Substituting the $\Lambda(\bar{M})$ obtained previously into the formula above, we get the results shown in Fig. 7.4. Note that in this figure, the lower end of each curve is determined by requiring each component of the binary system not to exceed its maximum mass. The $\bar{M}_c$ value of each end is negatively correlated with the q value, since for a given M_c the less symmetric system has a larger component mass which can exceed their maximum mass more easily. The general shape of the figure matches our qualitative expectation. For given $\bar{M}_c$, a smaller mass ratio q maps to a smaller $\tilde{\Lambda}$. Besides, for given q, a larger rescaled mass $\bar{M}_c = M_c\sqrt{4B_{\mathrm{eff}}}$ corresponds to a smaller $\tilde{\Lambda}$. These features are all due to the general fact that quark stars with larger masses have larger compactness, and thus are less likely to be tidally deformed.

As Fig. 7.4 shows, for GW170817 in which $M_c = 1.186\,M_\odot$, the constraint $\tilde{\Lambda} = 300^{+420}_{-230}$ [161] translates to $0.4 \lesssim q \lesssim 1$ for $B_{\mathrm{eff}} \in \{B_{ud\mathrm{QS}}\}$, and especially to $q = 0.74$ for $B_{\mathrm{eff}} = B_c = 50$ MeV/fm^3, all of which are compatible with the GW170817 constraint $q = 0.73 - 1.00$ [146]. We see that $q \gtrsim 0.73$ and $\tilde{\Lambda} \lesssim 720$ put a more stringent lower bound that $B_{ud\mathrm{QS}} \gtrsim 49.5\,\mathrm{MeV/fm^3}$. We also see that $B_{ud\mathrm{QS}}$ is not constrained much by the lower bound of $\tilde{\Lambda}$.

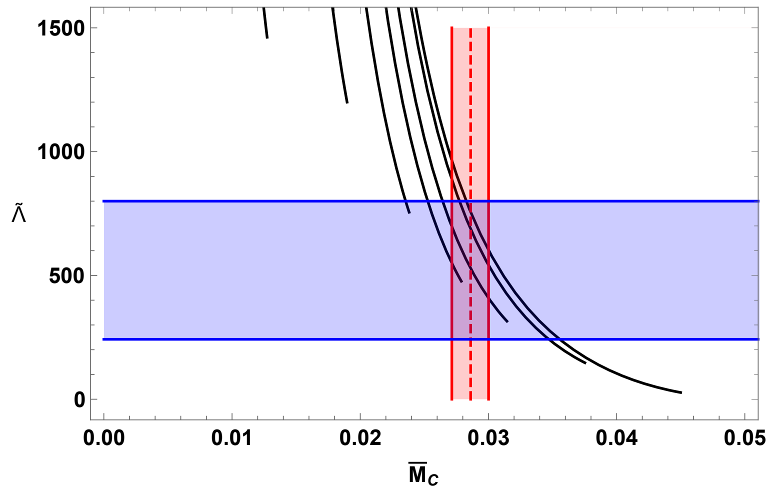

Figure 7.4: The average tidal deformability $\tilde{\Lambda}$ vs the rescaled chirp mass $\bar{M}_c$ for the udQS-udQS merger case. Black curves are with $q = M_2/M_1 = (0.1, 0.2, 0.3, 0.4, 0.5, 0.7, 1)$ from left to right, respectively. For the GW170817 event in which $M_c = 1.186 M_\odot$, the red band represents the region of $\bar{M}_c$ with $B_{\rm eff} \in \{B_{ud\rm QS}\}$, and the red dashed line is with $B_{\rm eff} = B_c$. The blue band is the GW170817 constraint on $\tilde{\Lambda}$ [161].

7.3.2 udQS-HS Merger

For the udQS-HS merger case, we need the information of the hadronic matter EOS, which has large uncertainties in the intermediate-density region. Based on nuclear physics alone, the EOS should match the low density many-body calculation and high density pQCD result [171]. Here we use three benchmarks of hadron matter EOSs, SLy [172, 173] Bsk19 and Bsk21 [174] that have unified representations from low density to high density. Bsk19 is an example of soft EOSs. HSs with Bsk19 have maximum mass $M_{\rm max} = 1.86\,M_\odot < 2\,M_\odot$ and $R_{1.4 M_\odot} = 10.74\,{\rm km} < 11\,{\rm km}$. The feature of small masses and small radii is preferred for the typical HSs branch of the two-families scenario. For illustration, we also show benchmarks of a hard EOS (Bsk21) with $M_{\rm max} = 2.27\,M_\odot$, $R_{1.4\,M_\odot} = 12.57\,{\rm km}$, and a moderate one (SLy) with $M_{\rm max} = 2.05\,M_\odot$, $R_{1.4 M_\odot} = 11.3\,{\rm km}$. With Eq. (7.12), the $\Lambda(M)$ results of udQS, and the HS EOS benchmarks, we obtain the average tidal deformability $\tilde{\Lambda}$ of the udQS-HS system, as shown in Fig. 7.5.

We see from Fig. 7.5 that the order of $\tilde{\Lambda}$ for different HS EOSs matches the expectation from the general rule that a HS with a stiffer EOS or a QS with a smaller effective bag constant has a larger radius, and thus has larger deformability. Lines with different hadronic EOSs tend to merge at lower q as $\tilde{\Lambda}$ gets dominated by the contribution of large-mass quark stars. We see a good compatibility with current GW170817 constraint $\tilde{\Lambda} = 300^{+420}_{-230}$ when $q = 0.73 - 1.00$, except for an exclusion of the stiffest hadronic EOS (Bsk21).

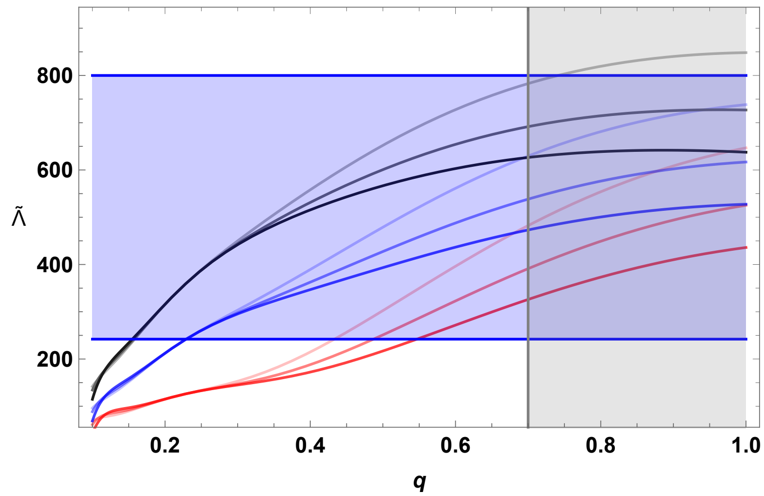

Figure 7.5: The average tidal deformability $\tilde{\Lambda}$ vs $q = M_2/M_1$ for the udQS-HS merger case, with M_2 being the mass of hadronic star and $M_c = 1.186M_\odot$ for the GW170817 event. For HS EOS, SLy (blue), Bsk19 (red), Bsk21 (black) are used. For udQS EOS, lines with darker color are with larger $B_{\rm eff}$, which samples $(45, 50, 55)\,\mathrm{MeV/fm^3} \in \{B_{ud\mathrm{QS}}\}$ respectively. The blue band and grey band are the GW170817 constraints on $\tilde{\Lambda}$ and q respectively [161].

7.4 Conclusions

We have discussed the distinct properties that make udQSs good candidates for the two-families scenario in which hadronic stars can co-exist with quark stars. We have shown that the requirements of $A_{\rm min} \gtrsim 300$ and $M_{\rm max} \gtrsim 2.14\,M_\odot$ together stringently constrain the effective bag constant of udQSs to $B_{\rm eff} \approx 50\,\mathrm{MeV/fm^3}$. A 10% relaxation that accounts for the possible uncertainties gives the conservative range $B_{ud\mathrm{QS}} \in [45,\,55]\,\mathrm{MeV/fm^3}$. Then we studied the related gravitational-wave probe of tidal deformability of binary star mergers including the udQS-udQS and udQS-HS cases. For the udQS-udQS case, the upper bound of tidal deformability and the binary mass ratio of GW170817 further confine the allowed parameter space to $B_{ud\mathrm{QS}} \in [49.5,\,55]\,\mathrm{MeV/fm^3}$. Also with the dimensionless rescaling method used, the analysis can be straightforwardly generalized to arbitrary binary chirp mass and effective bag constant for current and future gravitational-wave events. The udQS-HS case is also well compatible with the GW170817 constraints. These point to a new possibility that GW170817 can be identified as either a udQS-udQS merger or a udQS-HS merger event.

Note Added: As we were finalizing this work, we became aware of the new paper [175] around the same time. With a special version of the NJL model, their paper has some discussions on the $\Lambda(1.4M_\odot)$ of non-strange quark stars for the low spin case of GW170817, and they also found that $\Lambda(1.4M_\odot)$ can match the experimental constraints in certain parameter space. However, they neglected the study of the two-families scenario and the corresponding average tidal deformability $\tilde{\Lambda}$. And they only explored the parameter space in which udQM is more stable than SQM, with the parameter space where udQM is even more stable than nuclear matter remaining uncertain in their model.

Chapter 8

Conclusions and Future Prospects

In this thesis, we have explored the new possibilities of the Standard Model and beyond.

Towards the high energy scale, the asymptotically free and asymptotically safe extensions of the Standard Model are explored in Chapter 4 and Chapter 5 respectively. An exhaustive search on the asymptotically free extensions with semi-simple gauge groups has been completed, with the parameter space of stable UV fixed points being identified. Using the large number-of-flavour techniques, we constructed the asymptotically safe extensions by adding gauged vector-like fermions. These works resurrected the interest in these topics, motivating many following studies. For the complete asymptotic freedom program, in particular, detailed construction in the context of $SO(N)$ GUT with a UV-complete quadratic gravity sector was done in [176, 177], but with the generation of the electroweak scale remaining to be addressed. For the large-N_F asymptotically safe program, some more complete studies of the quartic coupling beta function showed that the quartic coupling blows up when abelian gauge coupling reaches its UV fixed point [178, 179]. Also, Antipin et al. [181] showed that for the abelian gauge group the mass anomalous dimension γ_m blows up at the abelian UV fixed point, violating the unitarity bound $\gamma_m \leq 2$. These deficiencies motivate people to extend the study to the semi-simple GUT [180], but the possibility of constructing an asymptotically safe extension of a simple-group GUT remains open.

At the low energy scale, with a phenomenological quark-meson model as an effective description of QCD dynamics, we showed in Chapter 6 that quark matter composed of u, d quarks only is more stable than both strange quark matter and normal nuclei for baryon number $A \gtrsim 300$ beyond the periodic table. Finally, in Chapter 7, we discussed the distinct gravitational properties of udQM, and the probe of udQM via gravitational waves. In particular, we pointed out a new possible interpretation of the GW170817 binary merger event, where ud quark star may be at least one component of the binary system detected.

Our very first publication of udQM [19] has attracted media reports [186]. Apart from the importance on understanding the fundamental nature, the study also leads to great potential impacts on human life for an old idea that using quark matter as a new source of energy. Recently, a search for high-electric-charge objects like udQM is attempted in collider using LHC data [145]. There are some remaining important questions to be addressed:

1. Can ud quark stars (udQSs), which are composed of udQM, co-exist with neutron stars considering the transition rate [183] from nuclear matter to udQM?

2. How does the perturbative QCD correction and the colour-superconductivity phase affect the properties of udQM?

3. Can udQM be a viable candidate for dark matter [184]?

4. How do we incorporate udQM in cosmological settings (QCD first-order phase transition) [55]?

5. How do we identify and extend those searches for SQM that are most relevant for udQM? Especially, how can we build viable fusion experiments so that we can produce udQM on earth [185]? And how can udQM be probed in cosmic rays [187]?

The works related to the first and second questions are explored in substantial progress, but they are not included in this thesis due to time constraints. The other questions remain to be studied in the future.

Appendices

Appendix A

The Generalized Meson Model

In this chapter, we elaborate the generalized $SU(3)_L \times SU(3)_R$ linear sigma model used in Chapter 6. This model includes an extended sector of explicit chiral symmetry breaking terms so that numerical fits of current experimental constraints on the masses and decay widths are accomplished. Once the isospin breaking effect is included, this model predicts the right value of the isospin-breaking parameter ϵ within the experimental uncertainties. The work is through my collaboration with Bob Holdom and Jing Ren.

A.1 Introduction

QCD has the approximate chiral symmetry $SU(3)_L \times SU(3)_R$ due to the smallness of u, d, s current quark masses compared to that of the other flavours. Effective models incorporating this chiral symmetry have achieved huge successes in describing the low-lying QCD spectrum, among which the linear sigma model is widely used for its simplicity and generality.

In the sense of simplicity, the MIT bag model is also simple and elegant. It introduces a bag constant to account for all the non-perturbative effects of QCD vacuum. But it fails on the generality. The chiral symmetry is badly broken at starting point, and thus it is hard to model light pseudo-scalar mesons. Besides, it suffers from the failure in describing finite-temperature QCD. Moreover, it neglects many important physics like the density-dependent and flavour-dependent feedback of the quarks on the QCD vacuum. In contrast, the linear sigma model can accommodate these aspects naturally.

The Lagrangian for the minimal linear sigma model [10, 36, 38] is:

$$\mathcal{L}_m = \mathrm{Tr}\left(\partial_\mu \Phi^\dagger \partial^\mu \Phi\right) - V(\Phi) \tag{A.1}$$

with the scalar potential

$$V(\Phi) = V_{\rm inv}(\Phi) + V_b(\Phi), \tag{A.2}$$

where $V_{\rm inv}$ is the chiral invariant part:

$$V_{\rm inv} = \lambda_1 \left(\mathrm{Tr}\ \Phi^\dagger\Phi\right)^2 + \lambda_2\, \mathrm{Tr}\left(\Phi^\dagger\Phi\Phi^\dagger\Phi\right) + m^2\, \mathrm{Tr}\left(\Phi^\dagger\Phi\right) + c\left(\det\Phi + \det\Phi^\dagger\right).$$

The c term is the t'Hooft term that signals $U(1)_A$ breaking. And V_b is the explicit breaking part. We denotes

$$\Phi = T_a\Phi_a = T_a\left(\sigma_a + i\pi_a\right), \tag{A.3}$$

where $T_a = \lambda_a/2$ with $a = 0,\ldots,8$ are the nine generators of the $U(3)$, with the λ_a the usual eight Gell-Mann matrices and $\lambda_0 = \sqrt{\frac{2}{3}}\,\mathbf{1}$. The generators T_a are normalized so that $\mathrm{Tr}(T_aT_b) = \delta_{ab}/2$ and obey the $U(3)$ algebra $[T_a, T_b] = if_{abc}T_c$ and $\{T_a, T_b\} = d_{abc}T_c$ respectively with the corresponding standard symmetric d_{abc} and antisymmetric f_{abc} structure constants of the $SU(3)$ group and $f_{ab0} = 0$, $d_{ab0} = \sqrt{\frac{2}{3}}\delta_{ab}$. σ_a and π_a form the scalar and pseudoscalar meson nonets, respectively.

$$\begin{aligned}
T_a\sigma_a &= \frac{1}{\sqrt{2}}\begin{pmatrix} \frac{1}{\sqrt{2}}\,a_0^0 + \frac{1}{\sqrt{6}}\,\sigma_8 + \frac{1}{\sqrt{3}}\,\sigma_0 & a_0^- & \kappa^- \\ a_0^+ & -\frac{1}{\sqrt{2}}\,a_0^0 + \frac{1}{\sqrt{6}}\,\sigma_8 + \frac{1}{\sqrt{3}}\,\sigma_0 & \bar{\kappa}^0 \\ \kappa^+ & \kappa^0 & -\frac{2}{\sqrt{3}}\,\sigma_8 + \frac{1}{\sqrt{3}}\,\sigma_0 \end{pmatrix}, \\
T_a\pi_a &= \frac{1}{\sqrt{2}}\begin{pmatrix} \frac{1}{\sqrt{2}}\,\pi^0 + \frac{1}{\sqrt{6}}\,\pi_8 + \frac{1}{\sqrt{3}}\,\pi_0 & \pi^- & K^- \\ \pi^+ & -\frac{1}{\sqrt{2}}\,\pi^0 + \frac{1}{\sqrt{6}}\,\pi_8 + \frac{1}{\sqrt{3}}\,\pi_0 & \bar{K}^0 \\ K^+ & K^0 & -\frac{2}{\sqrt{3}}\,\pi_8 + \frac{1}{\sqrt{3}}\,\pi_0 \end{pmatrix},
\end{aligned}$$

where the charged and neutral pions are $\pi^\pm \equiv (\pi_1 \pm i\,\pi_2)/\sqrt{2}$ and $\pi^0 \equiv \pi_3$, respectively. For kaons, $K^\pm \equiv (\pi_4 \pm i\,\pi_5)/\sqrt{2}$, $K^0 \equiv (\pi_6 + i\,\pi_7)/\sqrt{2}$, and the conjugate $\bar{K}^0 \equiv (\pi_6 - i\,\pi_7)/\sqrt{2}$. The remaining pseudoscalar components π_0 and π_8 mix into the η and η' meson. For scalar mesons, a_0 and κ are the parity partners of pion and kaon, respectively. The remaining scalar components σ_0 and σ_8 mix into the σ and f_0 meson.

We can include the following simple linear term for explicit breaking effects [36, 38]

$$V_b = \mathrm{Tr}\left[H(\Phi + \Phi^\dagger)\right], \tag{A.4}$$

where $H = T_ah_a$. Here h_a are external fields that explicitly break the chiral symmetry. More explicitly, h_8 is responsible for breaking the degeneracy between strange and non-strange sectors, while h_3 is responsible for the isospin breaking of the non-strange sector. In the following discussion, we focus on the isospin-symmetric case where $h_3 = 0$.

The minimal model gives the right mass predictions for η and η', but yields the value of m_{f0}, m_κ larger than 1 GeV. The difficulty on fitting all scalar meson masses below 1 GeV is common for any known variation of the linear sigma model if only the minimal linear explicit breaking term is included, like the variation with a large departure on input data [39], with vector mesons included, or with a replacement of t'Hooft term by the Veneziano-Witten term [40]. This motivates us to extend the explicit breaking sector.

A.2 Generalized Meson Model

We generalize the minimal model by including all possible explicit breaking terms. The full potential is:

$$V = V_{\text{inv}} + V_b \tag{A.5}$$

where V_{inv} is the chiral invariant part:

$$V_{\text{inv}} = \lambda_1 \left(\text{Tr }\Phi^\dagger\Phi\right)^2 + \lambda_2 \,\text{Tr}\left(\Phi^\dagger\Phi\Phi^\dagger\Phi\right) + m^2\,\text{Tr}\left(\Phi^\dagger\Phi\right) + c\left(\det\Phi + \det\Phi^\dagger\right). \tag{A.6}$$

The c term breaks the axial $\text{U}(1)_\text{A}$ symmetry explicitly. And V_b explicit break the $SU(3)_L \times SU(3)_R$ chiral symmetry:

$$V_b = \sum_{i=1}^{8} V_{bi}, \tag{A.7}$$

$$\begin{aligned}
V_{b1} &= b_1\,\text{Tr}\left(\Phi^\dagger\mathcal{M} + h.c.\right), & V_{b2} &= b_2\epsilon_{ijk}\epsilon_{mnl}\mathcal{M}_{im}\Phi_{jn}\Phi_{kl} + h.c.\,, \\
V_{b3} &= b_3\,\text{Tr}\left(\Phi^\dagger\Phi\Phi^\dagger\mathcal{M}\right) + h.c.\,, & V_{b4} &= b_4\,\text{Tr}\left(\Phi^\dagger\Phi\right)\text{Tr}\left(\Phi^\dagger\mathcal{M}\right) + h.c.\,, \\
V_{b5} &= b_5\,\text{Tr}\left(\Phi^\dagger\mathcal{M}\Phi^\dagger\mathcal{M}\right) + h.c.\,, & V_{b6} &= b_6\,\text{Tr}\left(\Phi\Phi^\dagger\mathcal{M}\mathcal{M}^\dagger + \Phi^\dagger\Phi\mathcal{M}^\dagger\mathcal{M}\right), \\
V_{b7} &= b_7\left(\text{Tr}\,\Phi^\dagger\mathcal{M} + h.c.\right)^2, & V_{b8} &= b_8\left(\text{Tr}\,\Phi^\dagger\mathcal{M} - h.c.\right)^2,
\end{aligned} \tag{A.8}$$

where $\mathcal{M} = \text{diag}(m_{u0}, m_{d0}, m_{s0}) = \bar{m}_{ud}\,\text{diag}(1,1,x)$ is the current quark mass matrix, with $\bar{m}_{ud} = (m_u + m_d)/2$ and $x = m_{s0}/\bar{m}_{ud}$. Here we have removed three redundant terms

$$b_9 e_{ijk}e_{mnl}\Phi_{im}\mathcal{M}_{jn}\mathcal{M}_{kl} + h.c.,\; b_{10}\,\text{Tr}\left(\Phi^\dagger\mathcal{M}\mathcal{M}^\dagger\mathcal{M}\right) + h.c.,\; b_{11}\,\text{Tr}\left(\mathcal{M}^\dagger\mathcal{M}\right)\text{Tr}\left(\mathcal{M}^\dagger\Phi\right) + h.c., \tag{A.9}$$

from the Kaplan-Manohar ambiguity [127].

This extension can make the fitting of all the meson nonet masses below 1 GeV possible, where other studies with the V_{b1} term only failed [36, 38, 40]. The values of the b_i coefficients are made more physical by normalizing with the formalism of Naive Dimensional Analysis (NDA) [128]:

$$\begin{aligned}
\bar{\lambda}_{1,2} &= \frac{f_\pi^2}{\Lambda^2}\lambda_{1,2},\ \bar{m}^2 = \frac{1}{\Lambda^2}m^2,\ \bar{c} = \frac{f_\pi}{\Lambda^2}c,\ \bar{b}_1 = \frac{1}{f_\pi \Lambda}b_1, \\
\bar{b}_2 &= \frac{1}{\Lambda}b_2,\ \bar{b}_{3,4} = \frac{f_\pi}{\Lambda}b_{3,4},\ \bar{b}_{5-8} = b_{5-8},
\end{aligned} \tag{A.10}$$

where f_π is the pion decay constant, and $\Lambda = 4\pi f_\pi$ is an effective cutoff. Hereafter we only use the NDA couplings and omit the bars.

The chiral symmetry breaking is realized by the non-zero vacuum expectation values at the potential minimum,

$$\langle\Phi\rangle = T_0 v_0 + T_8 v_8 = \frac{1}{2}\mathrm{diag}(v_n, v_n, \sqrt{2}v_s), \tag{A.11}$$

where we have used the relation

$$\begin{pmatrix}\sigma_n \\ \sigma_s\end{pmatrix} = \frac{1}{\sqrt{3}}\begin{pmatrix}\sqrt{2} & 1 \\ 1 & -\sqrt{2}\end{pmatrix}\begin{pmatrix}\sigma_0 \\ \sigma_8\end{pmatrix}. \tag{A.12}$$

The deformation by $\mathcal{M}$ naturally implies an $SU(3)$ breaking vacuum $v_n \neq \sqrt{2}v_s$. A standard gauging of the model then leads to $v_n = f_\pi = 92\,\mathrm{MeV}$, $v_s = \sqrt{2}f_K - f_\pi/\sqrt{2} = 90.5\,\mathrm{MeV}$ [37, 38].

The mass spectra for the scalar and pseudoscalar nonets are derived by

$$\mathbb{M}^2_{s,ab} = \partial^2 V/\partial\sigma_a\partial\sigma_b, \tag{A.13}$$

$$\mathbb{M}^2_{p,ab} = \partial^2 V/\partial\pi_a\partial\pi_b. \tag{A.14}$$

With the isospin symmetry, the mass spectra are $m^2_{a_0} = \mathbb{M}^2_{s,11} = (\mathbb{M}_S)_{22} = (\mathbb{M}_S)_{33}$, $m^2_\kappa = \mathbb{M}^2_{s,44}$, $m^2_\pi = \mathbb{M}^2_{p,11} = (\mathbb{M}_P)_{22} = (\mathbb{M}_P)_{33}$, $m^2_K = \mathbb{M}^2_{p,44}$ and $m^2_\sigma, m^2_{f_0}, m^2_\eta, m^2_{\eta'}$ after diagonalizing the $(0,8)$ sectors through the rotations:

$$\sigma_0 = \cos\theta_s\sigma - \sin\theta_s f_0, \quad \sigma_8 = \sin\theta_s\sigma + \cos\theta_s f_0, \tag{A.15}$$

and

$$\pi_0 = \cos\theta_p\eta' - \sin\theta_p\eta, \quad \pi_8 = \sin\theta_p\eta' + \cos\theta_p\eta, \tag{A.16}$$

so that the mass matrix transforms as:

$$\begin{aligned}
m^2_{\phi_1} &= (m_i^2)_{00}\cos^2\theta_i + (m_i^2)_{88}\sin^2\theta_i + (m_i^2)_{08}\sin 2\theta_i, \\
m^2_{\phi_2} &= (m_i^2)_{00}\sin^2\theta_i + (m_i^2)_{88}\cos^2\theta_i - (m_i^2)_{08}\sin 2\theta_i,
\end{aligned} \tag{A.17}$$

with

$$\tan 2\theta_i = \frac{2\,(m_i^2)_{08}}{(m_i^2)_{00} - (m_i^2)_{88}}, \tag{A.18}$$

where $i = S, (\phi_1, \phi_2) = (\sigma, f_0)$ or (f_0, σ) for the scalar sector, and $i = P, (\phi_1, \phi_2) = (\eta', \eta)$ or (η, η') for the pseudo-scalar sector. Note that from Eq. (A.18) the θ angle should lies between $[-45°, 45°]$, but one can rotate ϕ_1 to ϕ_2 via replacement $\theta \to \theta + \frac{\pi}{2}$ to account the degeneracy $\sigma \leftrightarrow f_0$ and $\eta \leftrightarrow \eta'$, so that the real periodicity is 180 degree. In the following figures, we shift the result of domain $[-135°, -45°]$ to $[-45°, 45°]$ denoted by the lighter colour lines.

A.3 Solutions for Couplings

We determine the 12 couplings $(\lambda_1, \lambda_2, c, m^2, b1 \sim b8)$ by solving the EOM with 6 inputs from the pseudoscalar nonet $(m_\pi, m_K, f_K, f_\pi, m_\eta, m_{\eta'})$, 4 inputs from the scalar nonet $(m_\sigma(500), m_{f0}(980), m_\kappa(500), m_{a0}(980))$, and the mixing angle (θ_p, θ_s). All inputs for solving the system are shown in table A.1. Note that the mixing angles are adjusted to fit the decay width constraints shown in Table A.2.

Table A.1: The experimental constraints on the meson masses (in MeV) [37].

	m_σ	m_κ	m_{a_0}	m_{f_0}	m_π	m_K	m_η	m'_η	θ_s	θ_p
Exp	400-550	700-900	980 ± 20	990 ± 20	138	496	548	958	NA	NA

Table A.2: The experimental values of decay widths [37]. Units are MeV for the scalar mesons, and are keV for the pseudoscalar mesons.

	$\Gamma_{\eta\to\gamma\gamma}$	$\Gamma_{\eta'\to\gamma\gamma}$	$\Gamma_{\sigma\to\pi\pi}$	$\Gamma_{\kappa\to K\pi}$	$\Gamma_{f_0\to\pi\pi}$	$\Gamma_{a_0\to\eta\pi}$
Exp	0.52-0.54	4.2-4.5	400-700	~ 500	10-100	50-100

Here we point out some general features observed from the exact solution:

- $(\lambda_2, c, b_3, b_5, b_6, b_8, \epsilon)$ have no any dependence on $(m_\sigma, f_0, \theta_s)$.
- The decay widths of κ and a_0 only depend on (λ_2, c, b_3), all of which are independent of $(m_\sigma, f_0, \theta_s)$ from point above. Therefore the variations of $(m_\sigma, f_0, \theta_s)$ won't have any influence on the decay widths of κ and a_0.

- The decay width of σ_0 has no dependence on m_{f0}, and the decay width of f_0 has no dependence on m_σ. This inverse relation can be seen easily simply from an interchange symmetry accompanied with $\theta_s \to \theta_s + \pi/2$ in the their definition from the (0, 8) basis to this mass basis.

- The combination $(\lambda_1 + \lambda_2/2)$ is independent of θ_p, and thus θ_p is irrelevant to the global stability condition $(\lambda_1 + \lambda_2/2) > 0$.

The explicit solutions are plotted in Fig. A.1, Fig. A.2, Fig. A.3 and Fig A.4, where we use lighter colour to denote the results shifted from from $\theta \to \theta + \pi/2$. For those couplings having no dependence on $\theta_s\,(\theta_P)$, we present them as functions of $\theta_P\,(\theta_S)$.

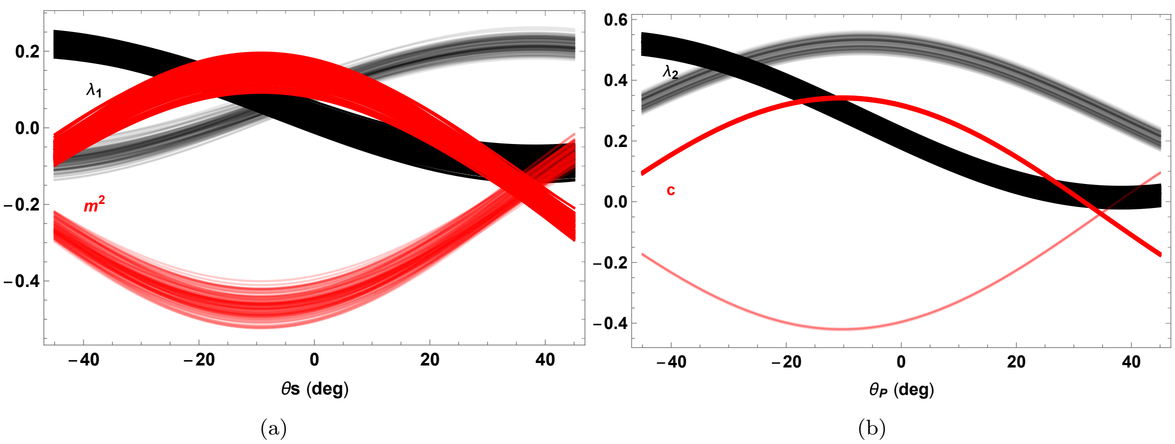

Figure A.1: Couplings of chiral invariant terms λ_1, m^2 that are θ_s-dependent (left), and λ_2, c that only depend on θ_p (right).

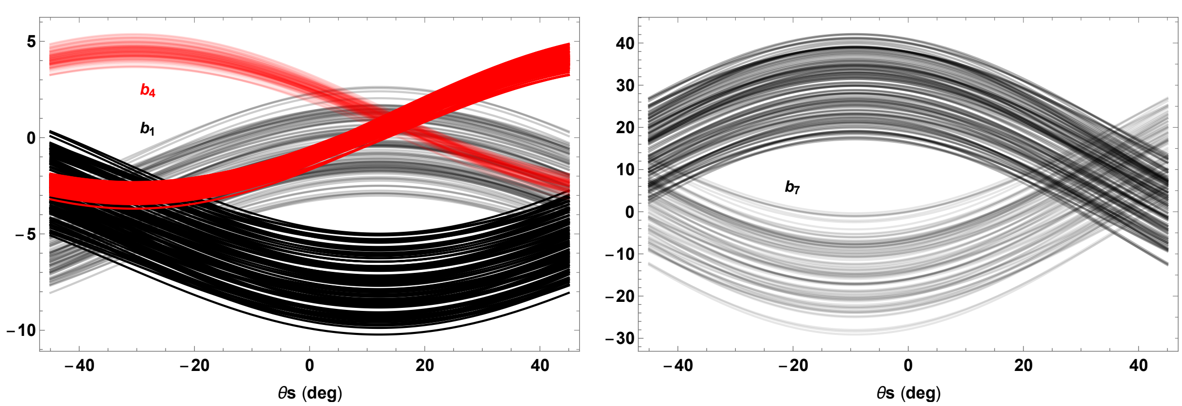

Figure A.2: Couplings of explicit breaking terms that are θ_s-dependent: b_1, b_4 (left) and b_7 (right).

We observe two interesting features observed from the numerical solution:

- Only λ_1, m^2, and b_4 are sensitive to the variation of m_σ compared to that of m_κ.

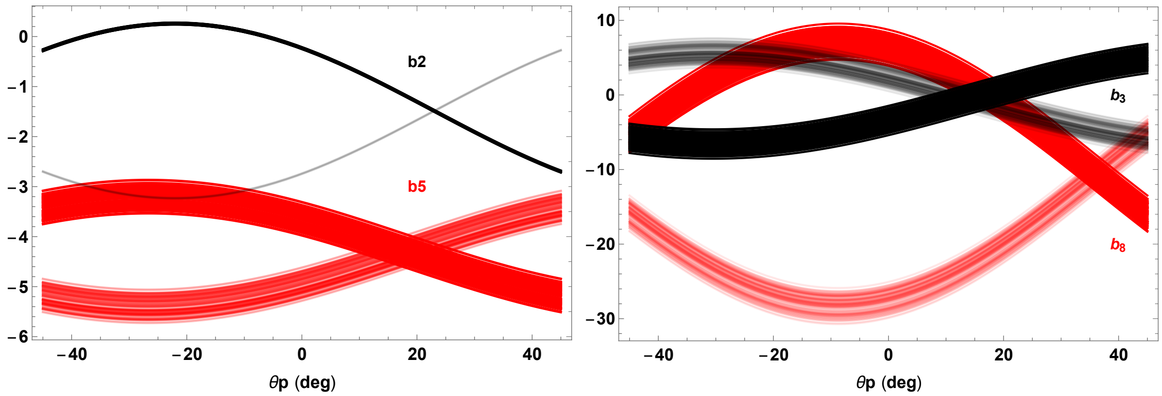

Figure A.3: Couplings of explicit breaking terms b_2, b_5 (left), b_3, b_8 (right) that only depend on θ_p.

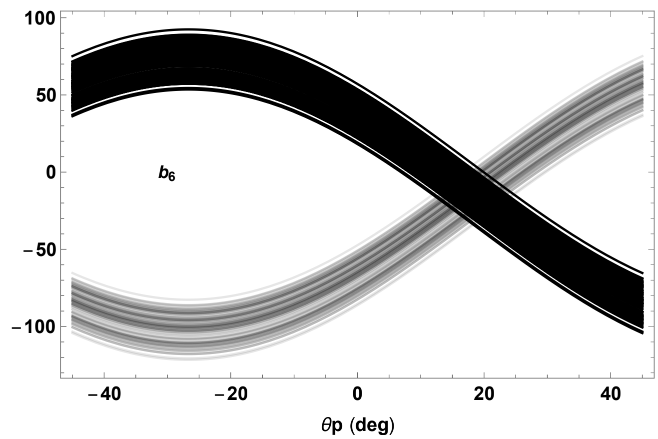

Figure A.4: Coupling of explicit breaking term b_6 that only depends on θ_p.

- The potential height along the non-strange direction is only sensitive to the variations of m_σ and m_π.

A.4 Decay Widths

From the Feynman diagrams, we know that the decay width of $a \to b + c$ is

$$\Gamma = \frac{S|\mathbf{p}|}{8\pi m_a^2} g_a^2, \tag{A.19}$$

where

$$|\mathbf{p}| = \frac{\sqrt{m_a^4 - 2m_a^2 m_b^2 - 2m_a^2 m_c^2 + m_b^4 - 2m_c^2 m_b^2 + m_c^4}}{2m_a}, \tag{A.20}$$

with S accounting for the symmetry and flavour factors. Here g_a is the coupling strength (vertex factor), which can be extracted from the expansion of the meson potential over the flavour basis. Thus, the decay width of σ ($\sigma \to \pi\pi$) has the form:

$$\begin{aligned} g_\sigma = &-\frac{\sqrt{3}}{12}[\sqrt{2}\cos\theta_s\left((-4f_K - 2f_\pi)\lambda_1 - 2f_\pi\lambda_2 + c - 2b_3 - 2(x+2)b_4\right) \\ &- 2\sin\theta_s((-4f_K + 4f_\pi)\lambda_1 + f_\pi\lambda_2 + c + b_3 - 2(x-1)b_4)], \end{aligned} \tag{A.21}$$

with the factor $S_\sigma = 3/2 \cdot 2^2 = 6$. From the rotational symmetry between $\phi_1 \to \phi_2$, we can directly obtain $g_{f_0} = g_\sigma|_{\theta_s \to \theta_s + \frac{\pi}{2}}$, with the same factor $S_{f_0} = 3/2 \cdot 2^2 = 6$. The dominant Brit-Wigner decay widths of the scalar mesons σ and f_0 predicted from our model are shown Figure A.5a. One can see that the θ_s value is mainly constrained by the decay widths of σ and f_0, which prefer $\theta_s \in [20°, 35°]$. Interestingly, this range gives a small $\bar{b}_7$ referring to Figure A.6. The band of Γ_{f_0} is narrower mainly because it has no

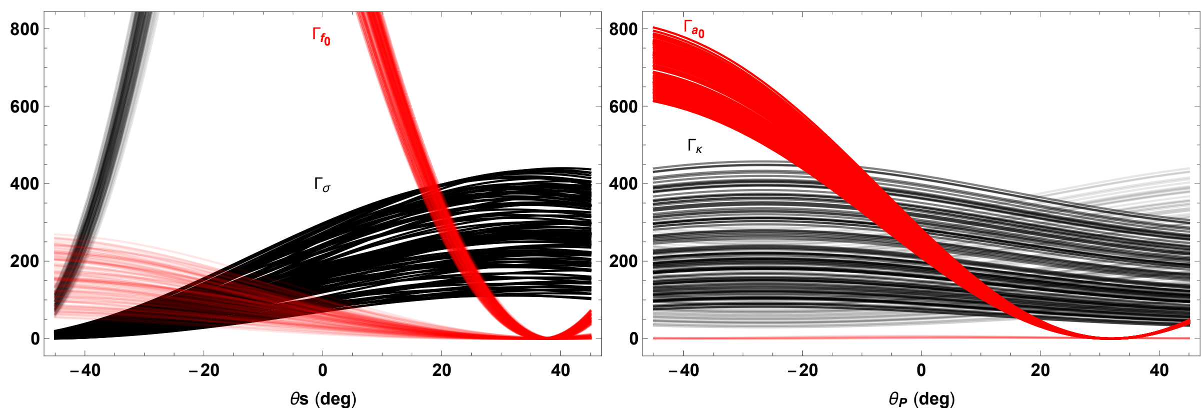

(a) Decay widths of σ (black) and f_0 (red) in units of MeV (b) Decay widths of κ (black) and a_0 (red) in units of MeV

Figure A.5: Decay widths of scalar mesons with the couplings solutions

dependence on m_σ, which instead causes a large uncertainty band for Γ_σ.

For the dominant decay width of κ ($\kappa \to K\pi$):

$$g_\kappa = \frac{1}{2}\left((-2f_K + f_\pi)\lambda_2 - c - xb_3\right), \tag{A.22}$$

with factor S_κ=3. For $a_0(980)$ ($a_0 \to \eta\pi$):

$$g_{a_0} = \frac{\sqrt{3}}{6}[\sqrt{2}\sin\theta_p(-2f_\pi\lambda_2 + c - 2b_3) + 2\cos\theta_p(f_\pi\lambda_2 + c + b_3)], \tag{A.23}$$

with the factor S_{a_0}=1. Considering that the decay widths of κ, a_0 have no dependence on θ_s, we show their results as functions of θ_p in Figure A.5b.

An important caveat is that, when comparing the calculated results to the experimental value of the decay widths of $f_0(980)$ ($f_0 \to \pi\pi$) and $a_0(980)$ ($a_0 \to \eta\pi$), we need to further include the threshold effects using Flatté method [129, 131], in which the cross section being close to the mass threshold takes the form:

$$\sigma_{el} = 4\pi |f^{\phi}|^2, \quad f^{\phi} = \frac{1}{|\mathbf{p}|} \frac{m_R \Gamma_{\phi}}{m_R^2 - s - i m_R (\Gamma_{\phi} + \Gamma^{\phi}_{K\bar{K}})}, \tag{A.24}$$

where $\phi = f_0$ or a_0, and $s = (p_1 + p_2)^2 \approx m_R^2$ with m_R as the resonance mass. $\Gamma^{\phi}_{K\bar{K}} = \bar{g}^{\phi}_K \sqrt{s/4 - m_K^2}$ above threshold, $\Gamma^{\phi}_{K\bar{K}} = i\bar{g}^{\phi}_K \sqrt{m_K^2 - s/4}$ below threshold, with $\bar{g}^{\phi}_K$ the coupling (vertex factor) of ϕ to the two kaons. Γ_{ϕ} denotes $\Gamma_{f_0 \to \pi\pi}$ and $\Gamma_{a_0 \to \eta\pi}$. Then from Eq. (A.24), we can directly obtain the half width of σ_{el}.

The diphoton decay widths of pseudoscalar mesons has the expression [131]:

$$\Gamma_{P\gamma\gamma} = \frac{|\vec{p}|^3}{8\pi} |A_{P\gamma\gamma}|^2, \tag{A.25}$$

where $|\vec{p}| = m/2$, and

$$\begin{aligned} A_{\eta\gamma\gamma} &= -\frac{5}{9} T_u^P \sin\bar{\psi}_P - \frac{\sqrt{2}}{9} T_s^P \cos\bar{\psi}_P, \\ A_{\eta'\gamma\gamma} &= \frac{5}{9} T_u^P \cos\bar{\psi}_P - \frac{\sqrt{2}}{9} T_s^P \sin\bar{\psi}_P, \\ A_{\pi^0\gamma\gamma} &= \frac{1}{3} T_u^P, \end{aligned} \tag{A.26}$$

with

$$T_u^P = \frac{N_c \alpha}{\pi f_\pi}, \quad T_s^P = \frac{N_c \alpha}{\pi (2 f_K - f_\pi)}. \tag{A.27}$$

where $\alpha = 1/137$. The results are shown in Figure A.6. We see that the most probable

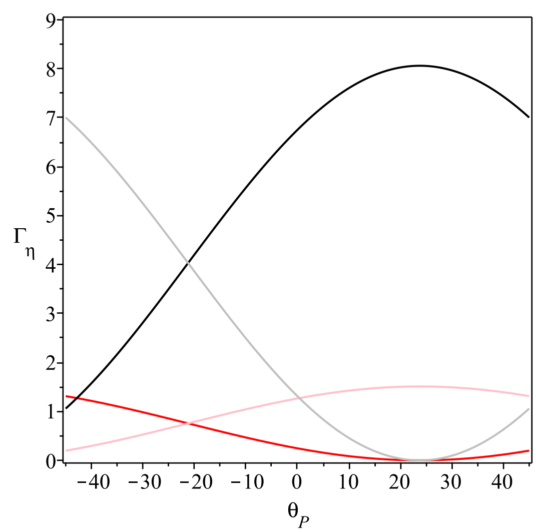

Figure A.6: The diphoton decay widths of η (red) and η' (black) in units of keV vs θ_p in units of degree. Lines with lighter colour denote the results 90°-shifted from the $\theta_P \in [-135°, -45°]$ domain.

region to fit the experimental diphoton width constraint is $\theta_P \in [-20°, -10°]$.

A.5 Benchmark Sets

Here we present two explicit benchmarks, the inputs of which are shown in Table A.3. The parameters of set 1 are chosen to give a good fit to the experimental data of the

Table A.3: The choice of inputs for the benchmark sets

	m_σ	m_κ	m_{a_0}	m_{f_0}	m_π	m_K	m_η	m'_η	θ_s	θ_p
Set 1	555	900	980	990	138	496	548	958	31.5°	−15.0°
Set 2	555	916	887	955	148	454	569	916	21.7°	−10.8°

mass spectrum. However, this leads to a rather large value for the NDA coupling $\bar{b}_6$, as Table A.4 shows. Therefore, given the theoretical uncertainties associated with the neglected higher dimensional terms, allowing the masses and decay widths to depart from the experimental values could be more sensible. Set 2 is such an example with deviations up to 10% but can give smaller NDA couplings. The resulted (NDA) couplings of the two benchmarks is shown in Table A.4.

Table A.4: The solution of NDA couplings for the benchmark sets

	λ_1	λ_2	m^2	c	b_1	b_2	b_3	b_4	b_5	b_6	b_7	b_8
Set 1	−0.06	0.33	−0.13	0.33	−4.4	0.19	−4.2	2.5	−3.0	50	1.4	4.7
Set 2	0.04	0.16	0.05	0.27	−1.6	−0.14	−0.18	0.09	4.0	5.2	−3.9	−5.5

The resulted predictions for the decay widths are shown in Table A.5. The f_0, a_0 widths have large threshold corrections, and thus the corresponding Flatté [129] widths are calculated.

Table A.5: The prediction of decay widths (in MeV, keV for scalar, pseudoscalar) from the benchmark sets.

	$\Gamma_{\eta\to\gamma\gamma}$	$\Gamma_{\eta'\to\gamma\gamma}$	$\Gamma_{\sigma\to\pi\pi}$	$\Gamma_{\kappa\to K\pi}$	$\Gamma_{f_0\to\pi\pi}$	$\Gamma_{a_0\to\eta\pi}$
Set 1	0.59	4.90	442	451	11	37.4
Set 2	0.54	4.87	422	537	20	52.0

A.6 Isospin breaking

We generalize this study to the isospin breaking case by replacing the spurion matrix $\mathcal{M} = (\bar{m}_{ud}, \bar{m}_{ud}, m_s)$ with $\mathcal{M} = \bar{m}_{ud}\,(1-\tau, 1+\tau, x)$, where the parameter $\tau = (m_d - m_u)/(m_d + m_u) \approx 0.38$, representing the size of isospin breaking. We can expand our results into perturbative series of τ. This inclusion of isospin breaking contributes to a change of scalar potential δV. Then we find the new minimum of $V + \delta V$, allowing the values of the scalar fields to have $v_u \neq v_d$. From the second derivatives at the minimum, the new mass matrices and mixing angles are thus determined. We find that the relevant physical quantities, like the mass spectrum, change less than 1%, as shown in Table A.6. These departures are small since $\bar{m}_{ud}\tau/(4\pi f_\pi)$ is small.

Table A.6: Comparison of model fit for the isospin symmetric case and the isospin breaking case (for set 1)

Set	m_σ	m_κ	m_π	m_K	m_η	$m_{\eta'}$	f_π	f_K	m_{a_0}	m_{f_0}
isospin symmetric	550	900	138	496	547	957.78	92	110	980	980
isospin breaking	555.1	903.62	138.58	488.7	548	957.84	92	109.3	980.1	994.4

However, the isospin breaking turns on the $\pi^0 - \eta(\eta')$ mixing angles ϵ and ϵ', which parameterize the basis transformation matrix from the flavour basis to the mass basis:

$$\begin{pmatrix} \pi^0 \\ \eta \\ \eta' \end{pmatrix} = U \begin{pmatrix} \phi_3 \\ \eta_{ns} \\ \eta_s \end{pmatrix}, \tag{A.28}$$

where the unitary matrix U is parameterized as

$$U = \begin{pmatrix} 1 & \epsilon_1 + \epsilon_2 \cos\psi & -\epsilon_2 \sin\psi \\ -\epsilon_2 - \epsilon_1 \cos\psi & \cos\psi & -\sin\psi \\ -\epsilon_1 \sin\psi & \sin\psi & \cos\psi \end{pmatrix}, \tag{A.29}$$

with conventional definitions $\epsilon = \epsilon_2 + \epsilon_1 \cos\psi$, $\epsilon' = \epsilon_1 \sin\psi$, assuming $\epsilon,\ \epsilon' \ll 1$. And the flavour basis is related to the gauge basis via the transformation:

$$\begin{pmatrix} \phi_3 \\ \eta_{ns} \\ \eta_s \end{pmatrix} = V \begin{pmatrix} \phi_3 \\ \eta_0 \\ \eta_8 \end{pmatrix}, \quad \text{where } V = \frac{1}{\sqrt{3}} \begin{pmatrix} \sqrt{3} & 0 & 0 \\ 0 & \sqrt{2} & 1 \\ 0 & 1 & -\sqrt{2} \end{pmatrix}. \tag{A.30}$$

Thus, the transformation matrix from the gauge basis to the flavour basis is $S = UV$, which leads to the relation $\psi = \theta + \arctan\sqrt{2} \approx \theta + 54.74^\circ$. The diagonalization of mass matrix from (ϕ_3, ϕ_0, ϕ_8) basis to (π^0, η, η') basis via S determines $\epsilon = 0.018$ (for set 1), which is roughly consistent with experiments [132, 133], while ϵ' can be compared to future measurements.

A.7 Summary and Discussion

In this chapter, we studied a phenomenological meson model that describes the mass and decay width spectra of the lightest pseudoscalar and scalar meson nonets with a full set of explicit chiral symmetry breaking terms. A general scan of parameter space within the current experimental uncertainties is presented, and two explicit benchmarks are given. Some general features regarding the exact solutions are discussed. We also addressed the isospin breaking effect, which turns out to have negligible effect except for generating the ϵ parameter that is consistent with the experimental constraint.

Some further developments of this model may include reinvestigating the finite-temperature study of the chiral phase transition [38, 39], and the comparison of the generalized linear sigma model with chiral perturbation theory [190, 191, 192].

Appendix B

Yukawa Bound State with A Self-interacting Scalar

In this chapter, we study the Yukawa bound states, in which fermions Yukawa couple to a self-interacting real scalar. Both the bulk limit and the region of finite particle numbers are explored. General analyses are given, with a double-well type scalar potential as an explicit benchmark. This work elaborates the numerical method used in the study of finite-size effect in Chapter 6.

B.1 Introduction

The study of Yukawa bound states has been explored in the context of the Walecka model (introduced in Section 3.3.2), and of the fermion Q-balls (fermion non-topological soliton) [193, 194, 195], where the bound state stability is guaranteed by the conserved fermion number. A simple example of the fermion Q-ball is the case where the fermion field ψ couples to a hermitian scalar field σ via Yukawa interaction $-y\sigma\bar{\psi}\psi$. The fermion mass m_ψ is thus $m = y\sigma$. When the fermion number in the system is large, one can take the Thomas-Fermi approximation $dm/dr << m^2$, in which the scalar field varies very slowly compared to the scale of the fermion Compton wavelength. The scalar field can be self-interacting with a potential $U(\sigma)$, which is commonly assumed to have a double-well shape. The feedback of the Yukawa interaction can drive the scalar field rolling to different values, leading to the masses of the fermions changing spatially. A general feature is that the fermions tend to be much less massive in the interior than they are in the exterior, resulting in a bound state. The surface-dominant case where σ rolls between two degenerate minima of the scalar potential was studied in [193]. The volume-dominant case, in which σ rolls between the local maxima and the global minima of the scalar potential, was studied in [194].

More recently, Wise et al. [196] studied such Yukawa bound states but in the context of dark matter. In contrast to the preceding studies, they also studied the finite fermion number regime away from the bulk limit. However, in their study, the scalar is free of self-interactions. In this work, we complete the study by introducing self-interaction for the scalar sector, and explore the finite particle number regime away from the bulk limit. For simplicity, we only consider the volume-dominant case here, with the surface-dominant case left for the future work.

B.2 General Model

The Lagrangian for the general model of a Yukawa bound state is:

$$L = \bar{\psi}\partial^{\mu}\gamma_{\mu}\psi - m_{\psi}\bar{\psi}\psi - y\bar{\psi}\psi\phi + \frac{1}{2}(\partial\phi)^2 - V(\phi). \tag{B.1}$$

Treating fermions as particle and scalars as fields, for the static configuration we have

$$L = -\sum_i m(x_i)\sqrt{1-\dot{x_i}^2} - \int d^3x \left(\frac{1}{2}(\nabla\phi)^2 - V(\phi)\right), \tag{B.2}$$

where the effective fermion mass is

$$m(x_i) = m_{\psi} + y\phi(x_i). \tag{B.3}$$

From the Lagrangian above, the equation of motion (EOM) for the scalar field thus is:

$$\begin{aligned} \nabla^2\phi(x) &= y\sum_i \delta^3(x-x_i)\sqrt{1-\dot{x_i}^2} + \frac{\partial V(\phi(x))}{\partial\phi(x)} \\ &= y\sum_i \delta^3\left(x-x_i\right)\frac{m(x_i)}{\sqrt{m(x_i)^2+p_i^2}} + \frac{\partial V(\phi(x))}{\partial\phi(x)}, \end{aligned} \tag{B.4}$$

where we have substituted the fermion canonical momentum: $p_i = m(x_i)\dot{x}_i/\sqrt{1-\dot{x_i}^2}$. The Hamiltonian thus is:

$$H = \sum_i \sqrt{m(x_i)^2+p_i^2} - \frac{1}{2}\sum_i y\phi(x_i)\frac{m(x_i)}{\sqrt{m(x_i)^2+p_i^2}} + \int d^3x\left(V(\phi) - \frac{1}{2}\phi\frac{\partial V}{\partial\phi}\right). \tag{B.5}$$

For the degenerate fermion gas, the summation over all ith fermion translates to:

$$\sum_{i=1}^{N} \longrightarrow \int d^3r \int \frac{d^3p}{(2\pi)^3} f(r,p), \tag{B.6}$$

where $f(r,p) = 2\theta\,(p_F - p)\,\theta(R-r)$. Thus

$$N = \sum_i 1 = \frac{4}{3\pi}\int_0^R dr r^2 p_F^3. \tag{B.7}$$

Assuming that p_F is r-independent[1], we have

$$p_F = \left(\frac{9\pi N}{4}\right)^{1/3}\frac{1}{R}. \tag{B.8}$$

Substituting Eq. (B.6) into Eq. (B.4), the EOM of the scalar field becomes:

$$\frac{d^2\phi}{dr^2} + \frac{2}{r}\frac{d\phi}{dr} = \theta(R-r)F_f + F_\phi, \tag{B.9}$$

where

$$F_f = \frac{y}{\pi^2}m(r)^3 i(\frac{p_F}{m}), \tag{B.10}$$

$$F_\phi = \frac{\partial V}{\partial\phi}, \tag{B.11}$$

with

$$i(z) = \int_0^z du\frac{u^2}{\sqrt{1+u^2}} = \frac{1}{2}z\sqrt{1+z^2} - \frac{1}{2}\text{arcsinh}(z), \quad z = p_F/m. \tag{B.12}$$

To have a qualitative picture of Eq. (B.9), we can make an analogy with the EOM of the one dimensional particle mechanics ($\phi \leftrightarrow x$, $r \leftrightarrow t$):

$$\ddot{x} = -\frac{2}{t}\dot{x} + \theta(t_R - t)F_\psi + F_\phi, \tag{B.13}$$

which describes a unit mass particle that moves with a driving force F_ψ in the region of $0 \le t \le t_R$, plus a damping friction $f = -\frac{2}{t}\dot{x}$ and a force of resistance F_ϕ that both appear in entire time frame.

The energy from Eq. (B.5) is:

$$E = E_\psi + E_\phi, \tag{B.14}$$

[1]In the more realistic case, p_F should have dependence on r, such as the one based on hydrodynamics consideration [196]. We have examined our self-interacting case and found that such spatial dependence does not cause substantial change for our results. Therefore, we use the Eq. (B.8) as a good approximation of p_F for the following analysis.

where

$$E_\psi = \int_0^R dr \frac{4}{\pi} r^2 \left(m^4 h(\frac{p_F}{m}) - \frac{1}{2} y\phi m(r)^3 i(\frac{p_F}{m}) \right), \tag{B.15}$$

$$E_\phi = 4\pi \int drr^2 \left(V(\phi) - \frac{1}{2}\phi(x)\frac{\partial V}{\partial \phi} \right), \tag{B.16}$$

and

$$h(z) = \int_0^z duu^2\sqrt{1+u^2} = \frac{1}{4}(i(z) + z^3\sqrt{1+z^2}). \tag{B.17}$$

In the relativistic limit $z \gg 1$, $i(z) \to z^2$, $h(z) \to z^4/4$, while in the non-relativistic limit $z \ll 1$, $i(z) \to h(z) \to z^3/3$.

Note that Eq. (B.1) can be rewritten as

$$L = \bar{\psi}\partial^\mu \gamma_\mu \psi - y\Phi\bar{\psi}\psi + \frac{1}{2}(\partial\Phi)^2 - V(\Phi) \tag{B.18}$$

where $\Phi = v + \phi$, $v = m_\psi/y$. For a double-well potential

$$V(\Phi) = \frac{\lambda}{4!}(\Phi^2 - v^2)^2 = \frac{\lambda\Phi^4}{4!} - \frac{1}{12}\lambda v^2\Phi^2 + \frac{\lambda v^4}{4!}, \tag{B.19}$$

after substitution $\lambda = 6u^2/v^2$ and $\Phi = v + \phi$, the expression changes to

$$V(\phi) = \frac{u^2}{4v^2}\phi^4 + \frac{u^2}{v}\phi^3 + u^2\phi^2. \tag{B.20}$$

Referring to Eq. (B.16), to have a finite total energy, $\phi(r \to \infty)$ must reach the zero of $\big(V(\phi) - \frac{1}{2}\phi\, \partial V/\partial\phi\big)$, i.e. $\phi = 0$ or $\phi = -2v$, being the degenerate vacua of $V(\phi)$.

B.2.1 Bulk limit

In the large particle number (bulk) limit, one can take the mean field approximation for the scalar field, so that Eq. (B.9) reduces to $F_f = -F_\phi$, i.e.

$$\frac{y}{\pi^2} m(r)^3 i(\frac{p_F}{m}) = -\frac{\partial V}{\partial \phi}. \tag{B.21}$$

Notice that both F_f and F_ϕ approach to zero when ϕ is close to the local maximum of the scalar potential where $\partial V/\partial\phi \to 0$ and $m \to 0$, giving an EOM solution $\phi \approx -v$. The result of energy can thus obtained by taking the relativistic limit ($z = p_F/m \gg 1$) of Eq. (B.15):

$$E_\psi \to \frac{4}{\pi}\int_0^R drr^2(m^4 h(z)) \to \frac{1}{\pi}\int_0^R drr^2(m_\psi^4 z^4) = c_0\frac{N^{4/3}}{R} = \frac{3}{4}p_F N. \tag{B.22}$$

And

$$E_\phi = \frac{4}{3}\pi R^3 V_0 = \frac{3\pi^2}{p_F^3} V_0 N, \tag{B.23}$$

from Eq. (B.16). Therefore, the total energy per particle number is

$$\epsilon = \frac{E}{N} = \frac{E_\psi + E_\phi}{N} = \frac{3}{4} p_F + \frac{3\pi^2}{p_F^3} V_0 \tag{B.24}$$

The minimization of E/N over p_F gives:

$$\epsilon_{\min} = 3^{1/4}\sqrt{2\pi}\, V_0^{1/4} \tag{B.25}$$

with $p_F = p_{\mathrm{Fm}} = 3^{1/4}\sqrt{2\pi} V_0^{1/4} = \epsilon_{\min}$. The binding energy per particle

$$\epsilon_B = m_\psi - \epsilon_{\min}, \tag{B.26}$$

is thus obtained. For the double-well potential Eq. (B.20).

$$V_0 = V(\Phi = 0) = V(\phi = -v) = \lambda v^4/4! = \frac{1}{4}u^2 v^2, \tag{B.27}$$

so that the analytical results above become:

$$\epsilon_{\min} = 3^{1/4}\sqrt{\pi}\sqrt{uv} = p_{\mathrm{Fm}} \tag{B.28}$$

from which $\epsilon_B = m_\psi - 3^{1/4}\sqrt{\pi}\sqrt{uv}$. Assuming $p_F \approx p_{Fm}$ for finite particle number, then from Eq. (B.8)

$$R_m = \left(\frac{9\pi N}{4}\right)^{1/3} \frac{1}{p_{Fm}} = \frac{c}{\sqrt{u\,v}} N^{1/3}, \tag{B.29}$$

where $c = 3^{5/12} 2^{-2/3} \pi^{1/6} \approx 0.823$.

B.2.2 Finite N

When the particle number decreases to finite value away from the bulk limit, the effective fermion mass gets larger so that the things become more non-relativistic, and the finite-size effect has to be accounted. The non-relativistic limit $z = p_F/m \ll 1$ is maximally achieved when $\phi \to 0$ so that $m \to m_\psi$ and $p_F \ll m_\psi$ so that $E_\phi \to 0$. In this limit, since

$$E_\psi = \frac{4}{\pi}\int_0^R drr^2(m^4 h(z)) \to 3m_\psi \frac{h(z)}{z^3},$$

the binding energy is thus

$$\epsilon_{UN} := m_\psi(1 - 3\frac{h(z)}{z^3}) \xrightarrow{z\to 0} 0^-. \tag{B.30}$$

For each particle number, we solve for the profile of the field $\phi(r)$ while scanning the radius R to find the configuration that minimizes the energy. The results on energy interpolate the aforementioned relativistic and non-relativistic limits. To be more specific, the shooting method is employed for the numerical solving. For any given N and R, we solve Eq. (B.9) for with the boundary conditions $\phi'|_{r=0} = 0$ and $\phi|_{r=0} = \phi_0$ for $r \leq R$, and then solve Eq. (B.9) for the $r > R$ domain using the obtained value of $\phi(R)$ and $\phi'(r = R)$ as the boundary condition. The value of ϕ_0 is determined via scanning from $-v$ to 0 until ϕ can reach zero somewhere at $r > R$. This scheme often requires very high precision when either u or N grows large.

We solve for the cases where $m_\psi = 100\,\text{GeV}$, $\alpha = y^2/(4\pi) = (0.1, 1.0, 5.0)$ and scalar mass $u = (10, 50, 100)\,\text{GeV}$. The units GeV can be replaced by any other units with mass dimension one, depending on what physics scale we are interested in. Results on the scalar field configurations for different particle numbers are shown in Figure B.1. In general, the field rolls between the $-v$ and zero from the interior to the exterior of the bound state, so that the fermions become more massive away from the center of the bound state. One can see that the scalar field becomes more like a constant as the particle number increases. The depth of the surface region becomes shallower as either the particle number or the scalar self-interacting strength increases.

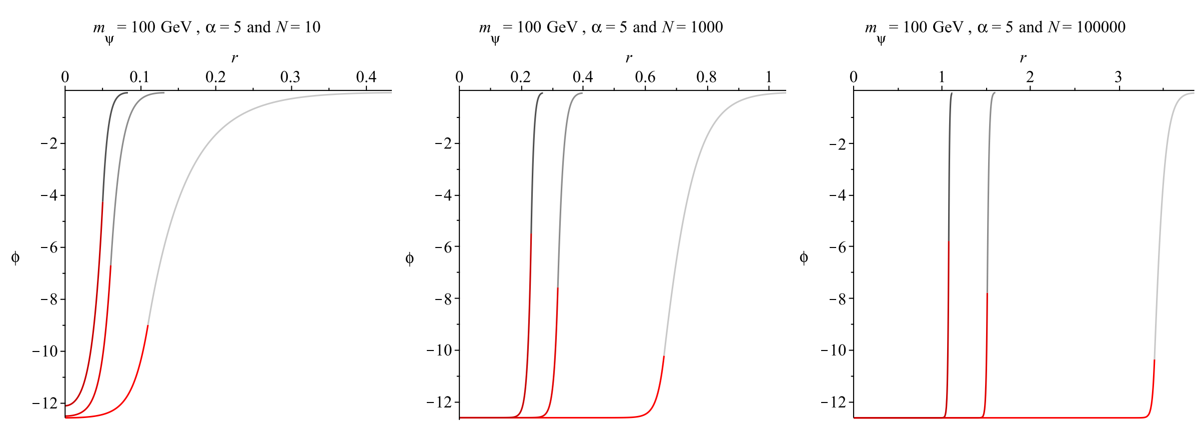

Figure B.1: Solutions of Eq. (B.9) with m_ψ=100 GeV, $\alpha = 5$ for $N = 10, 10^3, 10^5$ (left to right), respectively. Red lines denote the fields inside the bound states, while black lines map to the fields outside. Lines with darker colour are with larger u, which sample $u = (10, 50, 100)\,\text{GeV}$, respectively.

The boundary radius that minimizes the energy for a given particle number is shown in Figure B.2. In general, a larger scalar self-interaction or a smaller Yukawa coupling tends to suppress the size of the bound state radius. As we have examined, the numerical

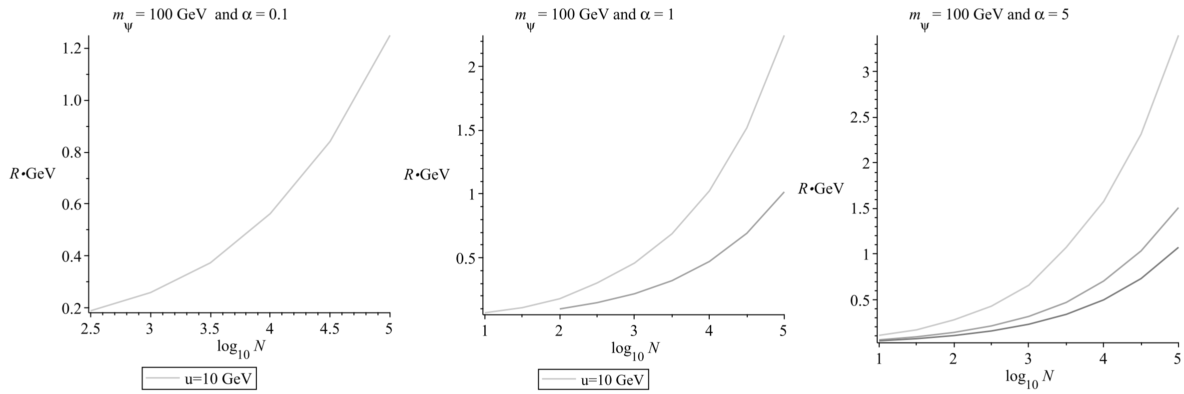

Figure B.2: Radius R that minimizes the energy vs the particle number N. Lines with darker colour are with larger u, which sample $u = (10, 50, 100)\,\mathrm{GeV}$, respectively.

result of the radius gives a very good match to the analytical prediction from Eq. (B.29).

Results on the binding energy per particle for different particle numbers are shown in Figure B.3. We can see that the relativistic (bulk) limit gives the upper bound of

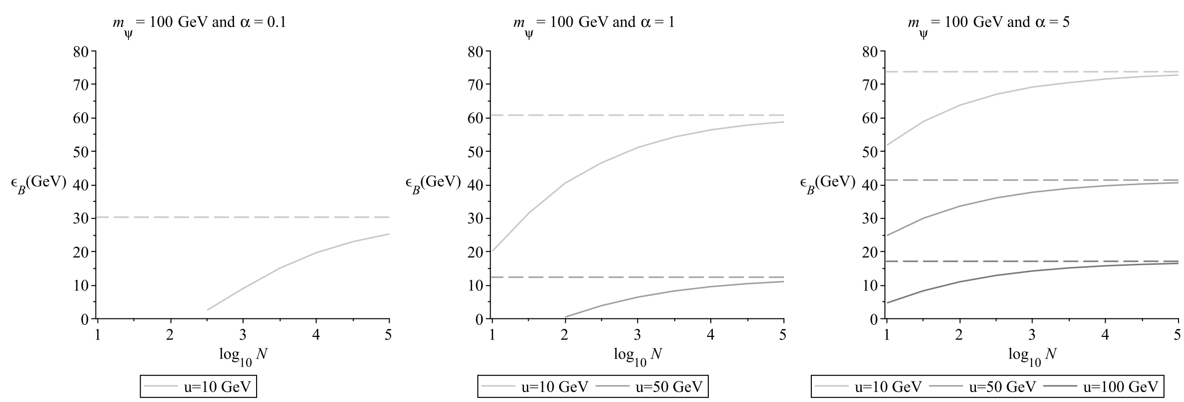

Figure B.3: The binding energy per fermion number $\epsilon_B(N)$. Lines with darker colour are with larger u, which sample $u = (10, 50, 100)\,\mathrm{GeV}$, respectively.

binding energy. One can see that a larger scalar self-interaction or a smaller Yukawa coupling tends to destabilize the bound state. Note that the cases with $u = 50, 100\,\mathrm{GeV}$ for $\alpha = 0.1$, and $u = 100\,\mathrm{GeV}$ for $\alpha = 1$, are not shown due to the fact that their binding energy turns out to be negative for any particle number. These numerical results match our expectation from Eq. (B.26).

B.3 Discussion

In this work, we studied the fermion bound state with a self-interacting scalar in the bulk limit and the finite particle number regime. With the shooting method employed, we can solve the equations of motion and obtain the results of the field, radius, and energy configuration for a given set of Yukawa coupling and scalar self-interacting strength. As the particle number increases, the bound state size increases and things become more relativistic. Therefore, the obtained results interpolate between the analytical expectation from the relativistic and non-relativistic limits. In general, the scalar self-interaction tends to destabilize the bound states, while the Yukawa coupling has the opposite effect.

Later we applied this work into the study of quark matter in [19], which was reproduced in Chapter 6 of this thesis. When we were trying to incorporate this work to the study of dark matter bound states, we became aware of the work [197], which carried out such studies. They also studied the synthesis of such bound states in early universe [198], and the related compact star physics in [199].

Bibliography

[1] S. Weinberg, Phys. Rev. Lett. **19**, 1264 (1967).

[2] K. G. Wilson, Phys. Rev. B **4**, 3174 (1971).

[3] K. G. Wilson, Phys. Rev. B **4**, 3184 (1971).

[4] D. J. Gross and F. Wilczek, Phys. Rev. Lett. **30**, 1343 (1973).

[5] D. J. Gross and F. Wilczek, Phys. Rev. D **8**, 3633 (1973).

[6] E. Gabrielli, M. Heikinheimo, K. Kannike, A. Racioppi, M. Raidal and C. Spethmann, Phys. Rev. D **89**, no. 1, 015017 (2014) [arXiv:1309.6632 [hep-ph]].

[7] H. Georgi, H. R. Quinn and S. Weinberg, Phys. Rev. Lett. **33**, 451 (1974).

[8] Y. Nambu and G. Jona-Lasinio, Phys. Rev. **122**, 345 (1961).

[9] Y. Nambu and G. Jona-Lasinio, Phys. Rev. **124**, 246 (1961).

[10] R. Gell-Mann and M. Levy, Nuovo Cimento 16, 705 (1960).

[11] S. Weinberg, Physica A **96**, no. 1-2, 327 (1979).

[12] J. Gasser and H. Leutwyler, Annals Phys. **158**, 142 (1984).

[13] J. Gasser and H. Leutwyler, Nucl. Phys. B **250**, 465 (1985).

[14] T. P. Cheng, E. Eichten and L. F. Li, Phys. Rev. D **9**, 2259 (1974).

[15] D. J. E. Callaway, Phys. Rept. **167**, 241 (1988).

[16] G. F. Giudice, G. Isidori, A. Salvio and A. Strumia, JHEP **1502**, 137 (2015).

[17] B. Holdom, J. Ren and C. Zhang, JHEP **1503**, 028 (2015).

[18] R. Mann, J. Meffe, F. Sannino, T. Steele, Z. W. Wang and C. Zhang, Phys. Rev. Lett. **119**, no. 26, 261802 (2017) [arXiv:1707.02942 [hep-ph]].

[19] B. Holdom, J. Ren and C. Zhang, Phys. Rev. Lett. **120** (2018) no.22, 222001 [arXiv:1707.06610 [hep-ph]].

[20] C. Zhang, arXiv:1908.10355 [astro-ph.HE].

[21] J. C. Pati and A. Salam, Phys. Rev. D **10**, 275 (1974) [Erratum-ibid. D **11**, 703 (1975)].

[22] S. L. Glashow. 1984. World Scientific. in Fifth Workshop on Grand Unification, K. Kang, H. Fried, and P. Frampton (eds.) Singapore,), p. 88.

[23] S. Weinberg, (1979), in General Relativity: An Einstein centenary survey, ed. S. W. Hawking and W. Israel, 790- 831.

[24] G. Veneziano, Nucl. Phys. B **159**, 213 (1979).

[25] D. F. Litim and F. Sannino, JHEP **1412** (2014) 178.

[26] B. Holdom, Phys. Lett. B **694** (2010) 74.

[27] A. Palanques-Mestre and P. Pascual, Commun. Math. Phys. **95** (1984) 277.

[28] J. A. Gracey, Phys. Lett. B **373** (1996) 178.

[29] R. Shrock, Phys. Rev. D 89, no. 4, 045019 (2014) [arXiv:1311.5268 [hep-th]].

[30] M. Beneke, Phys. Rept. **317**, 1 (1999) [hep-ph/9807443].

[31] I. Hinchliffe and A. V. Manohar, Ann. Rev. Nucl. Part. Sci. **50**, 643 (2000) [hep-ph/0004186].

[32] K. S. Stelle, Phys. Rev. D **16**, 953 (1977).

[33] A. Salvio and A. Strumia, JHEP **1406**, 080 (2014) [arXiv:1403.4226 [hep-ph]].

[34] J. F. Donoghue and G. Menezes, Phys. Rev. D **100**, no. 10, 105006 (2019) doi:10.1103/PhysRevD.100.105006 [arXiv:1908.02416 [hep-th]].

[35] J. F. Donoghue and G. Menezes, Phys. Rev. Lett. **123**, no. 17, 171601 (2019) doi:10.1103/PhysRevLett.123.171601 [arXiv:1908.04170 [hep-th]].

[36] N. A. Tornqvist, Eur. Phys. J. C **11**, 359 (1999) [hep-ph/9905282].

[37] C. Patrignani *et al.* [Particle Data Group], Chin. Phys. C **40**, no. 10, 100001 (2016) (see mini-review on scalar mesons).

[38] J. T. Lenaghan, D. H. Rischke and J. Schaffner-Bielich, Phys. Rev. D **62**, 085008 (2000) [nucl-th/0004006].

[39] Schaefer, B-J., and Mathias Wagner. "Three-flavor chiral phase structure in hot and dense QCD matter." Physical Review D 79.1 (2009): 014018.

[40] D. Parganlija, P. Kovacs, G. Wolf, F. Giacosa and D. H. Rischke, Phys. Rev. D **87**, no. 1, 014011 (2013) [arXiv:1208.0585 [hep-ph]].

[41] Alonso, Marcelo; Finn, Edward J. (1969). Fundamental University Physics. Vol. III. Quantum and Statistical Physics. Addison-Wesley Publishing Company. p. 297.

[42] P. Moller, W. D. Myers, W. J. Swiatecki and J. Treiner, Atomic Data and Nuclear Data Tables, 39 (1988) 225.

[43] Rohlf, J. W. (1994). Modern Physics from α to Z_0. John Wiley Sons. ISBN 978-0471572701.

[44] J. D. Walecka, Annals Phys. **83**, 491 (1974).

[45] N. K. Glendenning and S. A. Moszkowski, Phys. Rev. Lett. **67**, 2414 (1991).

[46] A. Chodos, R. L. Jaffe, K. Johnson, C. B. Thorne, and V. F. Weisskopf, Phys. Rev. D **9** (1974) 3471.

[47] A. Chodos, R. L. Jaffe, K. Johnson, and C. B. Thorne, Phys. Rev. D **10** (1974) 2599.

[48] E. Farhi and R. L. Jaffe, Phys. Rev. D **30** (1984) 2379.

[49] F. Weber, Prog. Part. Nucl. Phys. **54**, 193 (2005) [astro-ph/0407155].

[50] E. V. Shuryak, World Sci. Lect. Notes Phys. **71**, 1 (2004).

[51] P. Wang, V. E. Lyubovitskij, T. Gutsche and A. Faessler, Phys. Rev. C **67**, 015210 (2003) [hep-ph/0205251].

[52] E. Farhi and R. L. Jaffe, Phys. Rev. D **30**, 2379 (1984).

[53] H. Heiselberg, Phys. Rev. D **48**, 1418 (1993).

[54] A. R. Bodmer, Phys. Rev. D **4**, 1601 (1971).

[55] E. Witten, Phys. Rev. D **30**, 272 (1984).

[56] H. Terazawa, INS-Report-336 (INS, University of Tokyo, Tokyo) May, 1979.

[57] M. Buballa and M. Oertel, Phys. Lett. B **457**, 261 (1999) [hep-ph/9810529].

[58] P. Wang, V. E. Lyubovitskij, T. Gutsche and A. Faessler, Phys. Rev. C **67** (2003) 015210 [hep-ph/0205251].

[59] R. Balian and C. Bloch, Annals of Physics 60, 401 (1970)

[60] M. S. Berger and R. L. Jaffe, Phys. Rev. C **35**, 213 (1987).

[61] J. Madsen, Phys. Rev. D **50**, 3328 (1994).

[62] G. Lugones, A. G. Grunfeld and M. Al Ajmi, Phys. Rev. C **88**, no. 4, 045803 (2013) [arXiv:1308.1452 [hep-ph]].

[63] W. y. Ke and Y. x. Liu, Phys. Rev. D **89**, no. 7, 074041 (2014) [arXiv:1312.2295 [hep-ph]].

[64] A. F. Garcia and M. B. Pinto, Phys. Rev. C **88**, no. 2, 025207 (2013) [arXiv:1306.3090 [hep-ph]].

[65] L. F. Palhares and E. S. Fraga, Phys. Rev. D **82**, 125018 (2010) [arXiv:1006.2357 [hep-ph]].

[66] M. B. Pinto, V. Koch and J. Randrup, Phys. Rev. C **86**, 025203 (2012) [arXiv:1207.5186 [hep-ph]].

[67] E. S. Fraga, M. Hippert and A. Schmitt, Phys. Rev. D **99**, no. 1, 014046 (2019) [arXiv:1810.13226 [hep-ph]].

[68] D. N. Voskresensky, M. Yasuhira and T. Tatsumi, Nucl. Phys. A **723**, 291 (2003) [nucl-th/0208067].

[69] C. J. Xia, T. Maruyama, N. Yasutake and T. Tatsumi, Phys. Rev. D **99**, no. 10, 103017 (2019) [arXiv:1902.08766 [hep-ph]].

[70] R. C. Tolman, Phys. Rev. **55**, 364 (1939).

[71] J. R. Oppenheimer and G. M. Volkoff, Phys. Rev. **55**, 374 (1939).

[72] J. M. Lattimer and M. Prakash, Phys. Rept. **621**, 127 (2016) [arXiv:1512.07820 [astro-ph.SR]].

[73] P. Demorest, T. Pennucci, S. Ransom, M. Roberts and J. Hessels, Nature **467**, 1081 (2010) [arXiv:1010.5788 [astro-ph.HE]].

[74] J. Antoniadis *et al.*, Science **340**, 6131 (2013) [arXiv:1304.6875 [astro-ph.HE]].

[75] H. T. Cromartie *et al.*, arXiv:1904.06759 [astro-ph.HE].

[76] E. R. Most, L. R. Weih, L. Rezzolla and J. Schaffner-Bielich, Phys. Rev. Lett. **120**, no. 26, 261103 (2018) [arXiv:1803.00549 [gr-qc]].

[77] C. D. Capano *et al.*, arXiv:1908.10352 [astro-ph.HE].

[78] S. Koppel, L. Bovard and L. Rezzolla, Astrophys. J. **872**, no. 1, L16 (2019) [arXiv:1901.09977 [gr-qc]].

[79] F. Ozel and P. Freire, Ann. Rev. Astron. Astrophys. **54**, 401 (2016) [arXiv:1603.02698 [astro-ph.HE]].

[80] S. Weissenborn, I. Sagert, G. Pagliara, M. Hempel and J. Schaffner-Bielich, Astrophys. J. **740**, L14 (2011) [arXiv:1102.2869 [astro-ph.HE]].

[81] R. X. Xu, [Chin. J. Astron. Astrophys. Suppl. **6**, 02279 (2006)] [astro-ph/0512519].

[82] R. Anglani, R. Casalbuoni, M. Ciminale, N. Ippolito, R. Gatto, M. Mannarelli and M. Ruggieri, Rev. Mod. Phys. **86**, 509 (2014) [arXiv:1302.4264 [hep-ph]].

[83] J. L. Zdunik, Astron. Astrophys. **359**, 311 (2000) [astro-ph/0004375].

[84] P. Haensel, A. Y. Potekhin and D. G. Yakovlev, Astrophys. Space Sci. Libr. **326**, pp.1 (2007).

[85] S. Dubovsky, V. Gorbenko and M. Mirbabayi, JHEP **1309**, 045 (2013) [arXiv:1305.6939 [hep-th]].

[86] M. B. Einhorn and D. R. T. Jones, JHEP **1503**, 047 (2015) arXiv:1410.8513 [hep-th].

[87] J. Julve and M. Tonin, Nuovo Cim. B **46**, 137 (1978).

[88] E. S. Fradkin and A. A. Tseytlin, Nucl. Phys. B **201**, 469 (1982).

[89] O. K. Kalashnikov, Phys. Lett. B **72**, 65 (1977).

[90] G. Marques Tavares, M. Schmaltz and W. Skiba, Phys. Rev. D **89**, 015009 (2014) [arXiv:1308.0025 [hep-ph]].

[91] R. N. Mohapatra and J. C. Pati, Phys. Rev. D **11**, 566 (1975).

[92] E. Witten, Phys. Lett. B **117**, 324 (1982).

[93] S. Glashow, Trinification of all elementary particle forces, Providence Grand Unif. (1984) 0088.

[94] T. van Ritbergen, J. A. M. Vermaseren and S. A. Larin, Phys. Lett. B **400**, 379 (1997) [hep-ph/9701390].

[95] C. Pica, T. A. Ryttov and F. Sannino, arXiv:1605.04712 [hep-th].

[96] E. Molgaard and F. Sannino, Phys. Rev. D **96** (2017) 056004.

[97] H. Gies and L. Zambelli, arXiv:1611.09147 [hep-ph].

[98] C. Pica, T. A. Ryttov and F. Sannino, arXiv:1605.04712 [hep-th].

[99] E. Molgaard and F. Sannino, Phys. Rev. D **96** (2017) 056004.

[100] H. Gies and L. Zambelli, arXiv:1611.09147 [hep-ph].

[101] M. B. Einhorn and D. R. T. Jones, arXiv:1705.00751 [hep-ph].

[102] F. F. Hansen, T. Janowski, K. Langaeble, R. B. Mann, F. Sannino, T. G. Steele and Z. W. Wang, arXiv:1706.06402 [hep-ph].

[103] D. F. Litim, M. Mojaza and F. Sannino, JHEP **1601**, 081 (2016).

[104] J. K. Esbensen, T. A. Ryttov and F. Sannino, Phys. Rev. D **93**, 045009 (2016).

[105] G. M. Pelaggi, F. Sannino, A. Strumia and E. Vigiani, arXiv:1701.01453 [hep-ph].

[106] S. Abel and F. Sannino, arXiv:1704.00700 [hep-ph].

[107] F. Sannino, arXiv:1511.09022 [hep-ph].

[108] A. D. Bond, G. Hiller, K. Kowalska and D. F. Litim, JHEP **1708** (2017) 004.

[109] C. Pica and F. Sannino, Phys. Rev. D **83** (2011) 116001.

[110] O. Antipin, M. Gillioz, J. Krog, E. Mølgaard and F. Sannino, JHEP **1308** (2013) 034.

[111] D. Buttazzo, G. Degrassi, P. P. Giardino, G. F. Giudice, F. Sala, A. Salvio and A. Strumia, JHEP **1312** (2013) 089.

[112] D. R. T. Jones, Phys. Rev. D **25** (1982) 581.

[113] M. E. Machacek and M. T. Vaughn, Nucl. Phys. B **222** (1983) 83.

[114] K. G. Chetyrkin and M. F. Zoller, JHEP **1304** (2013) 091 Erratum: [JHEP **1309** (2013) 155].

[115] M. E. Machacek and M. T. Vaughn, Nucl. Phys. B **249** (1985) 70.

[116] R. Shrock, Phys. Rev. D **89** (2014) 045019.

[117] T. G. Steele and Z. W. Wang, Phys. Rev. Lett. **110** (2013) 151601.

[118] D. d'Enterria *et al.*, "Proceedings, High-Precision α_s Measurements from LHC to FCC-ee : Geneva, Switzerland, October 2-13, 2015," arXiv:1512.05194 [hep-ph].

[119] N. Itoh, Prog. Theor. Phys. **44**, 291 (1970).

[120] S. A. Chin and A. K. Kerman, Phys. Rev. Lett. **43**, 1292 (1979).

[121] A. Chodos, R. L. Jaffe, K. Johnson, C. B. Thorn and V. F. Weisskopf, Phys. Rev. D **9**, 3471 (1974).

[122] A. Zacchi, R. Stiele and J. Schaffner-Bielich, Phys. Rev. D **92**, no. 4, 045022 (2015) [arXiv:1506.01868 [astro-ph.HE]].

[123] C. Ratti, Europhys. Lett. **61**, 314 (2003) [hep-ph/0210295].

[124] for a review see M. Buballa, Phys. Rept. **407**, 205 (2005) [hep-ph/0402234].

[125] J. Moreira, J. Morais, B. Hiller, A. A. Osipov and A. H. Blin, Phys. Rev. D **91**, 116003 (2015) [arXiv:1409.0336 [hep-ph]].

[126] B. Holdom and Q. Wang, Phys. Rev. D **55**, 3101 (1997) [hep-ph/9612241].

[127] A. A. Osipov, B. Hiller and A. H. Blin, Eur. Phys. J. A **49**, 14 (2013) [arXiv:1206.1920 [hep-ph]].

[128] H. Georgi, Phys. Lett. B **298**, 187 (1993) [hep-ph/9207278].

[129] S. M. Flatte, Phys. Lett. **63B**, 224 (1976). Phys. Lett. **63B**, 228 (1976).

[130] D. V. Bugg, Eur. Phys. J. C **47**, 57 (2006) [hep-ph/0603089].

[131] A. A. Osipov, B. Hiller and A. H. Blin, Phys. Rev. D **88**, 054032 (2013) [arXiv:1309.2497 [hep-ph]].

[132] A. A. Osipov, B. Hiller and A. H. Blin, Phys. Rev. D **93**, no. 11, 116005 (2016) [arXiv:1501.06146 [hep-ph]].

[133] P. Kroll, Int. J. Mod. Phys. A **20**, 331 (2005) [hep-ph/0409141].

[134] T. D. Lee and Y. Pang, Phys. Rev. D **35**, 3678 (1987).

[135] S. Bahcall, B. W. Lynn and S. B. Selipsky, Nucl. Phys. B **325**, 606 (1989).

[136] A. V. Karpov, V. I. Zagrebaev and W. Greiner, FIAS Interdisc. Sci. Ser. 9783319441658, 31 (2017).

[137] E. Farhi and R. L. Jaffe, Phys. Rev. D **32**, 2452 (1985).

[138] M. C. Perillo Isaac *et al.*,s Phys. Rev. Lett. **81**, 2416 (1998) Erratum: [Phys. Rev. Lett. **82**, 2220 (1999)] [astro-ph/9806147].

[139] G. L. Shaw, M. Shin, R. H. Dalitz and M. Desai, Nature **337**, 436 (1989).

[140] I. Bombaci, D. Logoteta, I. Vidana and C. Providencia, Eur. Phys. J. A **52**, no. 3, 58 (2016) [arXiv:1601.04559 [astro-ph.HE]].

[141] A. Drago, A. Lavagno, G. Pagliara and D. Pigato, Eur. Phys. J. A **52**, no. 2, 40 (2016) [arXiv:1509.02131 [astro-ph.SR]].

[142] Q. Wang, T. Zhao and H. S. Zong, arXiv:1908.01325 [hep-ph].

[143] A. A. Osipov, B. Hiller and A. H. Blin, Phys. Rev. D **88**, 054032 (2013) doi:10.1103/PhysRevD.88.054032 [arXiv:1309.2497 [hep-ph]].

[144] J. Moreira, J. Morais, B. Hiller, A. A. Osipov and A. H. Blin, Phys. Rev. D **98**, no. 7, 074010 (2018) doi:10.1103/PhysRevD.98.074010 [arXiv:1806.00327 [hep-ph]].

[145] G. Aad *et al.* [ATLAS Collaboration], arXiv:1905.10130 [hep-ex].

[146] B. P. Abbott *et al.* [LIGO Scientific and Virgo Collaborations], Phys. Rev. Lett. **119**, no. 16, 161101 (2017) doi:10.1103/PhysRevLett.119.161101 [arXiv:1710.05832 [gr-qc]].

[147] Abbott, B. P., et al. 2017b, Astrophys. J., 848, L13; -. 2017c, Astrophys. J., 848, L12

[148] B. P. Abbott *et al.* [LIGO Scientific and Virgo Collaborations], Phys. Rev. Lett. **121**, no. 16, 161101 (2018) doi:10.1103/PhysRevLett.121.161101 [arXiv:1805.11581 [gr-qc]].

[149] D. Radice, A. Perego, F. Zappa and S. Bernuzzi,Burgio:2018yix Astrophys. J. **852**, no. 2, L29 (2018) doi:10.3847/2041-8213/aaa402 [arXiv:1711.03647 [astro-ph.HE]].

[150] A. Bauswein *et al.*, AIP Conf. Proc. **2127**, no. 1, 020013 (2019) doi:10.1063/1.5117803 [arXiv:1904.01306 [astro-ph.HE]].

[151] K. Kiuchi, K. Kyutoku, M. Shibata and K. Taniguchi Astrophys. J. bf 876, no. 2, L31 (2019) doi:10.3847/2041-8213/ab1e45 [arXiv:1903.01466 [astro-ph.HE]].

[152] E. Annala, T. Gorda, A. Kurkela and A. Vuorinen, Phys. Rev. Lett. **120**, no. 17, 172703 (2018) doi:10.1103/PhysRevLett.120.172703 [arXiv:1711.02644 [astro-ph.HE]].

[153] F. J. Fattoyev, J. Piekarewicz and C. J. Horowitz, Phys. Rev. Lett. **120**, no. 17, 172702 (2018) doi:10.1103/PhysRevLett.120.172702 [arXiv:1711.06615 [nucl-th]].

[154] S. De, D. Finstad, J. M. Lattimer, D. A. Brown, E. Berger and C. M. Biwer, Phys. Rev. Lett. **121**, no. 9, 091102 (2018) Erratum: [Phys. Rev. Lett. **121**, no. 25, 259902 (2018)] doi:10.1103/PhysRevLett.121.259902, 10.1103/PhysRevLett.121.091102 [arXiv:1804.08583 [astro-ph.HE]].

[155] A. Drago and G. Pagliara, Astrophys. J. **852**, no. 2, L32 (2018) doi:10.3847/2041-8213/aaa40a [arXiv:1710.02003 [astro-ph.HE]].

[156] G. F. Burgio, A. Drago, G. Pagliara, H. J. Schulze and J. B. Wei, Astrophys. J. **860**, no. 2, 139 (2018) doi:10.3847/1538-4357/aac6ee [arXiv:1803.09696 [astro-ph.HE]].

[157] E. R. Most, L. J. Papenfort, V. Dexheimer, M. Hanauske, S. Schramm, H. Stöcker, and L. Rezzolla, Phys. Rev. Lett. **122**, no. 6, 061101 (2019) doi:10.1103/PhysRevLett.122.061101 [arXiv:1807.03684 [astro-ph.HE]].

[158] L. R. Weih, E. R. Most and L. Rezzolla, Astrophys. J. **881**, 73 (2019) doi:10.3847/1538-4357/ab2edd, 10.3847/1538-4357 [arXiv:1905.04900 [astro-ph.HE]].

[159] G. Montana, L. Tolos, M. Hanauske and L. Rezzolla, Phys. Rev. D **99**, no. 10, 103009 (2019) doi:10.1103/PhysRevD.99.103009 [arXiv:1811.10929 [astro-ph.HE]].

[160] V. Dexheimer, L. T. T. Soethe, J. Roark, R. O. Gomes, S. O. Kepler and S. Schramm, Int. J. Mod. Phys. E **27**, no. 11, 1830008 (2018) doi:10.1142/S0218301318300084 [arXiv:1901.03252 [astro-ph.HE]].

[161] B. P. Abbott *et al.* [LIGO Scientific and Virgo Collaborations], Phys. Rev. X **9**, no. 1, 011001 (2019) doi:10.1103/PhysRevX.9.011001 [arXiv:1805.11579 [gr-qc]].

[162] A. Drago, A. Lavagno and G. Pagliara, Phys. Rev. D **89**, no. 4, 043014 (2014) doi:10.1103/PhysRevD.89.043014 [arXiv:1309.7263 [nucl-th]].

[163] E. P. Zhou, X. Zhou and A. Li, Phys. Rev. D **97**, no. 8, 083015 (2018) doi:10.1103/PhysRevD.97.083015 [arXiv:1711.04312 [astro-ph.HE]].

[164] T. Zhao, W. Zheng, F. Wang, C. M. Li, Y. Yan, Y. F. Huang and H. S. Zong, Phys. Rev. D **100**, no. 4, 043018 (2019) doi:10.1103/PhysRevD.100.043018 [arXiv:1904.09744 [nucl-th]].

[165] A. Drago, G. Pagliara, S. B. Popov, S. Traversi and G. Wiktorowicz, Universe **4**, no. 3, 50 (2018) doi:10.3390/universe4030050 [arXiv:1802.02495 [astro-ph.HE]].

[166] A. E. H. Love, Proc. R. Soc. A 82, 73 (1909).

[167] T. Hinderer, Astrophys. J. **677**, 1216 (2008) doi:10.1086/533487 [arXiv:0711.2420 [astro-ph]].

[168] T. Hinderer, B. D. Lackey, R. N. Lang and J. S. Read, Phys. Rev. D **81**, 123016 (2010) doi:10.1103/PhysRevD.81.123016 [arXiv:0911.3535 [astro-ph.HE]].

[169] S. Postnikov, M. Prakash and J. M. Lattimer, Phys. Rev. D **82**, 024016 (2010) doi:10.1103/PhysRevD.82.024016 [arXiv:1004.5098 [astro-ph.SR]].

[170] T. Damour and A. Nagar, Phys. Rev. D **80**, 084035 (2009) doi:10.1103/PhysRevD.80.084035 [arXiv:0906.0096 [gr-qc]].

[171] E. L. Oter, A. Windisch, F. J. Llanes-Estrada and M. Alford, J. Phys. G **46**, no. 8, 084001 (2019) doi:10.1088/1361-6471/ab2567 [arXiv:1901.05271 [gr-qc]].

[172] F. Douchin and P. Haensel, Astron. Astrophys. **380**, 151 (2001) doi:10.1051/0004-6361:20011402 [astro-ph/0111092].

[173] P. Haensel and A. Y. Potekhin, Astron. Astrophys. **428**, 191 (2004) doi:10.1051/0004-6361:20041722 [astro-ph/0408324].

[174] A. Y. Potekhin, A. F. Fantina, N. Chamel, J. M. Pearson and S. Goriely, Astron. Astrophys. **560**, A48 (2013) doi:10.1051/0004-6361/201321697 [arXiv:1310.0049 [astro-ph.SR]].

[175] Q. Wang, C. Shi and H. S. Zong, Phys. Rev. D **100**, no. 12, 123003 (2019) Erratum: [Phys. Rev. D **100**, no. 12, 129903 (2019)] doi:10.1103/PhysRevD.100.129903, 10.1103/PhysRevD.100.123003 [arXiv:1908.06558 [hep-ph]].

[176] M. B. Einhorn and D. R. T. Jones, JHEP **1605**, 185 (2016) [arXiv:1602.06290 [hep-th]].

[177] M. B. Einhorn and D. R. T. Jones, arXiv:1705.00751 [hep-ph].

[178] G. M. Pelaggi, A. D. Plascencia, A. Salvio, F. Sannino, J. Smirnov and A. Strumia, Phys. Rev. D **97**, no. 9, 095013 (2018) [arXiv:1708.00437 [hep-ph]].

[179] O. Antipin, N. A. Dondi, F. Sannino, A. E. Thomsen and Z. W. Wang, Phys. Rev. D **98**, no. 1, 016003 (2018) [arXiv:1803.09770 [hep-ph]].

[180] E. Molinaro, F. Sannino and Z. W. Wang, Phys. Rev. D **98**, no. 11, 115007 (2018) [arXiv:1807.03669 [hep-ph]].

[181] O. Antipin and F. Sannino, Phys. Rev. D **97**, no. 11, 116007 (2018) [arXiv:1709.02354 [hep-ph]].

[182] S. Abel and F. Sannino, Phys. Rev. D **96**, no. 5, 055021 (2017)

[arXiv:1707.06638 [hep-ph]].

[183] I. Bombaci, D. Logoteta, I. Vidana and C. Providencia, Eur. Phys. J. A 52, no. 3, 58 (2016) [arXiv:1601.04559 [astroph.HE]].

[184] D. M. Jacobs, G. D. Starkman and B. W. Lynn, Mon. Not. Roy. Astron. Soc. **450**, no. 4, 3418 (2015)

[arXiv:1410.2236 [astro-ph.CO]].

[185] S. Burdin, M. Fairbairn, P. Mermod, D. Milstead, J. Pinfold, T. Sloan and W. Taylor, Phys. Rept. **582**, 1 (2015)

[arXiv:1410.1374 [hep-ph]].

[186] A. Cho, Science, URL: http://science.sciencemag.org/content/360/6390/697; Lisa Zyga, Phys.org, URL: https://phys.org/news/2018-06-periodic-table.html;

[187] O. Adriani et al. [PAMELA Collaboration], Phys. Rev. Lett. 115, no. 11, 111101 (2015).

[188] Papazoglou, Panajotis, et al. Physical Review C 59.1 (1999): 411.

[189] Pelaez, Jose R. arXiv preprint arXiv:1510.00653 (2015).

[190] W. P. Alvarez, K. Kubodera and F. Myhrer, Phys. Rev. C **72**, 038201 (2005) [nucl-th/0506038].

[191] M. Abu-Shady and M. Rashdan, Int. J. Theor. Phys. **47**, 374 (2008).

[192] Ali, Tarek Sayed Taha. Journal of Modern Physics 4.11 (2013): 1471.

[193] Lee, T. D., and Y. Pang. Physical Review D 35.12 (1987): 3678.

[194] Bahcall, Safi, Bryan W. Lynn, and Stephen B. Selipsky. Nuclear Physics B 325.3 (1989): 606-618.

[195] Lee, Tsung-Dao, and Yang Pang. Physics Reports 221.5-6 (1992): 251-350.

[196] M. B. Wise and Y. Zhang, JHEP **1502**, 023 (2015) Erratum: [JHEP **1510**, 165 (2015)] [arXiv:1411.1772 [hep-ph]].

[197] M. I. Gresham, H. K. Lou and K. M. Zurek, Phys. Rev. D **96**, no. 9, 096012 (2017) [arXiv:1707.02313 [hep-ph]].

[198] M. I. Gresham, H. K. Lou and K. M. Zurek, Phys. Rev. D **98**, no. 9, 096001 (2018) [arXiv:1805.04512 [hep-ph]].

[199] M. I. Gresham and K. M. Zurek, Phys. Rev. D **99**, no. 8, 083008 (2019) [arXiv:1809.08254 [astro-ph.CO]].